



Expedition UT-GOM2-2 **Preliminary Report**

Terrebonne Basin Northern Gulf of Mexico
30 July–28 September 2023

Expedition UT-GOM2-2 Scientists

Publisher's notes

This work was supported by the U.S. Department of Energy (DOE), National Energy Technology Laboratory (NETL), under Contract No. DE-FE00223919.

This work was the result of scientific collaboration between the following institutions The University of Texas at Austin (UT), DOE, NETL, the United States Geological Survey (USGS), the Bureau of Ocean Energy Management (BOEM), The Ohio State University, Columbia University, University of New Hampshire, Oregon State University, University of Washington, Tufts University, Colorado School of Mines, and Geotek Ltd.

Our reporting structure, including this preliminary summary, is modeled after the reporting structure of the International Ocean Drilling Program (IODP). Core samples and the wider set of data from the science program covered in this report are under moratorium and accessible only to Science Party members until 31 December 2024.

Disclaimer

This report was prepared as an account of work sponsored by an agency of the United States Government. Neither the United States Government nor any agency thereof, nor any of their employees, makes any warranty, express or implied, or assumes any legal liability or responsibility for the accuracy, completeness, or usefulness of any information, apparatus, product, or process disclosed, or represents that its use would not infringe privately owned rights. Reference herein to any specific commercial product, process, or service by trade name, trademark, manufacturer, or otherwise does not necessarily constitute or imply its endorsement, recommendation, or favoring by the United States Government or any agency thereof. The views and opinions of authors expressed herein do not necessarily state or reflect those of the United States Government or any agency thereof.

Authorship and citation

Peter B. Flemings, Carla Thomas, Stephen C. Phillips, Timothy S. Collett, Ann E. Cook, Evan Solomon, Frederick S. Colwell, Joel E. Johnson, David Awwiller, Irita Aylward, Athma R. Bhandari, Donald Brooks, Alejandro Cardona, Michael Casso, Rachel Coyte, Tom Darrah, Marcy Davis, Brandon Dugan, Dan Duncan, John T. Germaine, Melanie Holland, Jesse Houghton, N. Tanner Mills, Michael Mimitz, Daniel Minarich, Yuki Morono, Zachary Murphy, Joshua O'Connell, Ethan Petrou, Tom Pettigrew, John W. Pohlman, Alexey Portnov, Marcie Purkey Phillips, Thomas Redd, Derek E. Sawyer, Peter Schultheiss, Kelly Shannon, Camille Sullivan, Cathal Small, Kayla Tozier, Man-Yin Tsang, Camila Van Der Maal, William F. Waite, Taylor Walton, 2024, *UT-GOM2-2 Preliminary Report Terrebonne Basin Northern Gulf of Mexico*, The University of Texas Institute for Geophysics, <https://doi.org/10.5281/zenodo.13648253>.



Cover photos

Left: Members of the science party inspect core at the Geotek Coring Inc. facilities in Salt Lake City, Utah. Pictured left to right: The Ohio State University professor Ann E. Cook, University of New Hampshire students Kayla Tozier and Camille Sullivan, U.S. Geological Survey scientist Timothy S. Collett, and University of New Hampshire professor Joel E. Johnson. Photo credit: Peter B. Flemings

Right: The Helix Q4000 semi-submersible platform and the 290-foot *Harvey Hermes* supply boat, carrying UT-GOM2-2 labs, pipe, fluids, and equipment, during a rendezvous on site. Photo credit: Peter B. Flemings



Members of the science party gather beneath the vessel banner designating The University of Texas at Austin (UT) as the operator on site. Photo credit: Monica Kortsha

Expedition UT-GOM2-2 participants

Leadership

Peter B. Flemings*[^] – The University of Texas at Austin, Chief Scientist

Carla Thomas[^] – The University of Texas at Austin, Staff Scientist & Lead Project Manager

Stephen C. Phillips*[^] – USGS Woods Hole, Lead Pressure Coring Scientist

Timothy S. Collett*[^] – USGS Denver, Lead Conventional Coring Scientist

Ann E. Cook*[^] – The Ohio State University, Lead Seismic-Log Integration & Depth Correlation

Evan Solomon* – University of Washington, Geochemist & Pore Water Lead Scientist

Frederick (Rick) S. Colwell*[^] – Oregon State University, Lead Microbiologist

Joel E. Johnson*[^] – University of New Hampshire, Lead Sedimentologist & Curation

Michael Mimitz*[^] – Geotek Coring Inc., Lead Coring Operations

Peter Schultheiss*^ – Geotek Ltd., Lead Core Logging and Physical Properties

Melanie Holland*^ – Geotek Ltd., Geochemist and Lead Core Processing

Jesse Houghton – The University of Texas at Austin, Regulatory Lead

Additional scientists (alphabetical by last name)

David Awwiller^ – ExxonMobil, Retired geoscientist

Irita (Rita) Aylward* – University of Washington, Geochemist

Athma R. Bhandari^ – The University of Texas at Austin, Geophysicist

Donald Brooks* – The University of Texas at Austin, Geoscientist

Alejandro Cardona*^ – The University of Texas at Austin, Geoscientist

Michael Casso – USGS Woods Hole, Geochemist

Rachel Coyte*^ – The Ohio State University, Geoscientist

Brandon Dugan – Colorado School of Mines, Lead in-situ measurements

John (Jack) T. Germaine^ – Tufts University, Lead Geomechanics

N. Tanner Mills* – The University of Texas at Austin, Lab Scientist

Daniel Minarich* – Geotek Coring Inc., Coring Operations

Yuki Morono^ – Kochi Institute for Core Sample Research JAMSTEC, Geoscientist

Zachary Murphy* – The University of Texas at Austin, Geoscientist

Joshua O’Connell* – The University of Texas at Austin, Geoscientist

Ethan Petrou* – The University of Texas at Austin, Geoscientist

John W. Pohlman - USGS Woods Hole, Geochemist

Alexey Portnov – The University of Texas at Austin, Seismologist

Marcie Purkey Phillips^ – The University of Texas at Austin, Biostratigrapher

Derek E. Sawyer*^ – The Ohio State University, Geoscientist

Kelly Shannon*^ – Oregon State University, Microbiologist

Cathal Small – Tufts University, Geomechanics

Camille Sullivan*^ – University of New Hampshire, Sedimentologist

Kayla Tozier^ – University of New Hampshire, Sedimentologist

Man-Yin Tsang^ – University of Washington, Geochemist

Camila Van Der Maal* – The University of Texas at Austin, Lab Scientist

William F. Waite[^] – USGS Woods Hole, Geoscientist

Taylor Walton^{*^} – University of Washington, Geochemist

Technical support (alphabetical by last name)

Tom Darrah – The Ohio State University, Geochemist

Marcy Davis – The University of Texas at Austin, Technical writer

Dan Duncan – The University of Texas at Austin, Lab Construction and Logistics

Tom Pettigrew – Pettigrew Engineering, Operations

Thomas (TR) Redd^{*} – TR Consulting, Company Rep.

*Offshore

[^]Dockside



Members of the Helix Q4000 crew (in red), science party members from Geotek Ltd. (in blue), and science party members from various universities (in navy) celebrate on the Helix Q4000 helipad. Photo Credit: Helix staff member

Abstract

In the summer and fall of 2023 the Gulf of Mexico Deepwater Hydrate Coring Expedition (UT-GOM2-2) drilled, cored, made downhole measurements, and analyzed samples from the seafloor to the base of the gas hydrate stability zone in one location, Site H in Walker Ridge Block 313 (Site H, WR313), in the Terrebonne Basin, deepwater Gulf of Mexico.

Analyses of data and samples from the expedition will inform biological, geochemical, and geomechanical models to constrain the role of gas hydrates in the carbon cycle and the potential for gas hydrates as an energy resource. Pressure and conventional cores were collected continuously to a depth of 155.1 meters below the seafloor (mbsf). At deeper depths, cores were taken periodically from hydrate-bearing sands and their bounding muds to a total depth of 861.3 mbsf, with 162.6 m of conventional core and 54.8 m of pressure core obtained.

Twelve temperature measurements were made between 27.1 mbsf and 144.5 mbsf to determine the geothermal gradient. At the seafloor, more than 4 m of sandy silt of unknown origin was encountered. Beneath this sand, to a depth of about 200 mbsf, the section was composed of interbedded mud and biogenic carbonate ooze. The biogenic ooze correlated to low density and high porosity intervals observed in the previously acquired logging while drilling (LWD) data and as measured. Calcareous nannofossil biostratigraphy constrains the

entire record to the Pleistocene (< 0.91 million years) with a pronounced increase in sedimentation rate with depth. Beneath 200 mbsf, the section was predominantly composed of mud with two thicker, hydrate-bearing coarse-grained intervals, which are commonly known as the Blue and Orange sands.

The dissolved gas concentration was quantified from pressure cores. In the shallow section, dissolved methane concentration increased below the sulfate-methane transition zone (SMTZ) and reaches saturation (the limit of solubility for methane) at 147 mbsf. Gas expansion was very common in conventional and depressurized pressure (conventionalized) cores below the SMTZ.

At deeper depths, the methane concentration within muds bounding the Blue and Orange reservoirs was generally found to be less than saturation. The dissolved and hydrate gas composition is consistent with a microbial source, containing greater than 99.99% methane and only trace concentrations of ethane, propane, and butane. The methane to ethane ratio (C_1/C_2) and the methane to ethane plus propane $C_1/(C_2+C_3)$ decrease with depth down to at least 678 mbsf, mainly driven by the increase in ethane with depth. It is unclear if this trend continues through the Orange sand interval. The $\delta^{13}C$ isotopic signature of methane ranges between -69.9 and -78.5 ‰ Vienna Pee Dee Belemnite (VPDB).

Pressure core recovery of all sandy intervals was poor. However, pressure core logs of the Orange sand show intervals of low density and high P-wave velocity, which are indicative of high hydrate saturation. One core from within the Orange sand was composed of interbedded graded sandy silt and mud. The sandy silts from this core are composed of mainly quartz and feldspar with some lithics. Most of the recovered pressure core samples are maintained at near in-situ pressure and temperature (within the hydrate stability field) at The University of Texas at Austin Pressure Core Center awaiting analysis.

In the shallow section, samples will be used to determine the flux of organic carbon through the

basin system, find the rate at which that carbon was consumed, and understand the microbial population responsible for these processes. In the deeper section, samples from in and around the hydrate reservoirs will be used to determine the petrophysical properties of the reservoir and bounding seals in these systems.

Table of contents

Publisher’s notes	2
Disclaimer	2
Authorship and citation	2
Cover photos	2
Expedition UT-GOM2-2 participants	3
Leadership	3
Additional scientists (alphabetical by last name)	4
Technical support (alphabetical by last name)	5
Abstract	6
Table of contents	8
List of figures	10
List of tables	11
List of equations	12
List of acronyms, abbreviations, symbols, units, and sample codes with definitions	13
Introduction	17
Scientific motivation	18
Gas hydrates, the global carbon cycle, and the microbial factory	19
Gas hydrates and energy	19
Gas hydrate and CO₂ sequestration	20
Background	21
Geological overview	21
Site H seismic and LWD interpretation	26
Geothermal gradient and thermodynamic conditions	33
Hazards	34
Pore pressure and fracture gradient	34
Science objectives	36
Planning	37
DOE project development and structure	37
Proposed borehole locations and sampling program	38
Drilling platform selection and contracting strategy	40
Regulatory obligations and compliance	41
Execution	44
Preparation and mobilization to the port	44

<u>Mobilization on the rig</u>	46
<u>Onboard operations</u>	46
<u>Demobilization from the rig</u>	46
<u>Remobilization in Salt Lake City</u>	47
<u>Salt Lake City operations</u>	47
<u>Demobilization from Salt Lake City</u>	48
<u>Drilling operations</u>	49
<u>Operational summary</u>	49
<u>Surface locations</u>	49
<u>Water depth and rig floor elevation</u>	49
<u>Borehole deviation survey</u>	50
<u>Correlation of Hole H001 log data to Site H core data</u>	51
<u>Correlations of Hole H001 LWD log data to Hole H003 core data</u>	51
<u>Correlation of Hole H001 LWD log data to Hole H002 core data</u>	52
<u>Plotting H001, H002, and H003 downhole data</u>	52
<u>Drilling challenges</u>	52
<u>Plug and abandonment</u>	54
<u>Scientific results</u>	58
<u>Coring</u>	58
<u>Core recovery</u>	58
<u>Pressure coring tool performance</u>	61
<u>Plotting core data as a function of depth</u>	61
<u>Lithostratigraphy</u>	63
<u>Lithologies</u>	63
<u>Lithofacies</u>	64
<u>Lithologic units</u>	64
<u>Calcareous nannofossil biostratigraphy</u>	67
<u>Physical properties</u>	74
<u>In-situ temperature</u>	74
<u>Core logging</u>	77
<u>Strength measurements</u>	77
<u>Index properties</u>	77
<u>Dissolved methane concentrations and hydrate saturation</u>	81
<u>Microbiology</u>	83

Geochemistry	83
Pore water geochemistry	86
Gas geochemistry	86
Sediment geochemistry	87
References	91

List of figures

Figure F1: Seafloor shaded relief map of the NW part of the Walker Ridge (WR) Protraction Area	22
Figure F2: Bathymetry map of the study area in the southern Terrebonne Basin	23
Figure F3: North-South regional cross-section through the Terrebonne Basin	24
Figure F4: Seismic section A to A' through previously drilled boreholes in WR Block 313.....	25
Figure F5: SW-NE oriented seismic section B to B'	25
Figure F6: Instantaneous amplitude map of Horizon (Hrz) 0400 (Blue)	27
Figure F7: Instantaneous amplitude map of Horizon (Hrz) 0300 (Orange).....	28
Figure F8: Stratigraphic overview of Hole H001	29
Figure F9: Hole H001 logging while drilling (LWD) data for the uppermost interval (0-150 mbsf)	31
Figure F10: Hole H001 logging while drilling (LWD) data in sand intervals	32
Figure F11: Estimated temperature profile from the seafloor to the BSR.....	34
Figure F12: Pressure and fracture gradient plot.....	35
Figure F13: Predicted depth versus time for the duration of UT-GOM2-2	39
Figure F14: Bit depth as a function of time	51
Figure F15: The locations, distances, and azimuths of the boreholes.....	52
Figure F16: Demonstration of correlation between Hole H001 and Hole H003	53
Figure F17: Images of the sandy seafloor	55
Figure F18: Visual core description grain size at the top of Core H003-01H	56
Figure F19: Examples of particle size distribution of sands encountered during drilling.....	57
Figure F20: Core deployments and temperature measurements.....	59
Figure F21: Core deployments at the Red sand.....	60
Figure F22: Interpreted depth when the pressure coring tool sealed	62
Figure F23: Illustration of how the compressed depth below seafloor is calculated.....	63
Figure F24: Ternary plots of sediment grain size and composition	65
Figure F25: Site H lithologic units and lithofacies	66
Figure F26: Lithologic Unit II (interbedded Ooze lithofacies and Mud lithofacies)	67
Figure F27: Lithologic Unit II.....	68
Figure F28: Representative interval of Lithologic Unit IV	69

Figure F29: Expanded view of Lithologic Unit IV	70
Figure F30: Expanded view of Lithologic Unit IV	71
Figure F31: View of Lithologic Units V, VI, and VII	72
Figure F32: Expanded view of Lithologic Unit VI	73
Figure F33: Composite time-depth plot of calcareous nannofossil biohorizons	75
Figure F34: A typical APCT-3 temperature measurement	76
Figure F35: Interpreted in-situ temperatures	76
Figure F36: Temperatures with true-vertical depth below the seafloor at Hole H003.....	76
Figure F37: Example of data from analysis of a pressure core	78
Figure F38: Example conventional core log	79
Figure F39: Example split core scan logs	80
Figure F40: Undrained shear strength measurements.....	80
Figure F41: Measured A) bulk density, B) water content, C) water saturation, and D) porosity	81
Figure F42: Example quantitative degassing results	82
Figure F43: Downhole dissolved methane concentration	83
Figure F44: Geochemistry summary	84
Figure F45: Expanded view of the Geochemistry Summary	85
Figure F46: Uncorrected concentration profiles of A) salinity and B) alkalinity.....	87
Figure F47: Expanded view of the uncorrected concentration profiles of A) salinity and B) alkalinity.....	87
Figure F48: $\delta^{13}\text{C}$ isotopic ratio of methane and molecular ratios.....	88
Figure F49: Initial downhole CNS element analysis results	89
Figure F50: Total sulfur vs total organic carbon cross-plot	90

List of tables

Table T1: Surface and bottom-hole locations of previously drilled boreholes.....	26
Table T2: Total depth, rig height (air gap), and water depth of previously drilled boreholes.....	26
Table T3: Mapped seismic horizons and major stratigraphic surfaces in Hole H003	30
Table T4: UT-GOM2-2 regulatory planning documents and permits	42
Table T5: UT-GOM2-2 regulatory reports and notifications.....	43
Table T6: UT-GOM2-2 execution phases performed in 2023.....	45
Table T7: High-level operational summary	50
Table T8: Final surface and bottom-hole locations and water depth	52
Table T9: Hole H003 and Hole H002 borehole deviation surveys	53
Table T10: Correlated seismic horizons and stratigraphic surfaces in Holes H001, H002, and H003	54

Table T11: Three incidents where tools became stuck inside the BHA.....	55
Table T12: Lithofacies classification.....	64

List of equations

Equation E1: Archie’s equation, used to calculate the hydrate saturation in coarse-grained intervals only.....	29
Equation E2: Used to model the fracture gradient.....	34
Equation E3: Used to correlate the measured depth below seafloor between the H001 and H003 wells.....	51
Equation E4: Used to calculate the compressed depth below seafloor of a specific sample or measurement.....	62
Equation E5: Used to determine the compression factor, which is unique to each core.....	62
Equation E6: Used to convert the sample depth in core to compressed depth in core.....	63
Equation E7: Used to calculate the compressed depth below the seafloor.....	63

List of acronyms, abbreviations, symbols, units, and sample codes with definitions

Acronyms, Abbreviations, Symbols, Units, & Sample Codes	Definition
AOM	Anaerobic Oxidation of Methane
APC	Advanced Piston Corer
APCT-3	Advanced Piston Coring Tool
APD	Application for Permit to Drill
API	American Petroleum Institute
APM	Application for Permit to Modify
ASTM	American Society for Testing and Materials
bbl	barrels
BHA	Bottom-Hole Assembly
BHSZ	Base of Hydrate-Stability Zone
BOEM	U.S. Bureau of Ocean Energy Management
BSEE	U.S. Bureau of Safety and Environmental Enforcement
bsf	Below the seafloor
bsl	Below the sea level or sea surface
BSR	Bottom-Simulating Reflector
Ca	Calcium
CD	Compressed Depth
CEL	Cell Counts
CF	Compression Factor
CFR	United States Code of Federal Regulation
CRDS	Cavity Ring-Down Spectrometer
CT	Computed Tomography
D	Depth
DMR	Discharge Monitoring Report
DNA	Deoxyribonucleic acid
DOE	U.S. Department of Energy
DP	Dynamic Positioning
DST	Data Storage Tag
DWOP	Drill-Well-on-Paper
E	East
EPA	U.S. Environmental Protection Agency
Eq	Equation
FAD	First Appearance Datum (evolution)
fbsf	feet below seafloor

Acronyms, Abbreviations, Symbols, Units, & Sample Codes	Definition
fbsl	feet below the sea level or sea surface
FID	Flame Ionization Detector
ft	feet
g/cc or g/cm ³	grams per cubic centimeter
g/kg	grams per kilogram
G-APC	Geotek Advanced Piston Corer
GC	Gas Chromatography
GEOM	Geomechanics
GR	Gamma Ray
G-XCB	Geotek eXtended Core Barrel
HQ	Headquarters
H001, H002, H003	Boreholes at Walker Ridge Block 313 Location H
Hrz	Horizon
HS	Headspace Gas Sample
IC	Inorganic Carbon
IR	Infrared
IWO	Interstitial Water (Organics)
IWR	Interstitial Water (Regular)
JAMSTEC	Japan Agency for Marine-Earth Science and Technology
JIP	Joint Industry Project
Km	Kilometer
kPa	kilo pascals
L	Length
L*	sediment lightness in spectrophotometry
LAD	Last Appearance Datum (extinction)
LDNR	Louisiana Department of Natural Resources
LWD	Logging While Drilling
m	meters
mM	millimolar
<i>m</i>	Archie tortuosity exponent (Archie, 1942)
MAD	Moisture and Density
MB	Microbiology
mbsf	meters below seafloor
MD	Measured Depth
MDW	Moisture and Density
MDT	Mass Transport Deposits
m/s	meters/second

Acronyms, Abbreviations, Symbols, Units, & Sample Codes	Definition
MPa	mega pascals
MSCL	Multi-Sensor Core Logger
N	North
NAD	North American Datum
NE	Northeast
NEPA	U.S. National Environmental Policy Act
NPDES	U.S. National Discharge Elimination System
NTL	Notice to Lessees
OCS	Outer Continental Shelf
OSR	Organoclastic Sulfate Reduction
P & A	Plug and Abandonment
PCATS	Pressure Core Analysis and Transfer System
PCTB	Pressure Coring Tool with Ball Valve
PCTB – CS	Pressure Coring Tool with Ball Valve in the Cutting Shoe Configuration
PCTB – FB	Pressure Coring Tool with Ball Valve in the Face Bit Configuration
PE	Professional Engineer
PEN	Handheld or Pocket Penetrometer
ppg	pounds per gallon
ppm	parts per million
psi	pounds per square inch
RRING	Ring Resistivity
RES	Resistivity
RFQ	Request for Qualifications
RIH	Run in Hole, run into borehole
RKB	Rotary Kelly Bushing or Rig Floor when no bushing is present
Ro	Formation Resistivity assuming 100% water saturation
ROV	Remotely-Operated Vehicle
RUE	Right of Use and Easement
RW	Reworked
Rw	Water Resistivity
S	South
Sh	Hydrate saturation (% of pore space)
SI	International System of Units
SW	Southwest
SMTZ	Sulfate-Methane Transition Zone
T2P	Temperature 2 Pressure Probe
TC	Total Carbon

Acronyms, Abbreviations, Symbols, Units, & Sample Codes	Definition
TCD	Thermal Conductivity Detector
TDS	Top Drive System
T-HUET	Tropical Helicopter Underwater Escape Training
Ti	Titanium
TN	Total Nitrogen
TOC	Total Organic Carbon
TS	Total Sulfur
TVD	Total Vertical Depth
USC	United States Code
USCG	United States Coast Guard
USGS	United States Geological Survey
UT	The University of Texas at Austin
UTM	Universal Transverse Mercator
W	West
WBM	Water-based Mud
WR	Walker Ridge
WR313	Walker Ridge Block 313
wt.%	weight percent
VPDB	Vienna Pee Dee Belemnite
XCB	eXtended Core Barrel
XRF	X-ray Fluorescence
XRPD	X-ray Powder Diffraction
K	Effective Stress Ratio
μm	micrometer
Σ_v	overburden stress
Σ_{hmin}	least principal stress
u_h	hydrostatic pore pressure
ϕ	porosity
Ωm	Ohm meter
3D	three-dimensional



The sun rises on another day on location at Walker Ridge Block 313 during the drilling of Hole H002. The *Harvey Spirit* has arrived to provide additional support. Photo credit: Peter B. Flemings

Introduction

In the summer and fall of 2023, The University of Texas at Austin (UT) Gulf of Mexico Deepwater Hydrate Coring Expedition (UT-GOM2-2) drilled, cored, made downhole measurements, and analyzed samples from the seafloor to the base of the gas hydrate stability zone at Site H in Walker Ridge Block 313 (Site H, WR313) in the Terrebonne basin, deepwater Gulf of Mexico.

This was the primary expedition of the Deepwater Methane Hydrate Characterization & Scientific Assessment project (DE-FE0023919). This project is funded by the United States Department of Energy (DOE), National Energy Technology Laboratory (NETL), and advised by the United States Geological Survey (USGS) and the Bureau of Ocean Energy Management (BOEM). We successfully sampled and analyzed the physical, chemical, and biological properties of hydrate-bearing reservoirs, their bounding strata, and the overlying sedimentary section. Completed and ongoing analyses of data and samples from the expedition will inform biological, geochemical, and geomechanical models to constrain the role of gas hydrates in the carbon cycle and the potential for gas hydrates as an energy resource.

The program planned to recover samples from the first few hundred meters beneath the seafloor to illuminate the microbial factory that is the primary source of the methane found in gas hydrates in the deep oceans. We sought to determine the flux of organic carbon through the basin system, find the rate at which that carbon was consumed, and methane was produced, and understand the microbial population responsible for these processes. We also sampled deeper, hydrate-bearing reservoirs, and their bounding non-reservoir units to interpret the petrophysical properties of these reservoirs and illuminate the mechanisms by which they formed.

We first summarize the underlying scientific questions that drove the program. We then provide the geological overview of the study region. We then integrate this framework to illustrate how we developed our operational plan. We then summarize the execution of the drilling and core analysis program. This includes an overview of the execution, the drilling operations, and a summary of scientific results.



USGS scientist Stephen C. Phillips degassing pressure cores — a process that measures how much gas is in each core sample.
Photo Credit: Monica Kortsha

Scientific motivation

About 10,000 billion tons of mobile carbon (in land plants, peat, soil, organic and inorganic carbon dissolved in the ocean, and fossil fuels) constantly cycle through the solid Earth, the ocean, and the atmosphere (Isson et al., [2020](#); You et al., [2019](#)). Of this carbon, 5% to 22% is trapped in gas hydrate, an ice-like substance composed mostly of methane and water (Boswell and Collett, [2011](#); Milkov, [2004](#); Ruppel and Kessler, [2017](#); Sloan and Koh, [2007](#)).

Most of this massive carbon reservoir lies in continental marine margin sediments within a layer that extends downward from the seafloor and can reach thicknesses of ~1,000 m (3,280 ft.) (Boswell and Collett, [2011](#); Kvenvolden, [2012](#)). This layer interacts with the Earth's oceans and, perhaps, the atmosphere (Ruppel and Kessler, [2017](#)). This dynamic carbon reservoir is a potential energy resource (Boswell and Collett, [2011](#)), a potential source of geohazards (Kayen and Lee, [1991](#); Mienert et al., [2005](#)), and a potential driver for climate change (Kennett et al., [2000](#); Ruppel and Kessler, [2017](#)).

Gas hydrates, the global carbon cycle, and the microbial factory

The atmosphere currently contains only 8% (about 800 billion tons) of the total mobile carbon (Schuur et al., [2008](#)). Thus, the hydrate carbon reservoir is of the same scale as that of the atmosphere. Furthermore, because methane is a greenhouse gas with 84 times the radiative forcing of carbon dioxide (CO₂) over a 20-year timeframe (Ruppel and Kessler, [2017](#)), any leakage of methane directly into the atmosphere can disproportionately impact climate. However, current evidence suggests that marine methane seeps from the hydrate stability zone are unlikely to pass through the ocean to reach the atmosphere (Ruppel and Kessler, [2017](#)). Instead, in many locations above hydrate deposits, methane vents into the overlying ocean and it is commonly oxidized, resulting in potential ocean acidification (Biastoch et al., [2011](#); Boudreau et al., [2015](#)). In addition, methane flowing upward within seafloor sediments is largely oxidized within near-seafloor sediments, leading to a flux of dissolved carbon into the ocean (Reeburgh, [2007](#)). However, large-scale hydrate dissociation events and the consequent methane emissions have been proposed to cause large climate perturbation in the geologic past (Kennett et al., [2000](#); Ruppel and Kessler, [2017](#)). The workings of this sedimentary carbon recycling factory and the role played by gas hydrates are not yet completely understood. A detailed sampling program of the marine water column and the underlying subsea sedimentary section has the potential to better illuminate these fluxes in the marine hydrate system.

At the root of this system is the microbial factory that ultimately produces methane (Claypool and Kvenvolden, [1983](#); Kida et al., [2015](#); Lorenson and Collett, [2018](#); Pohlman et al., [2009](#)). Wei et al. ([2024](#)) review the complex process by which primary organic carbon in marine sediments is broken down by a sequence of microbially-mediated reactions to generate dissolved organic carbon of decreasing molecular weights, which are eventually utilized in terminal respiratory processes such as methanogenesis.

We are only beginning to explore the microbial communities that are present, and the complex interactions and kinetics that control this process. A detailed sampling program of geochemistry and microbiology as a function of depth of burial has the potential to further illuminate these processes.

Gas hydrates and energy

The large amount of natural gas stored in gas hydrates makes hydrate reservoirs one of the most abundant possible unconventional energy resources on Earth (Boswell and Collett, [2011](#); Milkov, [2004](#); Yin and Linga, [2019](#)). Most of these hydrates lie within mudrocks and are unlikely to be economic because they have low hydrate concentration and little permeability (Boswell, [2009](#); Milkov, [2004](#)). In contrast, Japanese researchers found hydrate saturations greater than 80% in silts and sands of the Nankai Trough (Tsuji et al., [2004](#)). The high hydrate saturation and high intrinsic permeability of these deposits make them attractive for energy production (Boswell, [2009](#); Boswell and Collett, [2011](#)).

These types of hydrate reservoirs have now been found around the globe and recent expeditions have focused on characterizing their petrophysical behavior (Boswell et al., [2019b](#); Flemings et al., [2020b](#); Yamamoto, [2015](#)). This work has focused on illuminating the effective permeability, and the geomechanical behavior of the hydrate-bearing reservoirs and their bounding non-reservoir sections (Bhandari et al., [2024](#); Boswell et al., [2020](#); Cardona et al., [2023](#); Flemings et al., [2022](#); Yoneda et al., [2021](#)).

An accurate description of petrophysical behavior will better constrain reservoir simulation models and allow us to evaluate optimal approaches to safely produce hydrate reservoirs (Boswell et al., [2019a](#)). The chemistry and methane concentration of these reservoirs and their bounding seals can also be used to test models by which these reservoirs formed.

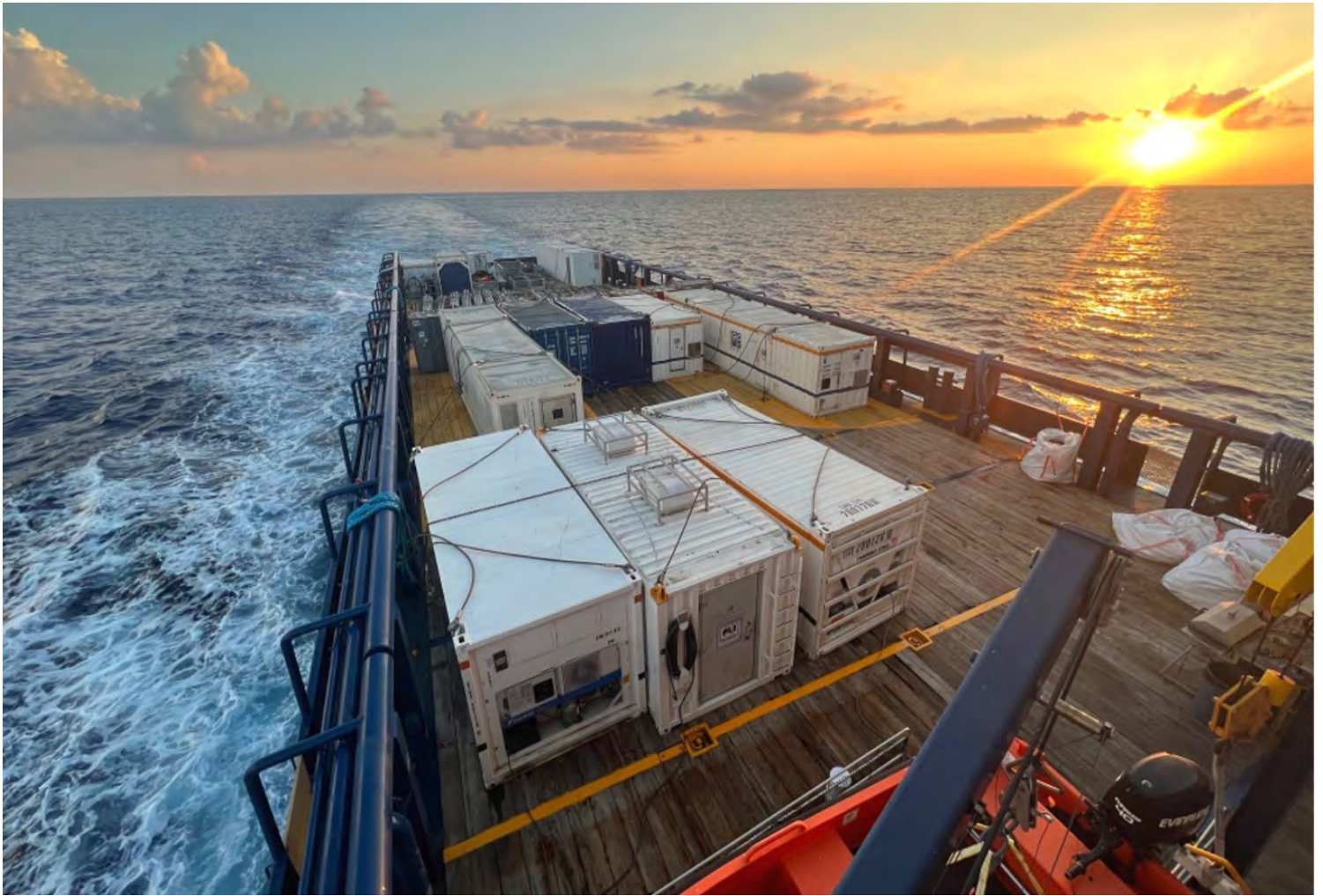
A central challenge has been to understand the mechanism by which coarse grained hydrate reservoirs are charged and contained (Malinverno and Goldberg, [2015](#)). This will strengthen our ability to explore for hydrate reservoirs.

Gas hydrate and CO₂ sequestration

CO₂ could be stored as an immobile, solid, CO₂-hydrate. One strategy that has been attempted is to replace methane in a hydrate reservoir with CO₂ (Boswell et al., [2017](#)), preserving the reservoir's geomechanical stability and reducing the environmental impact of the produced methane.

An alternative approach is to inject CO₂ into an aquifer that lies within the hydrate stability zone (Bhati et al., [2024](#); Darnell et al., [2019](#); Zheng et al., [2020](#)).

An improved understanding of the thermodynamic behavior of multi-component systems and of the geomechanical properties of gas hydrate reservoirs will inform simulation models for CO₂ sequestration that seek to optimize storage approaches (Zhang et al., [2011](#)).



The sun sets on the Gulf of Mexico as *Harvey Spirit* makes its way back to Port Fourchon with UT-GOM2-2 chilled laboratories carrying samples and core. Photo credit: Geotek Ltd.

Background

UT-GOM2-2 drilled and cored two boreholes at Site H in the Walker Ridge Protraction Area Block 313 (WR313) (Figure [F1](#)). Site H was originally drilled (Hole H001) using logging while drilling (LWD) data collected during the 2009 Gas Hydrates Joint Industry Project Leg II (JIP II) (Boswell et al., [2012a](#); Boswell et al., [2012b](#); Frye et al., [2012](#); Hutchinson et al., [2008](#); Shedd et al., [2010](#)).

Geological overview

The study area is near the southern boundary of Terrebonne Basin in WR313 about 193 miles (168 nautical miles) southwest of Port Fourchon, Louisiana, USA (Figure [F1](#)). The water depths range from 6,000 ft to 6,800 ft in the study area (Figure [F2](#)). The local seafloor topographic gradient in the study area varies between 2° and 3°.

Terrebonne Basin is a salt-floored and salt-bounded mini-basin on the midslope of central deepwater Gulf of Mexico (Diegel et al., [1995](#); Frye et al., [2012](#); Prather et al., [1998](#)). The strata that infill the basin dip and thicken to the north (Figure [F3](#)). Portnov et al. ([2023](#)) and Varona et al. ([2023](#)) describe the regional stratigraphy of basin sediments.

McConnell and Kendall ([2002](#)) first identified and described gas hydrate potential in the southeastern lobe of the Terrebonne Basin, where they observed seismic discontinuities called bottom-simulating reflections (BSRs)

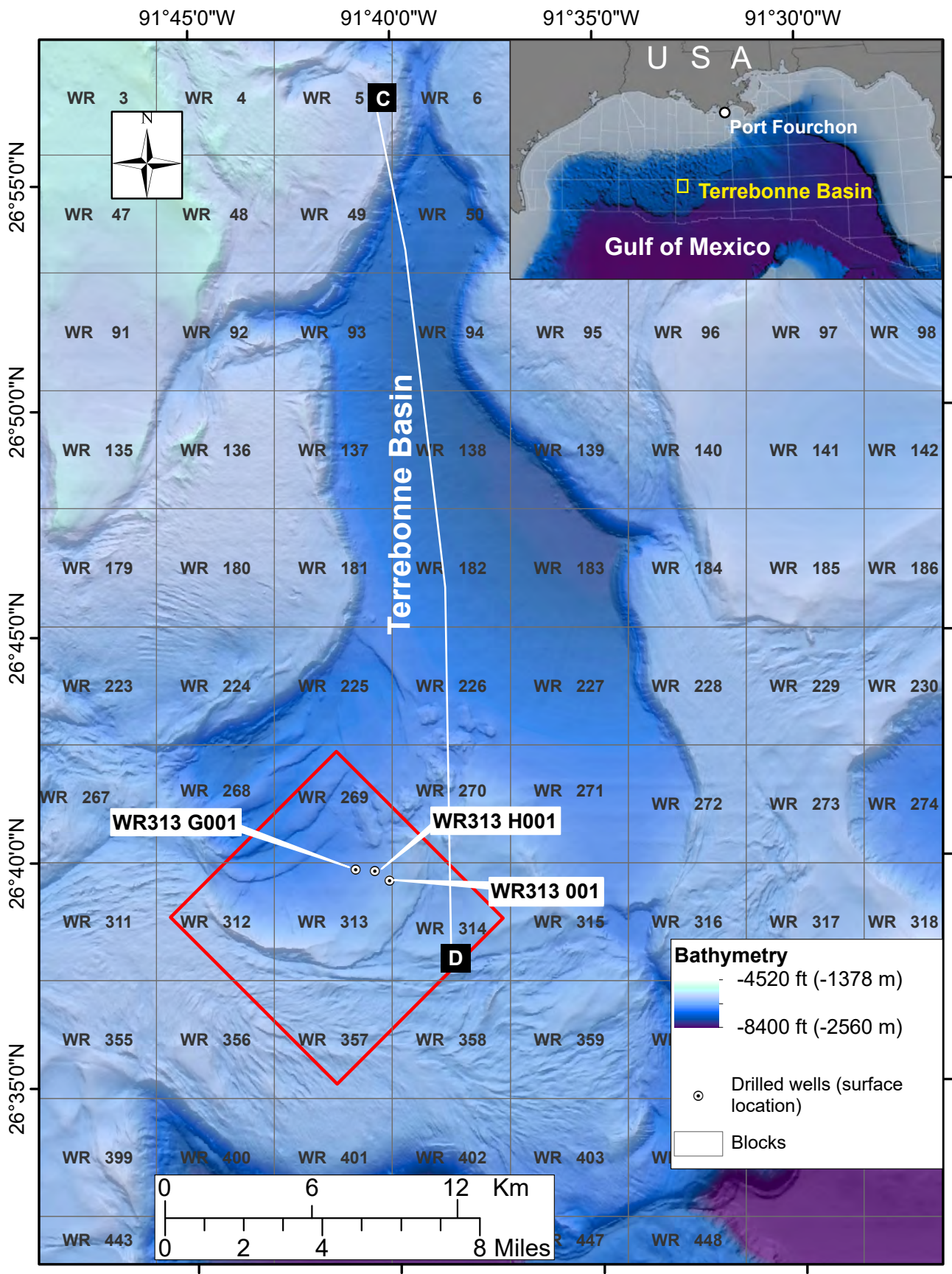


Figure F1: Seafloor shaded relief map of the northwest (NW) part of the Walker Ridge (WR) Protraction Area showing Terrebonne Basin and previously drilled locations in Walker Ridge Block 313 (WR313). The inset map shows the position of Terrebonne Basin in the northern Gulf of Mexico. The red box highlights the study area and is expanded in Figure F2. The transect between "C" and "D" is illustrated in Figure F3. The bathymetry data are from U.S. Bureau of Ocean Energy Management (BOEM) *Northern Gulf of Mexico Deepwater Bathymetry Grid from 3D Seismic* (Kramer and Shedd, 2017).

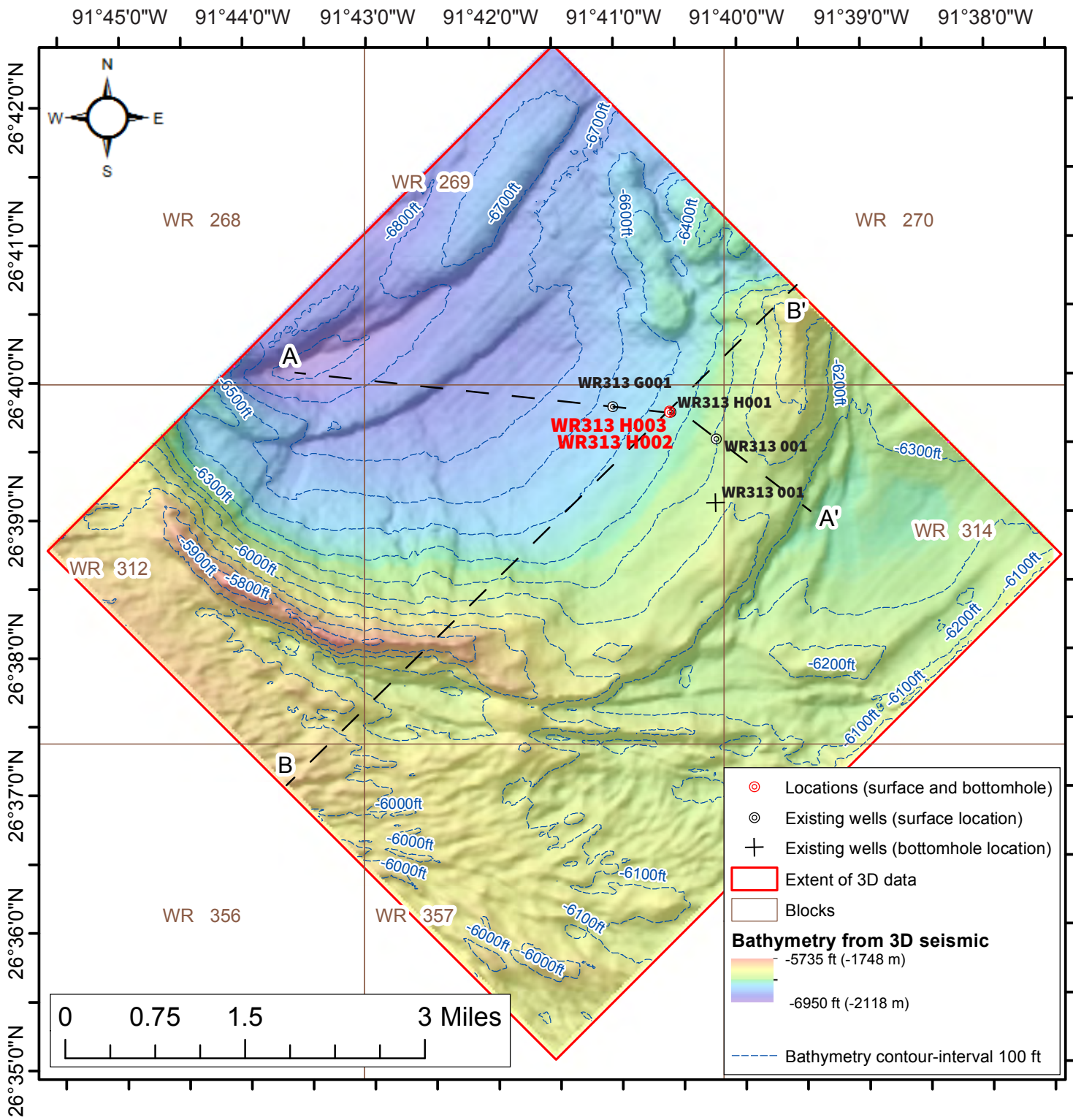


Figure F2: Bathymetry map of the study area in the southern Terrebonne Basin, showing the locations of boreholes drilled prior to and during this expedition. Previously drilled boreholes are shown with black labels. Walker Ridge Block 313 (WR 313) H002 (Hole H002) and WR313 H003 (Hole H003), shown with red labels, were drilled during this expedition. The transect between “A” and “A’” is presented in Figure F4. The transect between “B” and “B’” is presented in Figure F5. Bathymetry is based on 3D seismic data, courtesy of WesternGeco.

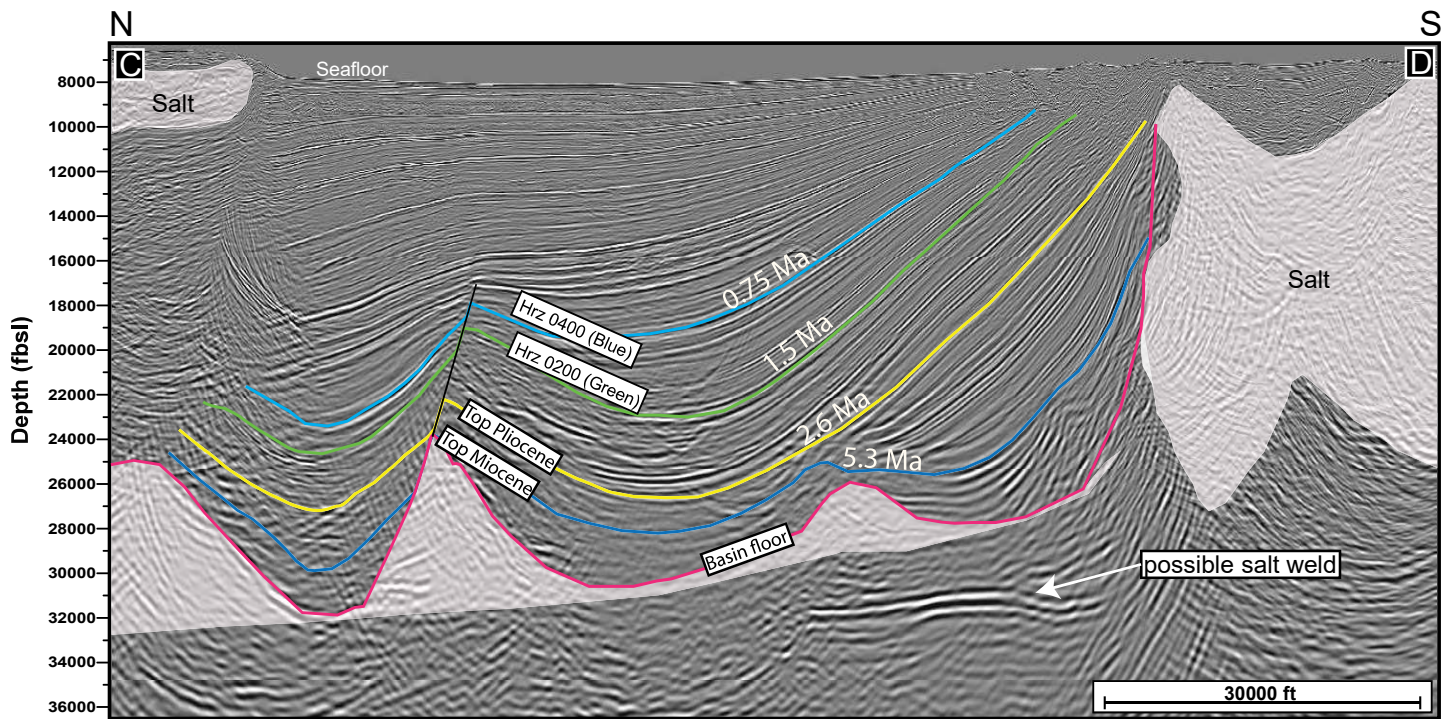


Figure F3: North-South regional cross section through the Terrebonne Basin (located in Figure F1). The interpreted ages are based on existing calcareous nannofossil and foraminifera biostratigraphy data from industry wells as described by Portnov et al. (2023). Figure modified from Portnov et al. (2023).

that they interpreted to record the base of hydrate stability zone (BHSZ) (Frye et al., 2012; McConnell and Kendall, 2002) (Figures F4 and F5).

The BHSZ marks the boundary above which hydrate is stable and below which hydrate is not stable. At WR313, the presence of high saturation hydrate in coarse-grained layers results in a high acoustic impedance or positive polarity reflection due to the high pressure wave (P-wave) velocity of the hydrate (Boswell et al., 2016; McConnell and Zhang, 2005).

Below the base of hydrate stability, gas may be present, causing a decrease in P-wave velocity and a significant negative acoustic impedance or negative polarity reflection. Thus, within a single horizon, the change in acoustic impedance from positive polarity reflection (peak) to a negative polarity reflection (trough) can be mapped as the BHSZ (Hillman et al., 2017b; McConnell and Kendall, 2002; Portnov et al., 2023; Shedd et al., 2012).

Three previously drilled boreholes exist in the WR313 study area (Figures F1, F2 and Table T1, T2). One exploration well, WR313 001, was drilled by Devon Energy in 2001 to target Pliocene and Miocene oil

reservoirs (Figure F1). Two LWD boreholes WR313 G001 (Hole G001) and WR313 H001 (Hole H001) (Figure F1) were drilled during the JIP II LWD program to test gas hydrate targets (Boswell et al., 2012a; Boswell et al., 2012b; Collett et al., 2009; Frye et al., 2012; Hutchinson et al., 2008; Shedd et al., 2010).

Seismic horizons were mapped on 3D seismic data throughout the study area and assigned a numerical designation for each mapped horizon with the numbering increasing upward (e.g. Figure F4). Mapped horizons correlate to previously mapped horizons by others but they used a different nomenclature (Boswell et al., 2012a; Boswell et al., 2012b; Hillman et al., 2017b).

For example, Horizon (Hrz) 0300 is a seismic reflection that correlates with the top of the Orange sand interval. This horizon was previously termed the Orange horizon. It is thus presented as Hrz 0300 (Orange) in this study (e.g. Figure F4). Similarly, Horizon 0400 is a regionally mappable reflector associated with the top of the lower Blue sand and is termed Hrz 0400 (Blue). Hrz 0300 (Orange) and Hrz 0400 (Blue) are prominent reflectors in the 3D seismic

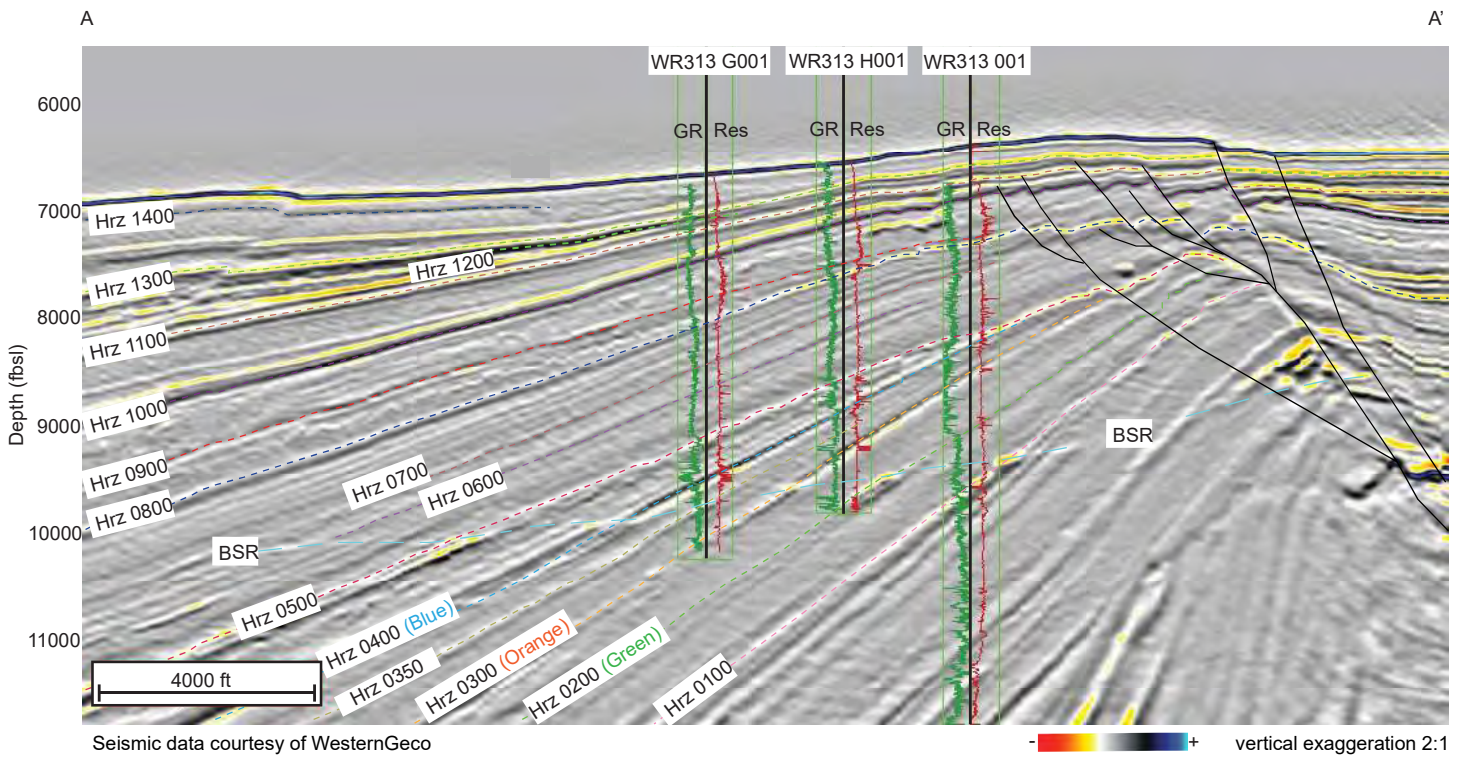


Figure F4: Seismic section A to A' through previously drilled boreholes in Walker Ridge Block 313 (WR313) (located in Figure F1). Seismic horizon (Hrz) nomenclature used in this study is delineated as 'Hrz #'. Previous nomenclature is shown in parenthesis (Boswell et al., 2012b; Frye et al., 2012; Hillman et al., 2017a). The bottom simulating reflections (BSRs), and logging while drilling (LWD) gamma ray (GR) and LWD resistivity (Res) logs of the previously drilled holes are also shown with values increasing to the right. Seismic data courtesy of WesternGeco.

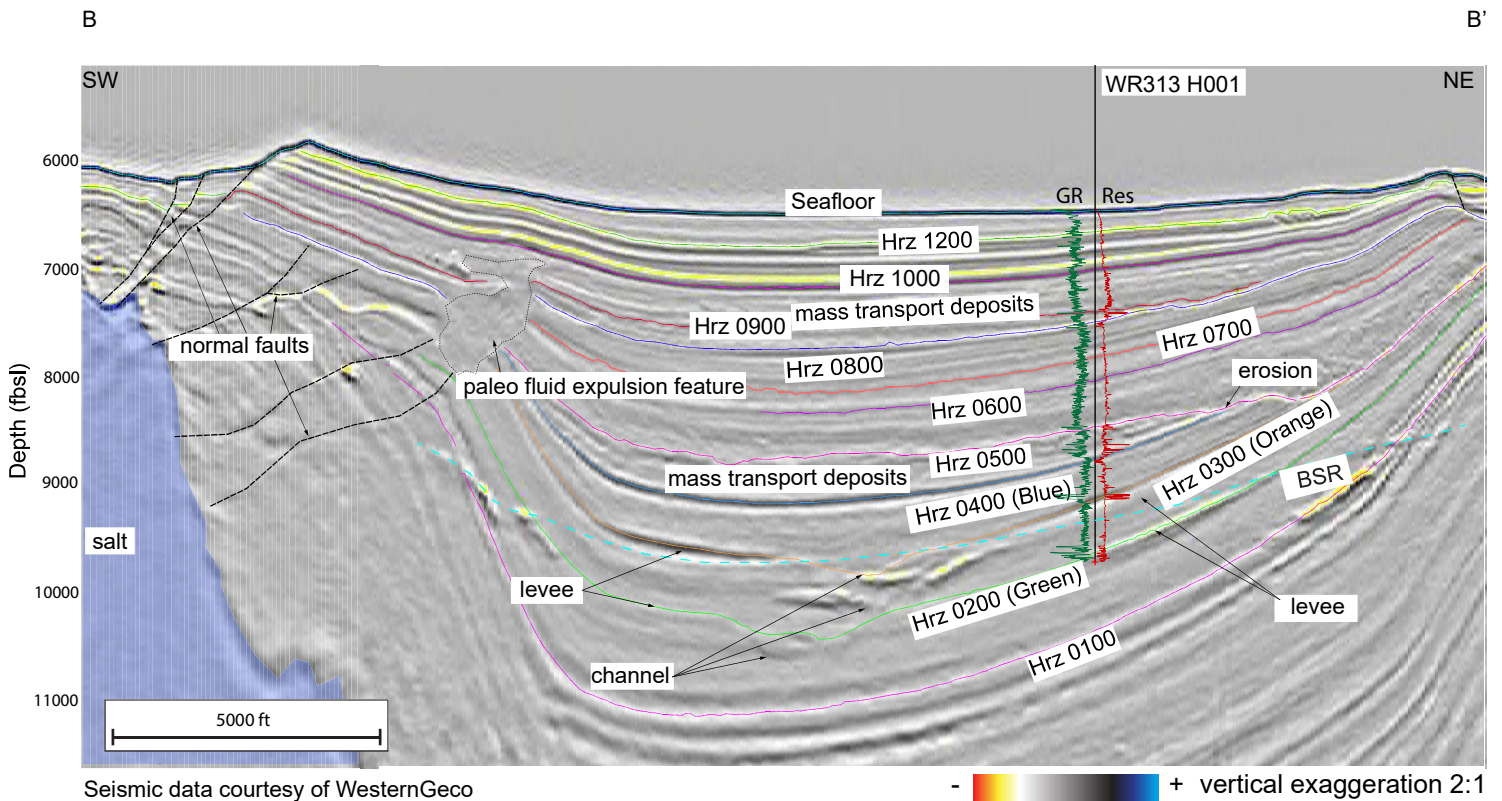


Figure F5: Southwest to northeast (SW-NE) oriented seismic section B to B' (located in Figure F2) through Hole H001 showing major seismic features in the study area. Logging while drilling (LWD), resistivity (RES), and gamma ray (GR) logs are shown at Hole H001 with values increasing to the right. Seismic data courtesy of WesternGeco.

Borehole	API Number	Surface Lat. (NAD27)	Surface Long. (NAD27)	Bottom Lat. (NAD27)	Bottom Long. (NAD27)
WR313 001	608124000700	26° 39' 32.83"	-91° 40' 11.66"	26° 39' 04.66"	-91° 40' 12.31"
WR313 G001	608124003900	26° 39' 47.48"	-91° 41' 01.94"	26° 39' 47.91"	-91° 41' 01.81"
WR313 H001	608124004000	26° 39' 44.85"	-91° 40' 33.75"	26° 39' 44.99"	-91° 40' 33.18"

Table T1: Surface and bottom-hole locations of previously drilled boreholes in WR313 (BSEE, 2024). API = American Petroleum Institute; NAD27 = North American Datum of 1927; WR313 = Walker Ridge Block 313; BSEE = U.S. Bureau of Safety and Environmental Enforcement

Borehole	API Number	Total MD (ft RKB)	TVD (ft RKB)	Air Gap (ft)	Water Depth (ft)
WR313 001	608124000700	16,720	16,072	72	6,216
WR313 G001	608124003900	10,200	10,199	52	6,562
WR313 H001	608124004000	9,888	9,887	51	6,462

Table T2: Total Depth, rig height (air gap), and water depth of previously drilled boreholes in WR313 (BSEE, 2024). API = American Petroleum Institute; TVD = Total Vertical Depth; MD = Measured Depth; WR313 = Walker Ridge Block 313; BSEE = U.S. Bureau of Safety and Environmental Enforcement

data and display a distinct phase reversal when they intersect the local BSR.

This phenomenon, described above, guided the project seismic mapping strategy. Each of these seismic horizons were traced as a seismic peak above the BSR and as a seismic trough below the BSR (See Boswell et al. (2012b) for an explanation of mapping strategy). In addition to the seismic horizons, a horizon was also generated connecting the discontinuous but locally strong BSR (Figure F4).

Hole G001, Hole H001, and WR313 001 penetrate the Hr3 0400 (Blue) above the BSR (Figure F6) whereas only Hole H001 and WR313 001 penetrate Hr3 0300 (Orange) above the BSR (Figure F7). These wells confirmed that positive seismic amplitudes above the base of hydrate stability record the presence of hydrates. Hole G001 penetrated Hr3 0300 (Orange) below the BSR. At this location, the Orange sand was mud prone and gas was not present. Frye et al. (2012), Boswell et al. (2012b), and Varona et al. (2023) interpret the specific depositional environments of the Blue and Orange sands.

Site H seismic and LWD interpretation

In preparation coring, LWD and seismic data were used to characterize the sediment type and hydrate occurrence at Hole H001. Five units ('LWD Units', e.g., Figure F8 and Table T3) were interpreted and the porosity along the borehole was calculated. Hydrate saturation within coarse-grained sediments was also calculated. Figures F9 and F10 show the planned primary coring intervals: the shallow near-seafloor system (Figure F9), the Red sand (Figure F10, top), the Upper Blue sand (Figure F10, middle) and the Orange sand (Figure F10, bottom).

In borehole or LWD data, water-saturated and gas hydrate-saturated sediments have unique signals. Water-saturated, unconsolidated, coarse-grained sediments usually wash out of the borehole during drilling and coring, leading to a very low LWD resistivity (often lower than the rest of borehole), enlarged caliper measurements, low bulk density and low gamma ray. In comparison, water-saturated marine muds usually have stable borehole size, a resistivity between 1-2 Ω m, and a mid-range gamma ray (between 60-120 API). Hydrate-saturated coarse-grained sediments have high resistivity, high P-wave velocity, little to no change in bulk density, and low gamma ray. This set of log responses indicates that hydrate is in the primary pore space of coarse-grained sediments.

In contrast, hydrate in marine muds often forms in near-vertical fractures, and these have been observed at Hole H001 (Cook et al., 2014). These intervals have high resistivity, hydrate-filled fractures visible on resistivity image logs, and separation between

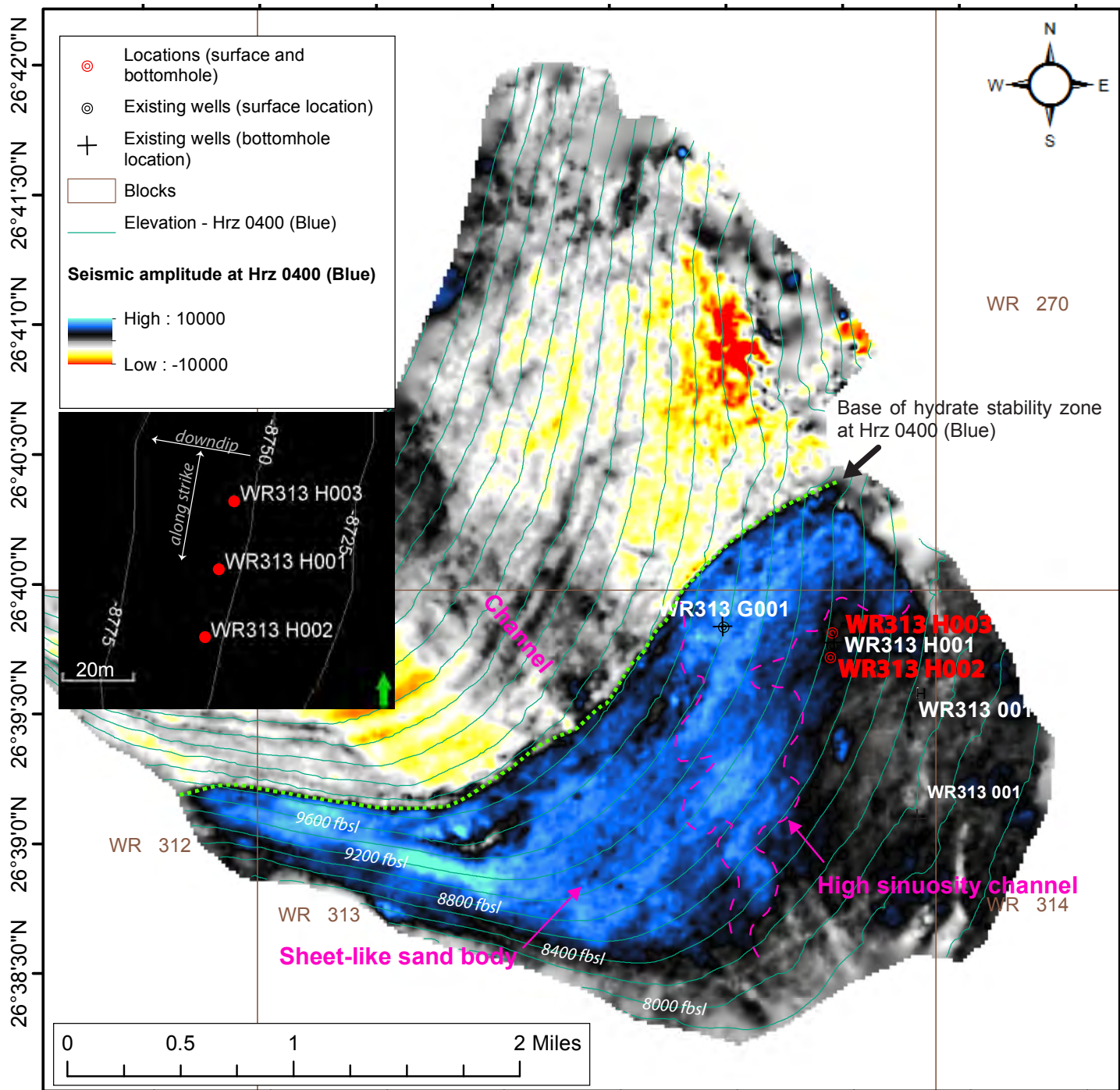


Figure F6: Instantaneous amplitude map of Horizon (Hrz) 0400 (Blue) Walker Ridge Block 313 (WR313) showing the geological interpretation of the lower part of the Blue sand interval (Boswell et al., 2012b). Inset illustrates an expanded view of the H001 location illustrating the two holes (H002 and H003) drilled in this study. The lower portion of the Blue sand does not extend to Hole H001. The top of the Blue sand interval (Upper Blue) was encountered in Hole H001 with a total thickness of 52 ft. Maps generated from three-dimensional (3D) seismic data used with permission of WesternGeco.

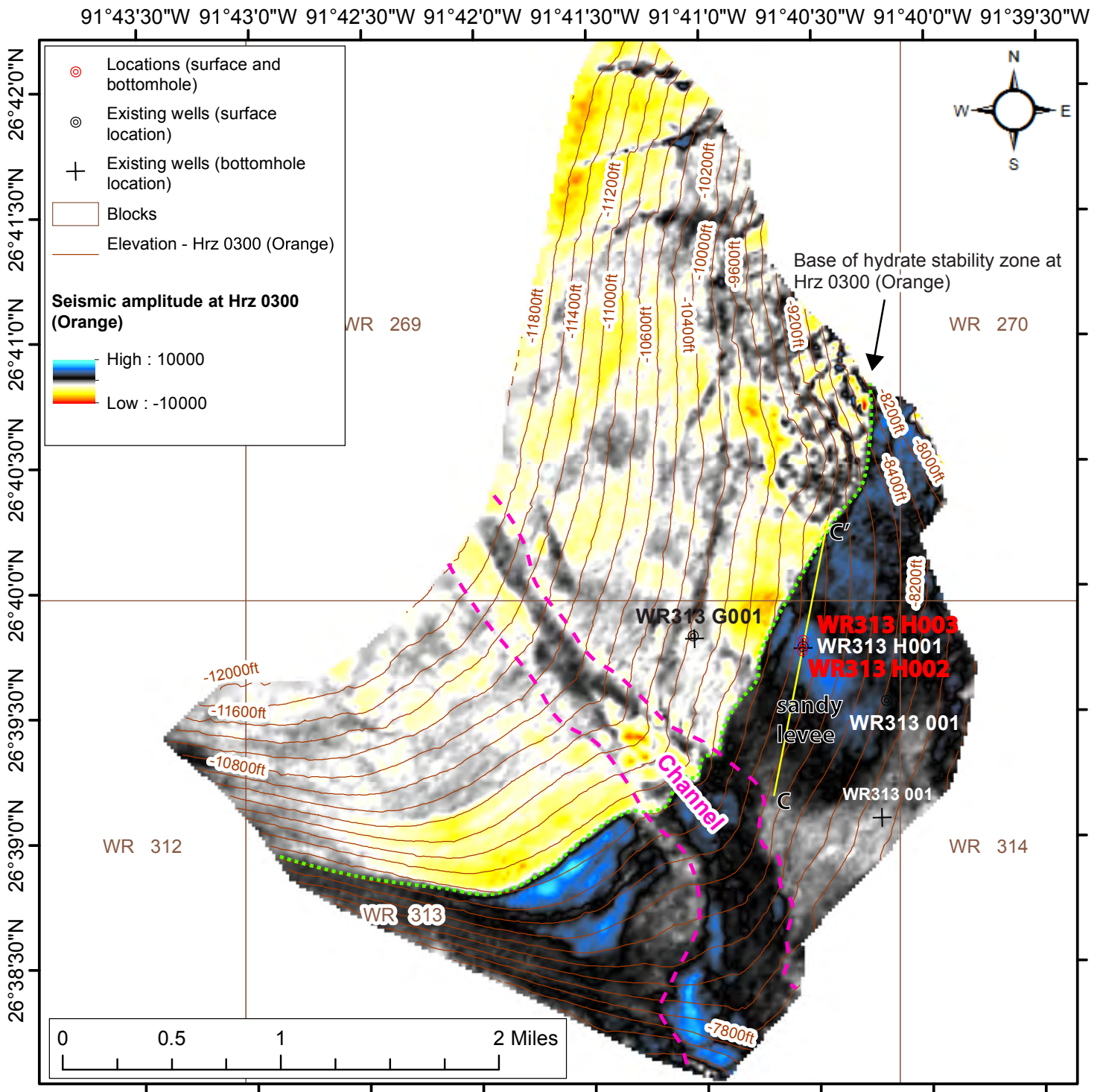


Figure F7: Instantaneous amplitude map of Horizon (Hrz) 0300 (Orange) Walker Ridge Block 313 (WR313) showing geological interpretation for the Orange sand. Previously-drilled Hole H001 and the proposed Hole H002 and Hole H003 target gas hydrate-bearing sands showing strong positive amplitude response (in blue). Maps generated from three-dimensional (3D) seismic data used with permission of WesternGeco.

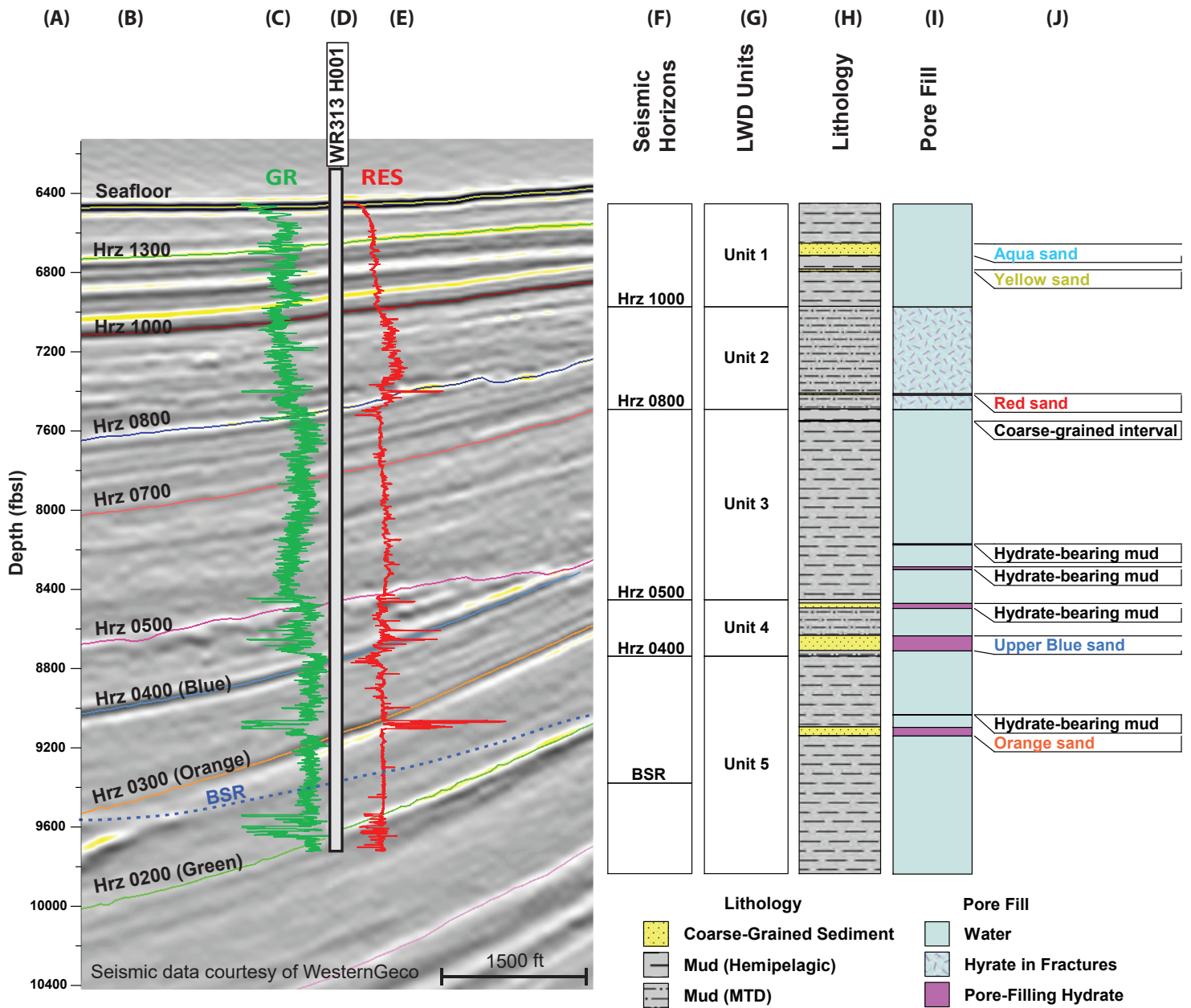


Figure F8: Stratigraphic overview of Hole H001. A) Depth in feet below sea level (fbsl); B) Seismic cross section running through Hole H001 with major seismic horizons (Hrz) labeled on the left-hand side; C) Logging while drilling (LWD) gamma ray (GR) with GR value increasing to the right; D) Location of Hole H001 on the seismic cross section; E) LWD resistivity (RES) with values increasing to the right; F) Seismic horizons as described in Table T3; G) LWD units and bottom-simulating reflector (BSR) defined by LWD and seismic data; H) Interpreted lithology; I) Interpreted pore fill; J) Interpreted sands and other events from Table T3.

propagation resistivity curves (Cook et al., 2010). The high resistivity observed in these intervals, however, is caused by electrical anisotropy and not uniformly high hydrate saturation.

Hydrate saturation (S_h) is calculated using Archie's equation (Equation E1) in coarse-grained intervals only, as Archie's equation is not accurate when vertical fractures or vugs are present (Archie, 1942; Goldberg et al., 2010).

$$S_h = 1 - \left(\frac{R_w}{\phi^m R_{RING}} \right)^{\frac{1}{n}}$$

Equation E1

To calculate hydrate saturation, the LWD resistivity log with the highest vertical resolution for its depth of penetration, which is ring resistivity, R_{RING} (R-RING) (Cook et al., 2012) was used. Water resistivity, R_w , is calculated using Fofonoff and Millard (1983). The Archie tortuosity exponent, m , is estimated from

WR313 H001					
Events, Sands & LWD Units		Depth (mbsf)	Depth (fbsl)	Depth (ft RKB)	
Seafloor		-	6,462	6,513	
Hrz 1200		LWD Unit 1	61	6,715	
Water-bearing Aqua sand	Top		61	6,715	
	Base		80	6,777	
Hrz 1100			101	6,846	
Water-bearing Yellow sand	Top		101	6,846	
	Base	105	6,857		
Hrz 1000		158	6,982	7,033	
JIP mud unit with low concentration hydrate	Top	LWD Unit 2	158	7,033	
Hrz 0900			292	7,471	
Hydrate-bearing Red sand	Top		292	7,471	
	Base		294	7,479	
JIP mud unit with low concentration hydrate	Base		316	7,551	
Hrz 0800		316	7,500	7,551	
Water-bearing coarse-grained interval	Top	LWD Unit 3	334	7,609	
	Base		335	7,613	
Hydrate-bearing marine mud	Top		523	8,229	
	Base		525	8,235	
Hydrate-bearing marine mud	Top		558	8,345	
	Base		563	8,359	
Hrz 0500			610	8,462	8,513
Water-bearing coarse-grained interval	Top		LWD Unit 4	615	8,530
	Base	622		8,555	
Hydrate-bearing Upper Blue sand	Top	664		8,693	
	Base	688		8,769	
Hrz 400		696	8,747	8,798	
Hydrate-bearing marine mud	Top	LWD Unit 5	786	9,091	
	Base		786	9,093	
Hrz 0300			805	9,155	
Hydrate-bearing Orange sand	Top		805	9,155	
	Base		819	9,199	
Interpolated BSR			895	9,397	9,448

Table T3: Mapped seismic horizons and major stratigraphic surfaces in Hole H001. Logging while drilling (LWD) units are as described in the text. JIP = 2009 Gas Hydrates Joint Industry Project Leg II; Hrz = horizon; mbsf=meters below seafloor; fbsl = feet below sea level; ft RKB = feet below rotary kelly bushing or rig floor when no bushing is present

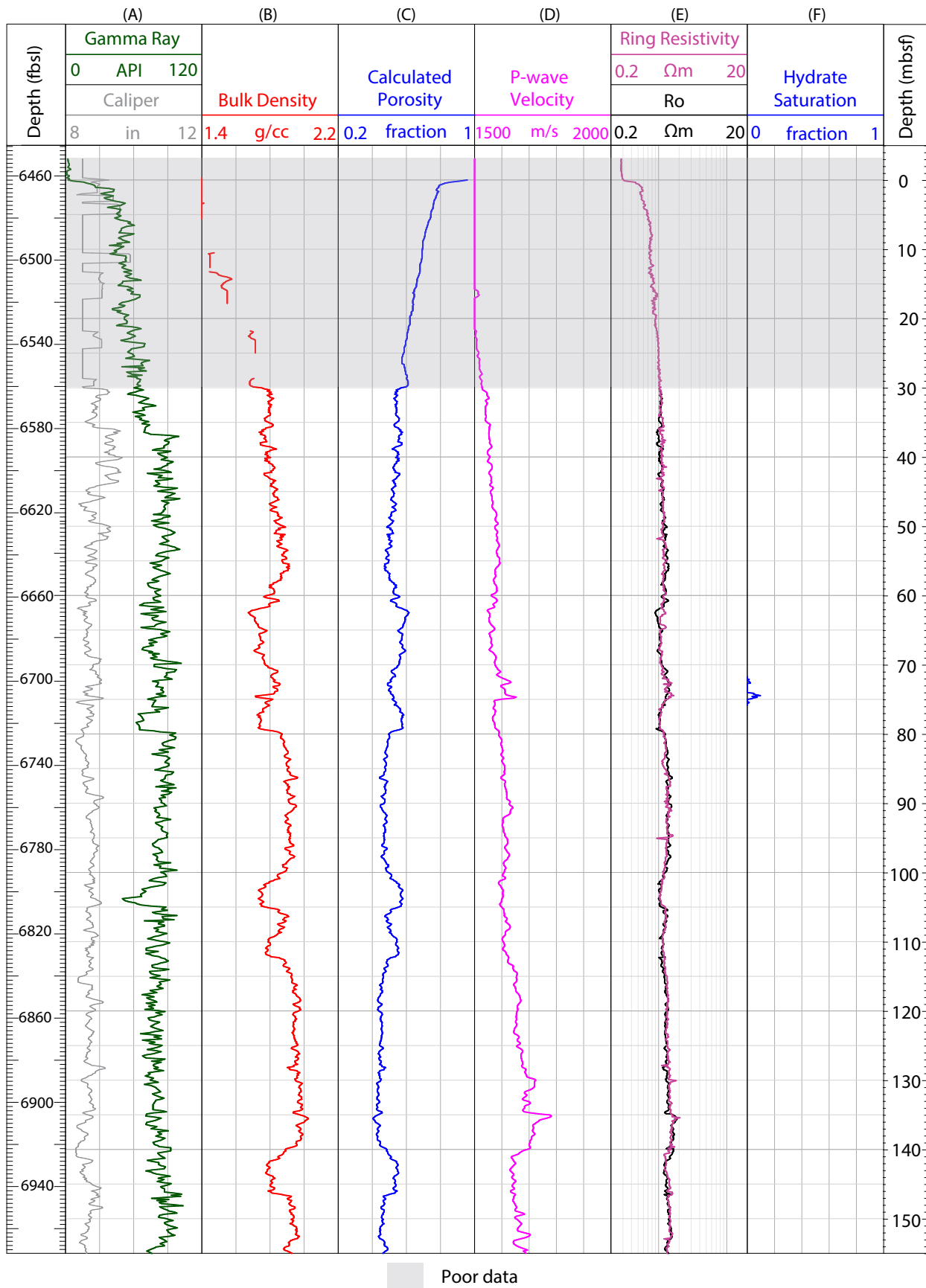


Figure F9: Hole H001 logging while drilling (LWD) data for the uppermost interval (0-150 mbsf), LWD Unit 1 with calculated porosity and hydrate saturation. The top interval is gray because the LWD data in the near-seafloor interval are of poor quality; A) LWD gamma ray (green line) and caliper data (gray line); B) LWD bulk density (red line); C) LWD calculated porosity (blue line); D) LWD P-wave velocity (pink line); E) LWD ring resistivity (light purple line) and formation resistivity with 100% water (R_0); F) Calculated hydrate saturation.

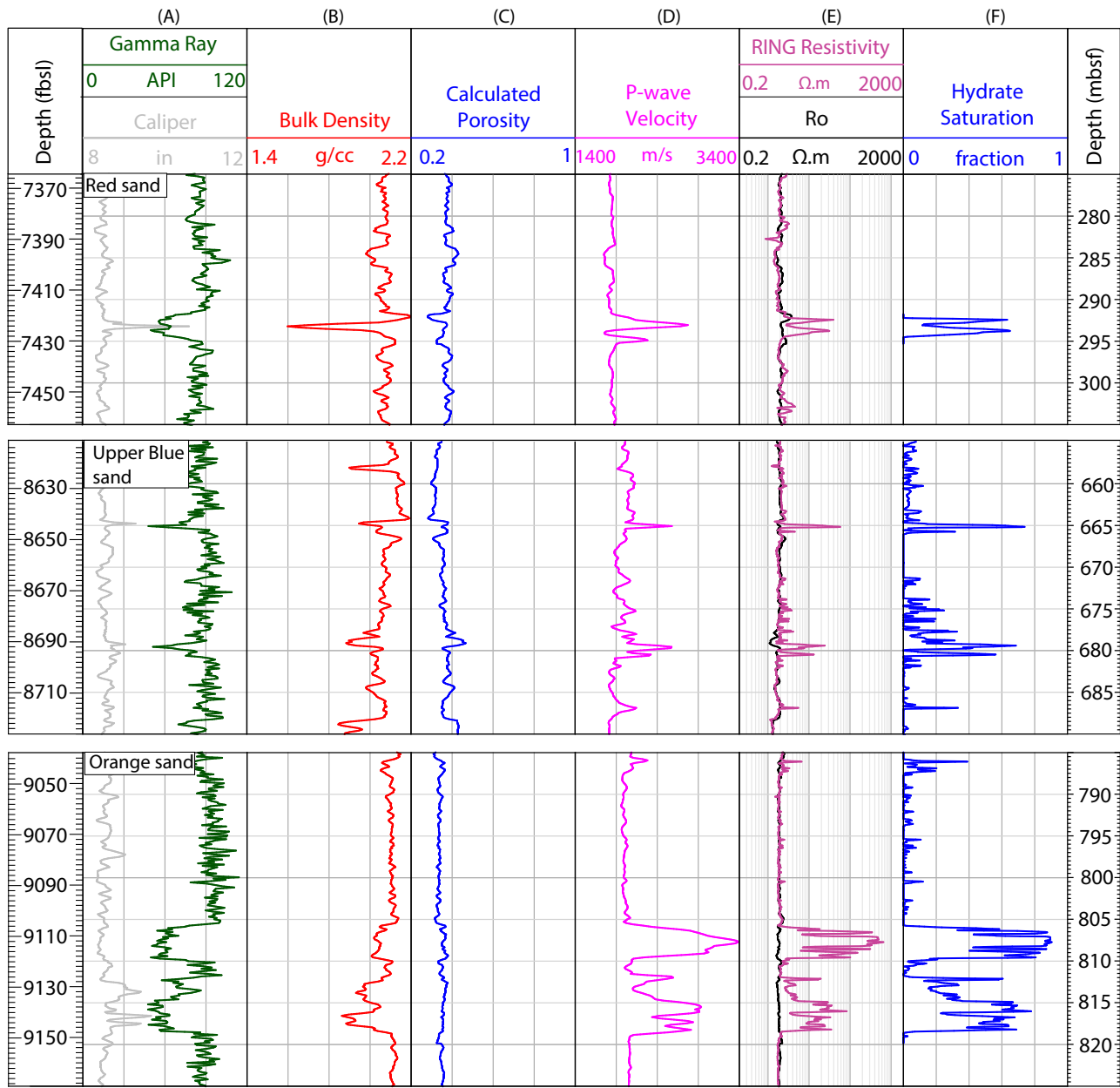


Figure F10: Hole H001 logging while drilling (LWD) data in sand intervals including the Red sand (LWD Unit 2), the Upper Blue sand (in LWD Unit 4), and the Orange sand (in LWD Unit 5) with calculated porosity and hydrate saturation; Hole H001 A) LWD gamma ray (green line) and caliper data (gray line); B) LWD bulk density (red line); C) LWD calculated porosity (blue line); D) LWD P-wave velocity (pink line); E) LWD ring resistivity (light purple line) and formation resistivity with 100% water (R_o); F) Calculated hydrate saturation.

water-saturated intervals and ranges from 1.9 to 2.5 for Hole H001. The hydrate saturation exponent, n , is set to 2.5 (Cook and Waite, 2018).

Finally, the porosity, ϕ is calculated from LWD bulk density using a pore water density of 1.03 g/cc, a hydrate density of 0.925 g/cc, and grain density of 2.65 g/cc for coarse-grained intervals and 2.7 g/cc for muds (Figures F9 and F10). These are common values used for the Gulf of Mexico and resemble those measured for Green Canyon Block 955 (Fang et al.,

2020). In zones of borehole washout, the bulk density was very low. In these zones, the porosity was edited to reflect what was present in similar lithologies in nearby intervals.

The five LWD units defined at Hole H001 using LWD and seismic data (Figure F7 and Table T3) include:

LWD Unit 1 extends from the seafloor to Hr_z 1000 (0-6,982 fbsl [0-158 mbsf]). In the seismic data, LWD Unit 1 is imaged as sub-parallel reflections. The LWD data has a high gamma ray response indicating

marine mud with few relatively thin lower gamma ray intervals. LWD Unit 1 is interpreted as a fine-grained hemipelagic interval with variable bulk density. Down dip, in Hole G001, the lower-density intervals contain several centimeter- to meter-thick coarse-grained beds, identified as the Aqua and Yellow sands; however, these sands are either not present or very thin at Site H. One thin interval at 74 mbsf was identified that may be a coarse-grained hydrate bearing sand; if it contains hydrate, it is at a low saturation, <10% (Figure F9).

LWD Unit 2 extends from Hrз 1000 to Hrз 0800 (6,982-7,500 fbsl [158-316 mbsf]); on the LWD logs, gas hydrate was identified in this interval in near-vertical fractures. The gamma ray in LWD Unit 2 is slightly lower than in the overlying section. Based on discontinuous and chaotic seismic reflections of variable amplitude, this section may be a mud-rich mass transport deposit (MTD). Near the bottom of Unit 2, a 2.5-m thick sand layer named the Red sand has the first high saturation hydrate in Hole H001 (Figure F10, top).

LWD Unit 3 underlies Unit 2 and extends from Hrз 0800 to Hrз 0500 (7,500-8,462 fbsl [316-610 mbsf]). In seismic data, LWD Unit 3 is characterized by continuous parallel reflections of moderate amplitude; the corresponding section in Hole H001 LWD has high gamma ray that changes to slightly lower gamma ray in the lower part of LWD Unit 3. LWD Unit 3 is interpreted as a hemipelagic mud-dominated section.

LWD Unit 4 extends from Hrз 0500 downward to Hrз 0400 (Blue) (8,462-8,747 fbsl [610-696 mbsf]). Hrз 0500 is a strong seismic reflector, that truncates underlying stratigraphy, marking an erosional surface (Figure F5, label erosion). Hrз 0500 is associated with abrupt increase in gamma ray with depth. The seismic reflection data within the lower-most section of LWD Unit 4, below Hrз 0500 is characterized by discontinuous reflections with variable amplitude. This section is interpreted as mass transport deposits (MTD), which may be silt-rich mud as indicated by moderately low gamma ray. Very thin low gamma-ray

and low resistivity streaks within this zone indicate presence of thin water-bearing coarse-grained intervals. The hydrate-bearing Upper Blue sand (Figure F10, middle) is near the base of this interval.

LWD Unit 5 starts at Hrз 0400 (Blue) (8,747 fbsl [696 mbsf]). The lower part of the Blue sand is not present at Hole H001. LWD Unit 5 contains Hrз 0300 (Orange), as indicated by low gamma ray values, and correlates to the top of the Orange sand. High resistivity, high P-wave velocity and low density in the Orange sand indicates the presence of pore-filling, high saturation gas hydrate (Figure F10, bottom) (Frye et al., 2012, Collett et al., 2010); the hydrate saturation in the Orange sand is the highest of all the sands in Hole H001 (Figure F10, bottom).

Geothermal gradient and thermodynamic conditions

In-situ temperatures were estimated at Hole H001 (Figure F11). The estimated temperature was based on the following assumptions:

- At the depth of the interpolated bottom simulating reflector, methane is in three phase equilibrium (vapor-liquid-hydrate). The three-phase equilibrium for methane hydrates was derived using the model developed by Moridis et al. (2012).
- The pore fluid salinity is that of seawater (35 ppt).
- The pore pressure is hydrostatic and follows a gradient of 0.446 psi/ft (i.e., a fluid density equal to 1.03 g/cm³).
- The seafloor temperature is 39.2° F (4.0° C) (Boyer et al., 2018).
- Temperature increases linearly with depth from the seafloor to the base of the hydrate stability zone.

The predicted in-situ temperature at Hole H001 is shown as a green dashed line in Figure F11. The BSR at Hole H001 is interpreted to be at ~9,397 fbsl. Based on this, at Hole H001, the temperature at the base of the hydrate stability zone is estimated to be

68.2° F (20.1° C) and the gradient to be 9.6° F/1,000 ft (17.5° C/km). The LWD temperatures acquired during the drilling of Hole H001 (green solid line in Figure F11) illustrate that the borehole temperature during drilling is less than the formation temperature because colder fluids were being circulated downhole.

Hazards

Hole H001 was interpreted to have intersected all hydrate-bearing reservoir sand units within the hydrate stability zone, and no free gas was interpreted to be present. No gas flow was encountered while drilling Hole H001 and Hole G001 during JIP II (Collett et al., 2009). LWD Units 1, 2 and 3 are interpreted to contain thin, wet, silty sands that dip basinward. These are possible shallow water flow sands. However, no shallow water flow was recorded during drilling of Hole H001 (Collett et al., 2009) or in WR313 001. Therefore, it was interpreted that there was low risk for water flow at Site H.

Pore pressure and fracture gradient

There was no indication of abnormal pressure when Hole G001 was drilled (Collett et al., 2010). However, at Hole G001, at depths greater than 8,264 ft RKB, it was necessary to pump and rotate the drill string while simultaneously pulling out of the borehole and it was interpreted that the borehole was closing on the bottom-hole assembly (BHA). At 9,244 ft RKB a major blockage of flow occurred. Thereafter, the water-based mud weight was raised to 10 ppg and pumped continuously. At a depth of 9,599 ft RKB, the water-based mud weight was raised to 10.5 ppg. Thereafter, the well was drilled without incident (Collett et al., 2010). The subsequent Hole H001 was drilled with 10.5 ppg below 8,501 ft RKB without incident.

Pre-drill pore pressure and fracture gradient profiles were constructed for Site H (Figure F12). The overburden stress (σ_v) was generated by integrating the density log from the LWD data in Hole H001. Pore pressures were assumed to be hydrostatic (u_h)

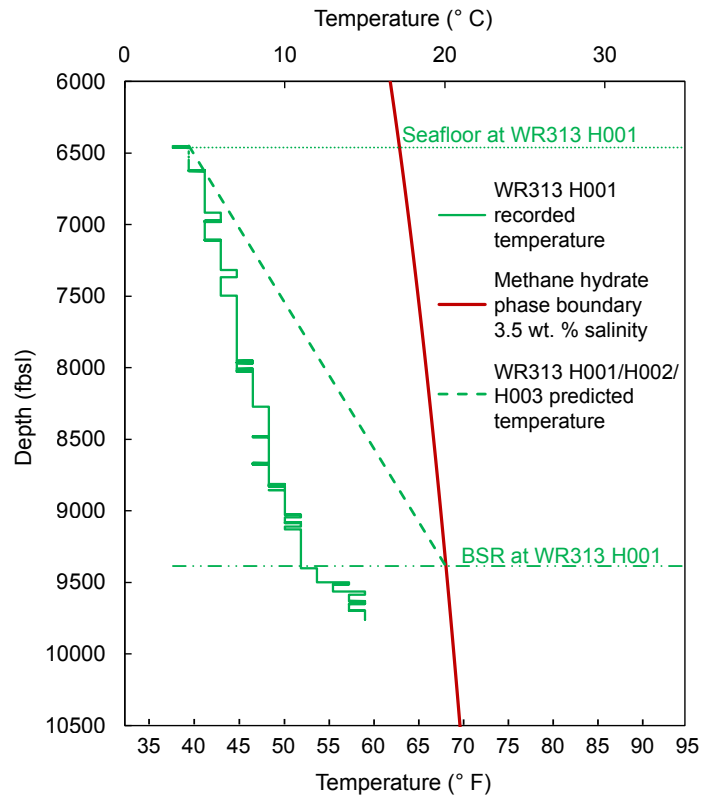


Figure F11: Estimated temperature profile from the seafloor to the BSR at Walker Ridge Block 313 Hole H001 (green dashed line). Solid green line illustrates the logging while drilling (LWD) borehole temperature. The phase boundary for methane hydrate is delineated by the red line: hydrate is stable to the left of this line and not stable to the right. The horizontal green dash-dot line records the depth of the bottom-simulating reflections (BSRs). The system is assumed to be at the three-phase boundary at this depth.

because of the lack of evidence for elevated pore pressures while drilling Hole H001. The hydrostatic pore pressure (u_h) profile was expressed with a pore pressure gradient of 8.95 ppg (0.465 psi/ft). This hydrostatic gradient is slightly larger than the previously assumed 0.446 psi/ft. However, it reflects common practice in the drilling industry and was used in permitting the well. The least principal stress (σ_{hmin}) was estimated using:

$$\sigma_{hmin} = K * (\sigma_v - u_h) + u_h$$

Equation E2

Equation E2 is commonly used to model the fracture gradient (Eaton, 1969; Flemings, 2021b). An upper bound of $K = 0.9$ and a lower bound of $K = 0.7$ was assumed.

To avoid borehole closer at deeper depths when

a weighted mud is not used as occurred for G001 (Collett et al., 2010), the plan was to increase the drilling fluid weight at a depth of 8,113 ft RKB by

switching to a 10.5 ppg water-based mud (Figure F12, gray horizontal line).

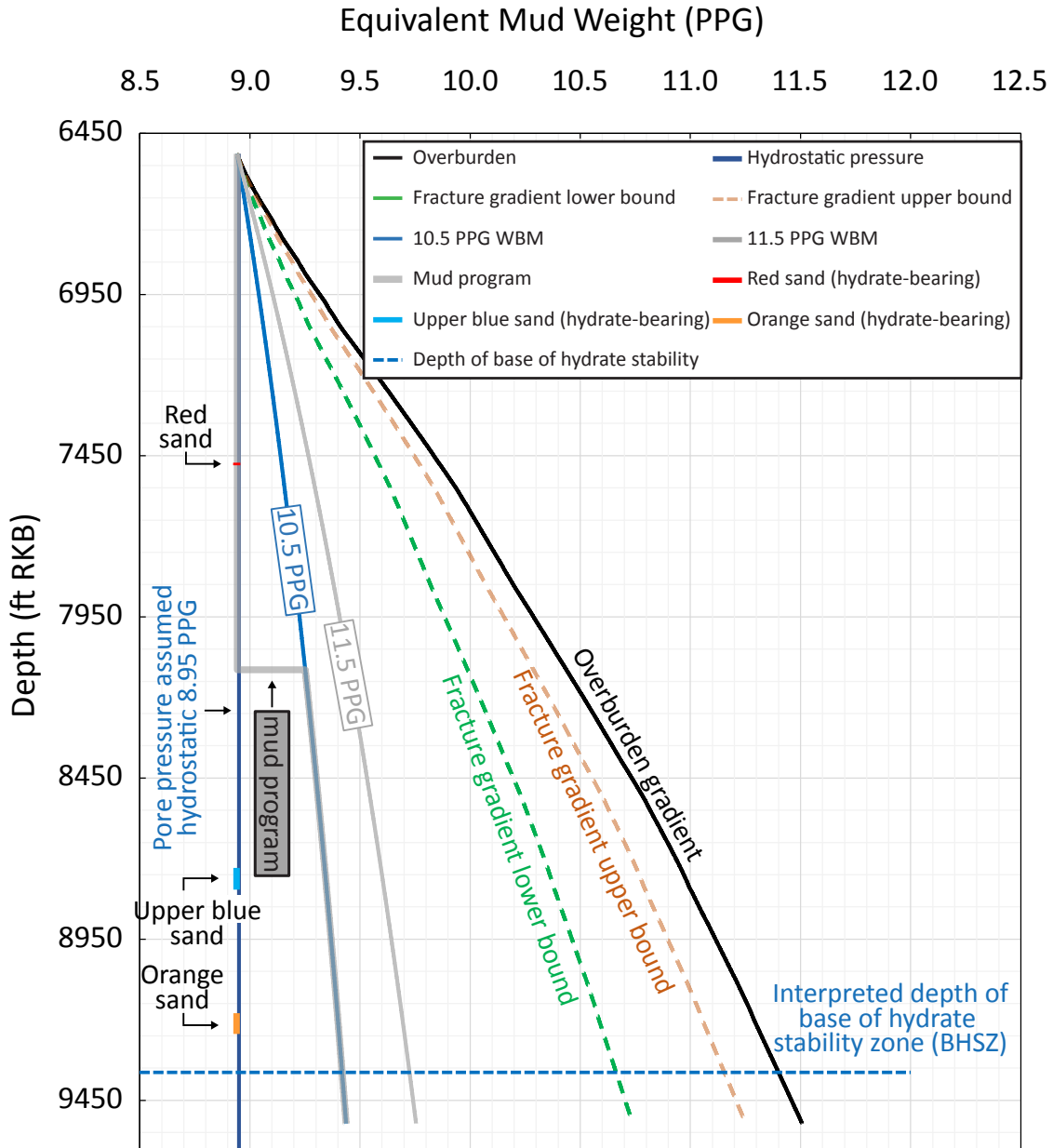
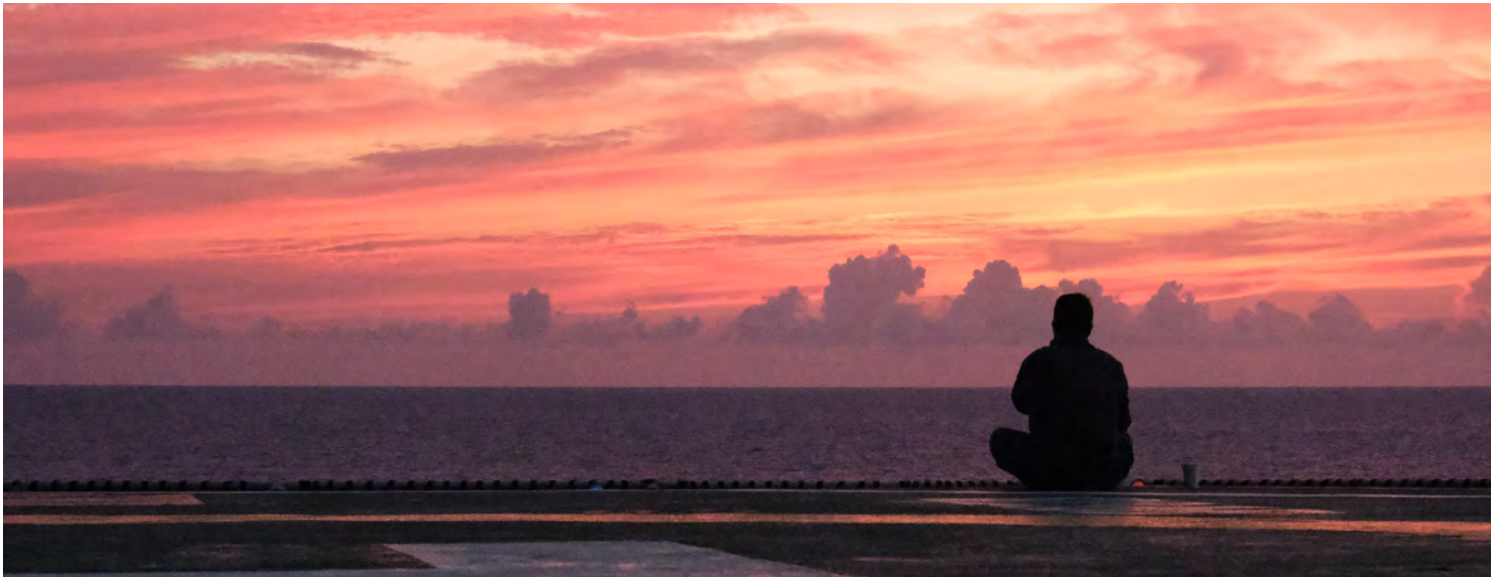


Figure F12: Pressure and fracture gradient plot for Site H at Walker Ridge Block 313 (WR313). The pore pressure is assumed to be hydrostatic (solid blue line). The overburden is shown with a solid black line. The fracture pressure is inferred to lie between the green and tan dashed lines based on assuming $K = 0.7$ and 0.9 in Equation E2. The planned mud program (gray solid line) shows the increase in mud weight to 10.5 ppg water-based mud (WBM) at 8,113 ft rotary kelly bushing or rig floor when no bushing is present (RKB).



A UT-GOM2-2 science party member enjoys the sunset while relaxing on the Helix Q4000 helipad. Photo credit: Peter B. Flemings

Science objectives

The goals of this expedition were to better understand the potential of deepwater marine hydrate reservoirs to serve as an energy resource (See [Gas hydrates and energy](#)) and to illuminate the role of the marine hydrate system in the carbon cycle (See [Gas hydrates, the global carbon cycle, and the microbial factory](#)).

To accomplish these goals, we wished 1) to understand how coarse-grained hydrate reservoirs form and how carbon cycles through this sedimentary system where hydrate reservoirs reside, and 2) to understand the geological and petrophysical properties of the coarse-grained hydrate reservoir and its seals. These goals led to 5 principal prioritized objectives described below.

1. Characterize the Orange sand and Upper Blue sand hydrate reservoirs and their bounding units by determining:
 - hydrate saturation, dissolved methane concentration, and gas composition
 - pore water solute concentration and composition
 - sediment type (mineral and clay composition), grain size, and sorting
 - compressibility
 - strength behavior
 - sediment composition and age
 - microbial communities and activity
2. Obtain vertical high-resolution geochemical and sedimentary profiles by continuously coring to 500 fbsl and including:
 - pore water
 - sedimentology
 - physical properties
 - microbiological properties
 - mechanical properties
3. Measure the in-situ temperature and pressure profile
 - measure temperature with the advanced piston corer temperature tool (APCT-3)
 - measure both temperature and pressure with a pore pressure penetrometer
4. Characterize the dissolved methane concentration and analyze the gas molecular and isotopic compositions with depth by collecting pressurized core samples and quantifying the gas content.
5. Describe occurrences of hydrate-bearing thin sands < 3-m thick and hydrate-bearing near-vertical fractures in marine muds which also occur at WR313.



The Ohio State University professor Ann E. Cook talks science with The University of Texas at Austin student Ethan Petrou on the Helix Q4000 helipad. Photo credit: Jesse Houghton

Planning

DOE project development and structure

In the Spring of 2014, The University of Texas at Austin (UT) partnered with The Ohio State University, Columbia University, and the Consortium for Ocean Leadership and responded to a funding opportunity announcement from the U.S. Department of Energy (DOE). UT was selected and a cooperative agreement titled Deepwater Methane Hydrate Characterization and Scientific Assessment (DOE Award No. DE-FE0023919) was initiated, with UT as the prime recipient. Over the following decade, UT worked with seven universities (The Ohio State University, Columbia University, University of New Hampshire, Oregon State University, University of Washington, Tufts University, and Colorado School of Mines), the DOE, the DOE National Energy Technology Laboratory (NETL), the United States Geological Survey (USGS), and the U.S. Bureau of Ocean Energy Management (BOEM) to implement the project.

A six-phase program, including the initial hydrate coring expedition UT-GOM2-1 (Flemings et al., [2018a](#)) and multiple land tests (Flemings et al., [2016](#); Flemings et al., [2020a](#); Price et al., [2021](#)) was designed that culminated in the planning and execution of UT-GOM2-2 to target methane hydrates in coarse-grained reservoirs on the US continental margin in the Gulf of Mexico.

During Phase 1 (Flemings et al., [2016](#)), potential field coring sites were identified. Each site was examined using geophysical and geologic data and prioritized using criteria developed with DOE. Following the site selection process, a draft pre-expedition drilling, coring, and sampling operational plan was developed.

During Phase 2 (Flemings et al., [2018a](#)), a land-based field test of the Pressure Coring Tool with Ball Valve (PCTB) was conducted (Flemings, [2020a](#)). UT developed the capability to transport, store, manipulate, and analyze pressure cores. A Marine Field Test (UT-GOM2-1) was planned and executed in the Gulf of Mexico, Green Canyon Block 955 (GC955), to test the PCTB in a deepwater marine environment (Flemings, [2021a](#)). UT-GOM2-1 not only tested the PCTB but accomplished numerous scientific objectives in understanding the hydrate

reservoir at GC955. UT-GOM2-1 pressure cores were transported to land-based laboratory facilities, stored, subsampled, and characterized.

During Phase 3, pressure cores recovered during UT-GOM2-1 underwent analysis and experimentation. UT expanded and refined their internal pressure core analytical capabilities (Flemings et al., [2020a](#)). Science and operational plans for the UT-GOM2-2 hydrate coring expedition were refined and UT continued to pursue access to a drilling vessel supporting the planned expedition. Further PCTB lab testing was performed, and engineering upgrades were implemented.

During Phase 4, analysis of the pressure cores acquired during UT-GOM2-1 continued. Further engineering modifications to the PCTB were made and a second land-based test of the PCTB was performed. The science and operational plans for UT-GOM2-2 hydrate coring expedition were refined. UT continued efforts to obtain access to a suitable vessel for UT-GOM2-2, and pre-expedition contracting, procurement, and permitting was initiated.

During Phase 5, the science and operational plans for the UT-GOM2-2 expedition were finalized and UT contracted with Helix Energy Solutions in support of UT-GOM2-2 Operations. A final land-based test of the PCTB was performed, and the PCTB was upgraded to the final design prior to deployment. Regulatory obligations, permitting, certifications, equipment, and supply preparations for UT-GOM2-2 were completed, the Operational Plan (Flemings et al., [2023b](#)) and Prospectus (Flemings et al., [2023a](#)) were published, and UT-GOM2-2 was executed in the Gulf of Mexico.

In Phase 6, currently underway, cores acquired from UT-GOM2-2 have been analyzed at UT and distributed to numerous institutions. Scientific analysis of methane hydrate reservoirs will continue, including sample and data distribution, collaborative analysis of geologic data, archiving of data and findings in dedicated scientific volumes, and technical presentations. A summary of drilling and sample

procurement procedures, as well as scientific results, will be archived and will be made publicly available at [UT-GOM2-2: Gulf of Mexico Deepwater Hydrate Coring Expedition](#).

This report describes the planning, execution, and results of the marine gas-hydrate science expedition designated as UT-GOM2-2, completed during Phase 5 of the project.

Proposed borehole locations and sampling program

For UT-GOM2-2, two ‘twinned’ boreholes were planned adjacent to Hole H001. Many trade-offs were considered in developing the drilling and coring program including the priority to obtain pressure cores from the Orange sand interval, the availability of key scientific staff, the ability to adjust operational plans depending on the outcome of completed goals, and whether coring of the deeper sands should be planned in the same or different boreholes as coring of the shallow muds.

Both pressure coring using the PCTB, and conventional coring using Geotek’s Advanced Piston Corer (G-APC) and eXtended core barrel (G-XCB), were planned with the goal of acquiring samples of shallow and background muds, bounding muds, and hydrate-bearing sands. Pressure cores would be processed using Geotek’s Pressure Core Analysis and Transfer System (PCATS) to log and x-ray the pressure cores and subsample the recovered pressure cores at hydrate-stable conditions. Subsamples would undergo quantitative degassing to determine dissolved methane concentration and hydrate saturation.

Conventional cores would be processed on board and as soon as possible after the expedition at dockside labs established in Salt Lake City, Utah. Onboard, sections of conventional and depressurized core would be cut for microbiology and pore water analysis. Sections for pore water analysis would be squeezed and ephemeral pore water measurements would be completed on board. Void, pressure core, and headspace gas samples would be collected.

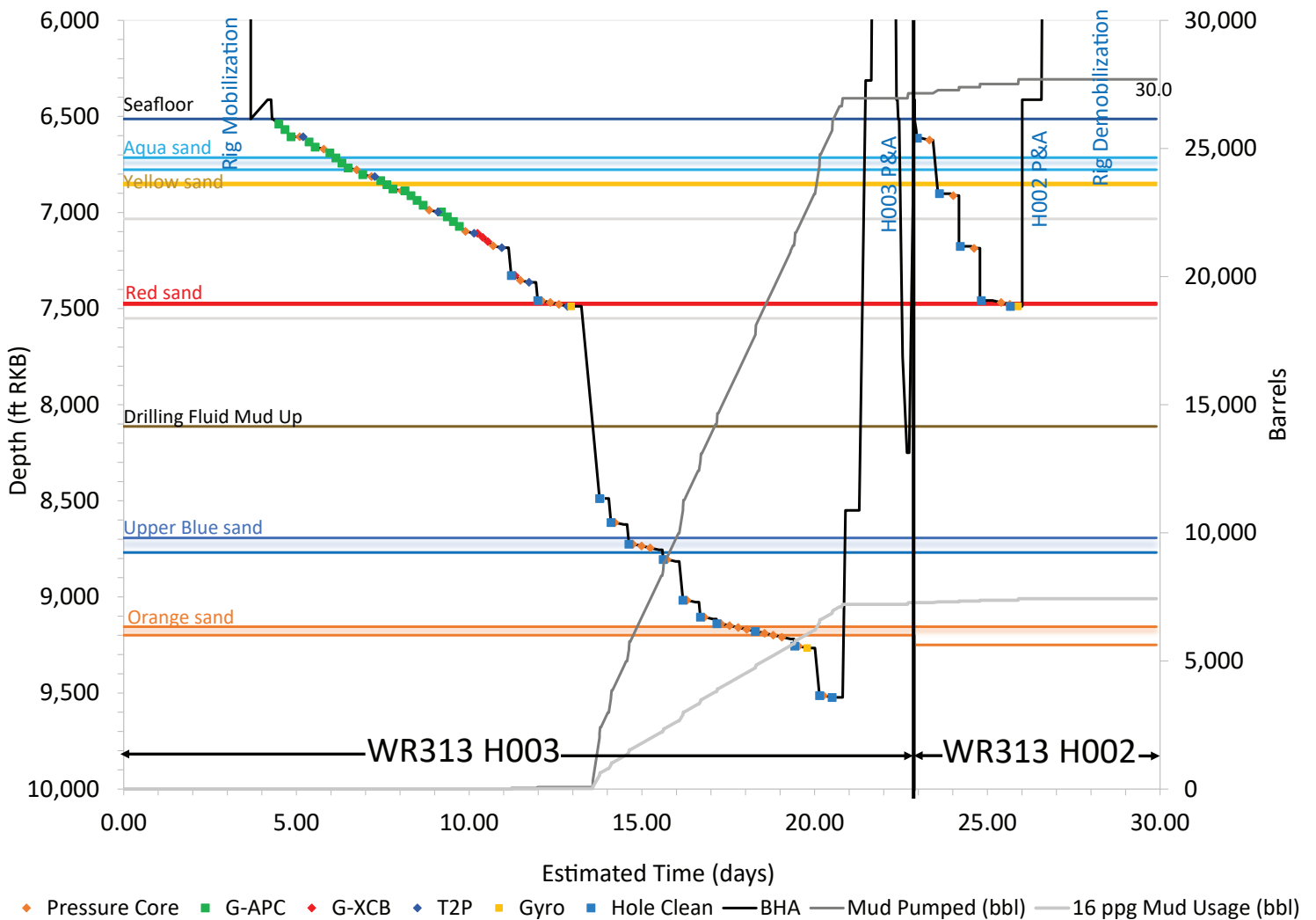


Figure F13: Predicted depth versus time for the duration of UT-GOM2-2, including rig mobilization, at Walker Ridge Block 313 (WR313) Hole H003 drilling and coring, Hole H003 plug and abandonment (P&A), Hole H002 drilling and coring, Hole H002 P&A, and Rig demobilization. Bit depth is shown as a solid black line (ft RKB using a water depth of 6,462 ft and a rig height of 51 ft). Geotek Advanced Piston Corer (G-APC) deployments are shown as green squares. Geotek eXtended Core Barrel (G-XCB) deployments are shown as red diamonds. Pressuring coring deployments are shown as orange diamonds. The depth of transition for switching from APC to XCB coring was predicted but not known. Gyroscopic measurements are shown as yellow squares and borehole cleans as blue squares. Estimated 16 ppg water-based mud usage (not including mud used for P&A) is shown as a dashed light gray line. Estimated 10.5 ppg water-based mud usage (not including mud used for P&A) is shown as a dashed dark gray line. Sand depths described in Table T3 are shown as aqua blue, yellow, red, blue, and orange horizontal lines. Estimated time include 20% downtime. Figure based on *Operations Plan 2.3* (Flemings et al., 2023b).

Figure F13 shows the planned depths for drilling, coring, penetrometer, and gyroscope measurements versus predicted time for the expedition. Hole H003 was to be drilled and cored from the seafloor to 3,010 fbsf. Conventional coring, including G-APC and G-XCB coring, was planned to capture high resolution geochemical, microbiological, and physical property profiles. Pressure coring was planned to capture the dissolved methane concentration profile and LWD log inferred low to high density transitions in mud-rich sedimentary section.

Targeted pressure coring was to be conducted to capture targets of interest including the Red, Upper Blue, and Orange sands and bounding muds was planned for the deeper portions of Hole H003. Hole H002 was to be cored after Hole H003, capturing additional pressure cores to establish a dissolved methane solubility profile and to execute a second attempt at coring the Red sand with the option to core the deeper sands depending on the success of coring in Hole H003.

Drilling platform selection and contracting strategy

UT, with input from an advisory panel that included DOE, USGS, Geotek, and Pettigrew Engineering, developed vessel specification requirements, operational summaries, schedules, and well design documents that were distributed to pre-screened vessel contractors with a request for the submission of qualifications (RFQ) and expression of interest. Responses were evaluated to determine interest and verify the capabilities of proposed vessels to meet project requirements. Additional requests for information were made as needed and follow-up meetings were held to clarify project requirements.

UT performed a best-value determination pursuant to Section 51.9335 of the Texas Education Code that evaluated specific criteria such as cost, vendor reputation, quality of goods and services, extent to which a vendor met UT's needs, and past relationship with UT. The best-value determination was evaluated by UT Legal Services, UT Procurement & Payment Services, and UT Business Contracts. Based on a review of the evaluation criteria, a unanimous recommendation was made to enter contract negotiations with Helix Energy Solutions Group (Helix) to perform UT-GOM2-2 with the *Q4000* Multi-Service Vessel (*Q4000*).

UT-GOM2-2 planning and execution was simplified by contracting a US-flagged intervention vessel that routinely operates in the deepwater Gulf of Mexico. UT was able to take advantage of procedures, systems, and third-party alliance partnerships already established and provided by Helix. Most notable was the ability for UT to operate under the vessel contractor's Safety and Environmental Management System (SEMS).

Additionally, vessel-specific regulatory requirements for operating in the Gulf of Mexico OCS were already in place, therefore no additional actions were required by UT as the primary operator. These vessel-specific requirements included the USCG Certificate of Inspection, Certificate of Class, Oil Spill Response

Plan, US Certificate of Financial Responsibility, and National Pollutant Discharge Elimination System (NPDES) discharge permit.

Due to the complexities of university procurement and business contract processes, Helix agreed to subcontract and manage all third-party contractors (excluding coring) required to execute the UT-GOM2-2 operations plan as part of the master service contract with UT Austin. Subcontracted third-party services included: drilling fluids, onsite environmental compliance, cementing operations, wireline operations, gyro survey tools, drill pipe rental, professional engineer (PE) certification of well plug and abandonment designs, drilling-parameter recording system, enhanced communication system, remotely operated vehicles (ROVs), and logistical support (helicopters, crew boats, and supply boats).

During contract negotiations, the determination and acceptance of liabilities was based on a project-specific risk analysis. UT and Helix developed a mutual agreement of liability, based on project-specific factors including which aspects of the drilling activities would be controlled by which party, well control risks in the penetrated formations, and hydrate behavior. A knock-for-knock indemnification was agreed upon to the extent authorized by the constitution and laws of the State of Texas, meaning that each party was responsible for their own potential damages and losses, regardless of fault and without recourse from the other party.

UT and Helix each carried insurance to cover agreed-upon liabilities and associated financial responsibility. UT and Helix named each other as additional insureds where appropriate. UT carried the following additional insurance during project execution:

- Control of Well and Excess Downhole Equipment Coverage
- Commercial General Liability
- Maritime Employers' Liability (Jones Act)
- U.S. Longshore and Harbor Worker's Compensation Act
- Excess Liabilities
- Downhole Equipment Coverage

Regulatory obligations and compliance

In order to bid on, own, hold, or operate a lease or right of use and easement in the OCS, as defined in the Outer Continental Shelf Lands Act (43 USC 1331), a company or institution must first obtain a qualification from BOEM (30 CFR 556), after which they are recognized as a Qualified Operator. UT acquired recognition by BOEM as qualified to bid and acquire leases at a BOEM lease sale, to receive and hold leases, to be designated operator of a lease or portion of a lease, and to receive and hold pipeline rights-of-way and rights-of-use and easement on the OCS for the UT-GOM2-1 Hydrate Pressure Coring Expedition in 2017 (Flemings et al., [2018b](#)).

UT maintained its status as a Qualified Operator in the OCS, which assured that UT was able to meet the financial obligations to cover the liabilities outlined by the federal regulations (Title 30 CFR 250, 251, 550, and 551) for UT-GOM2-2. As an operator in the Gulf of Mexico, UT was required to comply with all applicable permitting and reporting requirements promulgated by state and federal regulatory agencies, including:

- United States Environmental Protection Agency (US EPA)
- United States Coast Guard (USCG)
- United States Department of Energy (DOE)
- Bureau of Ocean Energy Management (BOEM),
- Bureau of Safety and Environmental Enforcement (BSEE)
- Louisiana Department of Natural Resources (LDNR)

A summary of the permits and regulatory authorizations UT was required to obtain prior to conducting the UT-GOM2-2 offshore operations is presented in Table [T4](#). A summary of the regulatory reports and notifications that UT was required to submit throughout and subsequent to UT-GOM2-2 offshore operations is presented in Table [T5](#).

Agency	Permit / Requirement	Approved	Ref. No.	Regulatory Ref.
BOEM	Qualified Operator Certification	2017-03-21	No. 3487	30 CFR 556.35
BOEM	Leasee's or Operator's Bond (Terminated)	2021-07-19	Bond No. ROG000193	30 CFR 551.7
BOEM	Right-of-Use and Easement (RUE)	2021-11-12	OCS-G 30392	30 CFR 550.160-161
BOEM	Shallow Hazard Reports (H, G, F Locations)	2021-11-12	N-10162	NTL 2022-G01
BOEM	Exploration Plan (Initial)	2021-11-12	N-10162	NTL 2008-G04; 30 CFR 550.125-126; 550.211-235
BOEM	Right-of-Use and Easement (RUE) Amendment	2022-12-08	OCS-G 30392	30 CFR 550.160-161
BOEM	Exploration Plan (Revised)	2022-12-08	R-7211	NTL 2008-G04; 30 CFR 550.125-126; 550.211-235
BOEM	Leasee's or Operator's Bond (Replacement)	2023-07-11	Bond No. 651168	30 CFR 551.7
BOEM	Permit to Conduct Geological or Geophysical Exploration	2023-07-17	L22-025	30 CFR 551; 550.125-126
BOEM	Ads for Public Participation	2023-07-17	NA	30 CFR 551.7
BSEE	APD WR313 H002	2023-07-11	API: 608124014800	30 CFR 251.7; 250.410-418; 250.125-126
BSEE	APD WR313 H003	2023-07-11	API: 608124014900	30 CFR 251.7; 250.410-418; 250.125-126
BSEE	Burning & Welding Plan	2023-07-18	323906991	30 CFR 250.113; 250.109-113
BSEE	APM-Abandon WR313 H002	2023-08-07	API: 608124014800	30 CFR 250.465; 250.125-126, 250.1712
BSEE	APM-Abandon WR313 H003	2023-08-07	API: 608124014900	30 CFR 250.465; 250.125-126, 250.1712
DOE-NETL	NEPA Environmental Questionnaire / Categorical Exclusion	2022-03-10	NA	42 USC 4321; 43 CFR Part 46
EPA	NPDES Electronic Notice of Intent (eNOI)	2023-06-22	GMG29062W	GMG290000
LDNR	CZM Consistency Cert.	2021-11-05	C20210156	30 CFR 550.226; 251.7
USCG	Emergency Evacuation Plan	2023-05-25	ECP-23131RMS001	33 CFR 146.140
USCG	Letter of Determination (LOD)	2023-05-31	LOD-23143RMS001	33 CFR 141

Table T4: UT-GOM2-2 regulatory planning documents and permits. BOEM = U.S. Bureau of Ocean Energy Management; BSEE = U.S. Bureau of Safety and Environmental Enforcement; DOE-NETL = U.S. Department of Energy National Energy Technology Laboratory; EPA = U.S. Environmental Protection Agency; LDNR = Louisiana Department of Natural Resources; USCG = U.S. Coast Guard; APM = Application for Permit to Modify; APD = Application for Permit to Drill; NEPA = U.S. National Environmental Policy Act; NPDES = U.S. National Discharge Elimination System; CZM = U.S. Coastal Zone Management; WR313 = Walker Ridge Block 313

Agency	Well	Permit / Notice /Requirement	Submitted	Form	Regulatory Ref.
BOEM	All	Notice of Commencement of Operations	2023-08-02	Email Notice	Permit L22-025 COA
BOEM	All	Notice of Completion of Operations	2023-09-02	Email Notice	Permit L22-025 COA
BOEM	All	Final Report	2023-09-28	None/Courier	Permit L22-025 COA
BSEE	H002	APM - Plug and Abandon H002	2023-07-18	BSEE-0124	§ 250.1712
BSEE	H003	APM - Plug and Abandon H003	2023-07-26	BSEE-0124	§ 250.1712
BSEE	H003	Notice of Rig Movement	2023-07-28	BSEE-0144	§ 250.712
BSEE	H003	Determine Final Surface Location	2023-08-11	BSEE-0124	§ 250.465
BSEE	H002	Determine Final Surface Location	2023-08-11	BSEE-0124	§ 250.465
BSEE	H003	WAR, Open Hole Data Report (8/02 - 8/05)	2023-08-11	BSEE 0133, BSEE 0133S	§ 250.742, § 250.743
BSEE	H003	APM Rev. - Request to Spot Mud H003	2023-08-15	BSEE-0124	§ 250.465, § 250.701
BSEE	All	Notice of Rig Movement	2023-08-16	BSEE-0144	§ 250.712
BSEE	H003	WAR, Open Hole Data Report (8/06 - 8/12)	2023-08-18	BSEE 0133, BSEE 0133S	§ 250.742, § 250.743
BSEE	H003	WAR, Open Hole Data Report (8/13 - 8/16)	2023-08-19	BSEE 0133, BSEE 0133S	§ 250.742, § 250.743
BSEE	H002	WAR, Open Hole Data Report (8/16 - 8/19)	2023-08-25	BSEE 0133, BSEE 0133S	§ 250.742, § 250.743
BSEE	H002	Notice of Rig Movement	2023-08-31	BSEE-0144	§ 250.712
BSEE	H002	WAR, Open Hole Data Report (8/20 - 8/26)	2023-09-01	BSEE 0133, BSEE 0133S	§ 250.742, § 250.743
BSEE	H002	WAR, Open Hole Data Report (8/27 - 8/31)	2023-09-08	BSEE 0133, BSEE 0133S	§ 250.742, § 250.743
BSEE	H003	End of Operations Report	2023-09-15	BSEE-0125	§ 250.744
BSEE	H003	Site Clearance Report	2023-09-15	BSEE-0124	§ 250.1740, § 250.1742, § 250.1743
BSEE	H002	Site Clearance Report	2023-09-15	BSEE-0124	§ 250.1740, § 250.1742, § 250.1743
BSEE	H002	End of Operations Report	2023-09-27	BSEE-0125	§ 250.744
BSEE	All	Final Well Logs	2023-10-04	None / Courier	NTL 2016 N07, NTL 2009-N10
EPA	All	Quarter 2 DMR	2023-08-25	NetDMR	GMG290000
EPA	All	Notice of Termination	2023-09-27	NetDMR	GMG290000
EPA	All	Quarter 3 DMR	2023-09-27	NetDMR	GMG290000

Table T5: UT-GOM2-2 regulatory reports and notifications. BOEM = U.S. Bureau of Ocean Energy Management; BSEE = U.S. Bureau of Safety and Environmental Enforcement; EPA = U.S. Environmental Protection Agency



Laboratories from Geotek Coring Inc. are placed on deck. Each lab was supplied with safety monitors, power, water, and air before being set up to receive core. Photo credit: Geotek Ltd.

Execution

UT-GOM2-2 occurred in seven execution phases: (1) Preparation; (2) Mobilization; (3) Onboard Operations; (4) Demobilization; (5) Remobilization for Shore-Based Science at the ‘dockside’ location in Salt Lake City, Utah; (6) Execution of Dockside Operations; and (7) Demobilization from Salt Lake City (Table [T6](#)).

Preparation and mobilization to the port

Extensive planning for core acquisition, core analysis, and sample transport was conducted during the preparation phase. Invitations were sent out to members of the science team and a first pass look at sample and data requests from the members of the greater hydrate community was used in the identification and gathering of supplies to support the science goals. The *Operational Plan* (Flemings et al., [2023b](#)) and *Scientific Prospectus* (Flemings et al., [2023a](#)) were published.

All regulatory obligations were met, permits and equipment certifications were secured, and equipment and supplies were acquired and packed.

T-HUET and UT-GOM2-2 Science Meeting were conducted in Houston, Texas and a Drill-Well-on-Paper (DWOP) workshop was conducted with Helix and others in Austin, Texas.

University personnel visited the Helix Q4000 in dry dock in Pascagoula, Mississippi on two occasions to discuss mobilization needs with Helix. The Helix Q4000 departed from Pascagoula, Mississippi and transitioned directly to the offshore Walker Ridge Block 313 Project Site H.

Phase	Summary	Start	End
1. Preparation & mobilization to the port	<ul style="list-style-type: none"> • Complete regulatory obligations, permitting, certifications, equipment & supply packing • T-HUET training and UT-GOM2-2 Science Meeting, Houston, TX • Drill-Well-on-Paper (DWOP) workshop with Helix & others, Austin, TX • Finalize & publish Operations Plan & Prospectus: Science & Sample Distribution Plan • Visit Helix <i>Q4000</i> in dry dock, Pascagoula, MS • Helix <i>Q4000</i> transit from Pascagoula, MS directly to the offshore WR313 project site • Land mobilization of tools, equipment, & supplies to Harvey Gulf port, Port Fourchon, LA • Tools, equipment, & supplies loaded onto the <i>Harvey Hermes</i> supply vessel • Personnel mobilized to Houma, LA heliport 	1 January 2023	30 July 2023
2. Mobilization	<ul style="list-style-type: none"> • Helix <i>Q4000</i> goes on contract 40 miles from WR313 project site • Helicopter flights commence from Houma, LA • <i>Harvey Hermes</i> departs from Port Fourchon, LA • Helix <i>Q4000</i> and <i>Harvey Hermes</i> rendezvous at the WR313 project site • Load equipment from supply vessel <i>Harvey Hermes</i> to Helix <i>Q4000</i>; Pressure testing; ROV survey; T2P & PCTB test; trip to seafloor 	30 July 2023	3 August 2023
3. Onboard Operations	<ul style="list-style-type: none"> • Drill/core Hole H003 with G-APC, G-XCB, & PCTB-CS to 7505 ft RKB • Abandon Hole H003 with heavy mud • Drill/core Hole H002 with PCTB-FB & PCTB-CS to 9332 ft RKB • Abandon Hole H002 with cement & heavy mud • Image, log, & cut pressure cores • Image & cut conventional cores, measure sediment strength • Collect, analyze, & store void gas samples • Sub-core microbiology whole rounds, squeeze pore water whole rounds, & sub-divide pore water & cakes 	4 August 2023	30 August 2023
4. Demobilization	<ul style="list-style-type: none"> • Personnel & equipment disembark from Helix <i>Q4000</i> on helicopters or supply boats • Helix <i>Q4000</i> goes off contract 	30 August 2023	1 September 2023
5. Dockside Remobilization	<ul style="list-style-type: none"> • Transport pressure cores to UT Austin or Geotek HQ, Salt Lake City, UT • Transport conventional/conventionalized cores to College Station, TX for MSCL & CT • Transport conventional/conventionalized cores from College Station, TX to Geotek HQ in Salt Lake City, UT • Set up laboratories; mobilize science party in Salt Lake City, UT 	4 September 2023	18 September 2023
6. Dockside Operations	<ul style="list-style-type: none"> • Intensive analysis of cores in Salt Lake City, UT • Quantitative degassing of pressure core sections • Split, image, log, describe, characterize, & sample conventionalized cores • Squeeze depressurized whole rounds for pore water • Cryogenically freeze, depressurize, & sample pressure cores for microbiological analysis 	19 September 2023	26 September 2023
7. Dockside Demobilization	<ul style="list-style-type: none"> • Decommission laboratories, demobilize science party • Ship conventional cores & sediment samples to UT Austin • Ship samples to laboratories for additional analysis 	27 September 2023	28 September 2023

Table T6: Execution phases of UT-GOM2-2 performed in 2023. T-HUET= Tropical Helicopter Underwater Escape Training; WR313 = Walker Ridge Block 313; ROV = remote-operated vehicle; PCTB = Pressure Coring Tool with Ball Valve; APC = Advanced Piston Corer; XCB = eXtended Core Barrel; PCTB-CS = Pressure Coring Tool with Ball Valve in the Cutting Shoe Configuration; PCTB-FB = Pressure Coring Tool with Ball Valve in the Face Bit Configuration; T2P = Temperature 2 Pressure Probe; MSCL= Multi-Sensor Core Logger; CT = Computed Tomography; RKB = rotary kelly bushing or rig floor when no bushing is present; UT Austin = The University of Texas at Austin; Geotek HQ = Geotek Headquarters

The UT-GOM2-2 port of embarkation was Harvey Gulf, in Port Fourchon, Louisiana. Mobilization of all Helix and Helix third-party equipment, supplies, and fluids to Harvey Gulf was managed and performed by Helix. Helix also managed the mobilization of drill collars from the UT Pickle Research Campus in Austin, Texas to Harvey Gulf. Mobilization of University and Geotek equipment and supplies to Harvey Gulf was managed and performed by UT and Geotek. Mobilization of rented equipment from Pro-Log Inc. and Trinity Rentals to Harvey Gulf was managed by UT.

Geotek containers arrived at Harvey Gulf several days early to allow time to setup and test equipment and set up mobile laboratories prior to loading onto the supply vessel, the *Harvey Hermes*. Twelve service vans/containers and two baskets of heavy equipment were delivered to Harvey Gulf and loaded onto the *Harvey Hermes*. Drilling fluids, water, and fuel were also loaded onto the *Harvey Hermes*. Heavy pipe and drill collars were loaded onto the *Harvey Hermes* in baskets and slings. The *Harvey Hermes* departed from Harvey Gulf to rendezvous with the Helix Q4000 at the drill site.

Personnel arrived in Port Fourchon and Houma, Louisiana.

Mobilization on the rig

The Helix Q4000 officially went on contract with UT when it was within 40 miles of the drill site. The Helix Q4000 arrived at the drill site on 30 July 2023. The *Harvey Hermes* also arrived on site on 30 July 2023 and began transferring tools, equipment, supplies, and fluids to the Helix Q4000. Geotek brought the service vans online, and connected them to external air, water, and power sources. Mobilization of personnel occurred in stages, with some being transferred on the *Harvey Hermes* and others by helicopter transport from Houma, Louisiana over several days. All helicopter transports were managed by Helix.

The Helix Q4000 was moved over the planned position of Hole H003 while conducting dynamic positioning (DP) surveys for the vessel. The PCTB bottom-hole

assembly (BHA) and drill pipe were run into the ocean and Helix Q4000 work-class ROVs (XLS09 and XLS10) were deployed to conduct a systematic search for the seafloor location of the Hole H001 borehole head. The seafloor search for Hole H001 was unsuccessful and the decision was made to mark the seafloor locations of the proposed UT-GOM2-2 boreholes with ROV deployed buoys based on the coordinates for the holes within the expedition prospectus (Flemings et al., [2023a](#)).

Geotek made up the BHA and tested the PCTB within the water column before spudding Hole H003. A test of the Temperature 2 Pressure probe (T2P) was performed but was unsuccessful.

Onboard operations

UT-GOM2-2 was executed from 0000 hours on 04 August 2023 to 2400 hours on 30 August 2023. A description of operations, surface locations, water depth, rig-floor height, deviation, drilling fluids program, and plug and abandonment program are described in [Drilling Operations](#).

Demobilization from the rig

Demobilization from the UT-GOM2-2 Terrebonne Basin test site at WR313 began on 31 August 2023. The UT-GOM2-2 port of debarkation was Harvey Gulf, in Port Fourchon, Louisiana. All university, Geotek, and rented equipment was transferred from the Helix Q4000 to the *Harvey Hermes* and/or *Harvey Spirit* for transport to Harvey Gulf. Some university and science party personnel demobilized from the Helix Q4000 by helicopter. All Geotek crew and remaining shipboard scientists departed the Helix Q4000 on the *Harvey Hermes*, which departed the Helix Q4000 (onsite at WR313) at 1500 hours on 31 August 2023.

After completing the transfer of equipment and personnel, the Helix Q4000 moved 1 mile off location by 2400 hours on 01 September 2023, and the Helix Q4000 went off contract. On 01 September 2023, the Geotek staff offloaded containers and other equipment from the *Harvey Hermes* at the Harvey Gulf Port. Three containers with cores and samples were

provided with electrical power on the *Harvey Hermes* and at the port.

Microbiology, biostratigraphic, pore water, and gas samples were hand delivered to waiting scientists and/or shipped from Port Fourchon, Louisiana to the appropriate labs.

Remobilization in Salt Lake City

Rented cargo baskets were picked up by Trinity Rentals at Harvey Gulf Port. Geotek shipped eight service vans/containers including laboratories with samples and the PCTB heavy van with pressure core equipment and tubulars from Harvey Gulf to Geotek facilities in Salt Lake City, Utah. Conventional cores were transported by Geotek to College Station, Texas for conventional core logging (Geotek Multi-Sensor Core Logger [MSCL] and computed tomography [CT]). Harvey Gulf was vacated by the UT-GOM2-2 science party and subcontractors on 08 September 2023.

Thirteen pressure cores were delivered to the UT Pressure Core Center on 09 September 2023. The remaining pressure core sections were transported to Geotek facilities in Salt Lake City, Utah for further processing. All whole-core logging and CT imaging was completed in College Station, Texas on 12 September 2023. Conventional and conventionalized cores were transported from College Station, Texas to Geotek facilities, arriving on 15 September 2023. Geotek continued to establish the facilities and laboratory spaces in Salt Lake City, Utah through 18 September 2023.

Salt Lake City operations

Scientists and associated technical staff arrived at Geotek Salt Lake City facilities on 18 September 2023 and began setting up laboratories. Microscopes, sampling supplies, tables, and computers were set up in the Split Core Lab. Scientists started sub-sampling discrete paleomagnetic samples from the residual sediments left after pore water squeezing on the vessel. CT images of cores from Hole H003 were reviewed and the whole-round core sampling program in support of the geomechanical testing

effort was prepared for Cores H003-01H through H003-10H.

Core analysis and processing at the Geotek Salt Lake City facilities started on 19 September 2023. Core sections were weighed and whole round core samples were cut for index properties, including moisture and density analysis (MAD), grain size studies by laser particle analysis and hydrometer methods, x-ray powder diffraction (XRPD), and other basic properties). Additionally, geomechanics (plus permeability, porosity, and other physical properties), undrained strength measurements (one per section), and thermal conductivity measurements (at least one per core) were made.

Conventional and conventionalized core sections were split, imaged (including color spectrophotometry), laid out in the Split Core lab, and described. Smear slides were produced and examined. Working halves of cores were sampled for a range of additional measurements (e.g., total organic carbon (TOC), total carbon (TC), hydrogen, nitrogen, and sulfur (CHNS), isotopes, grain size, moisture and density, XRPD, x-ray fluorescence (XRF), rock magnetism, magnetic susceptibility, paleontology, and biogenic silica). No authigenic carbonates or sulfide nodules were encountered. Archival halves of sections were logged, measuring magnetic susceptibility and XRF.

Geotek used a loop magnetic susceptibility sensor for scanning whole round conventionalized pressure core, which was not conducted with the MSCL-S scans of conventional core at College Station, Texas.

Several whole rounds were squeezed, and the resulting water samples were measured for salinity and alkalinity; and stabilized for shipping to post-expedition labs.

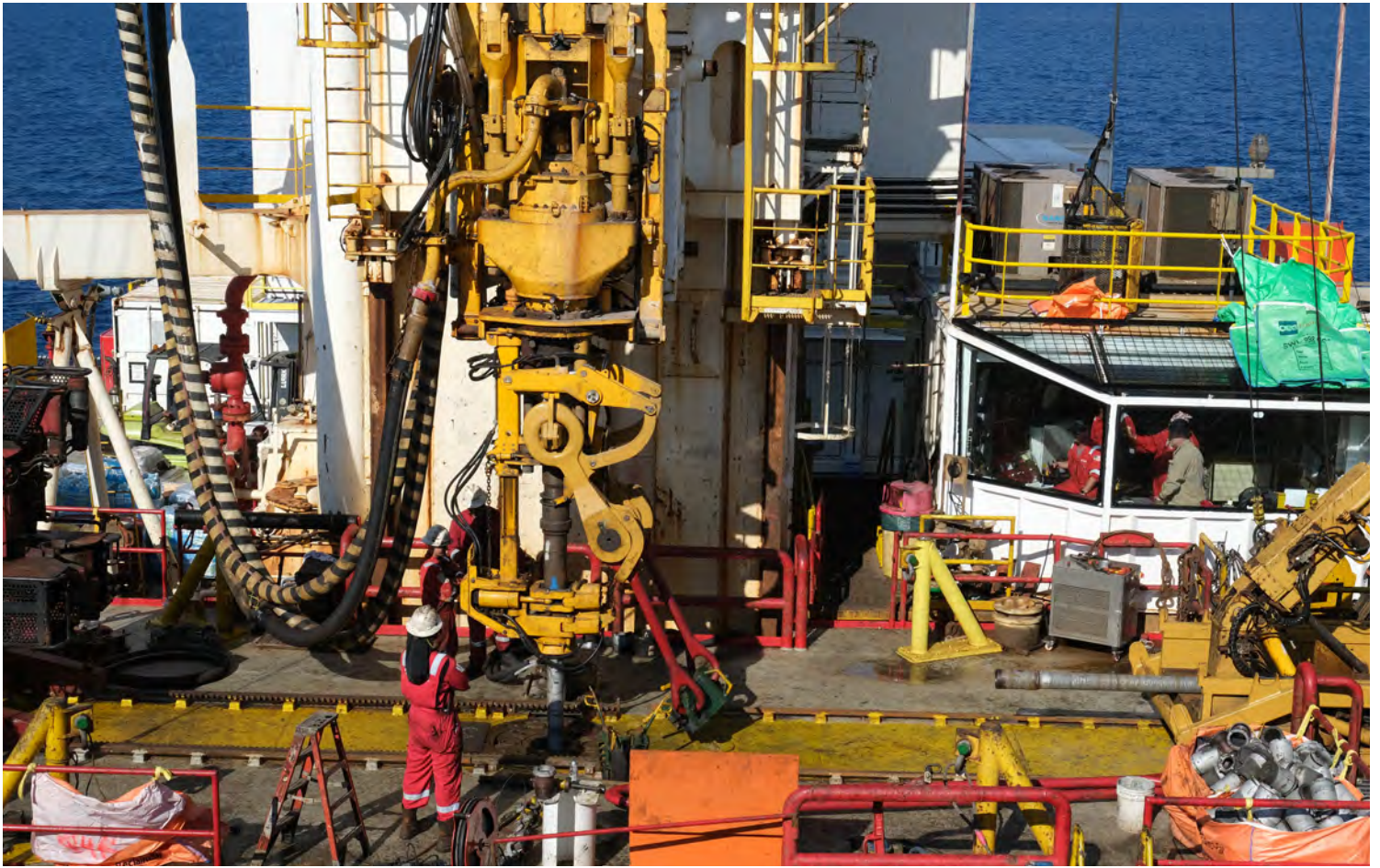
Pressure core sections were quantitatively degassed or cryogenically frozen and rapidly depressurized. Microbiological samples were also acquired by sub-coring these cryo-frozen cores and those that had been cryo-frozen onboard. Sub-core samples were divided for cell count analysis at the Japan Agency

for Marine-Earth Science and Technology (JAMSTEC) and DNA extraction at Oregon State University. The remaining rinds of cryo-cores were also split and described in Salt Lake City. Gas hydrate samples and associated gas samples were also acquired while sub-coring and splitting the last cryo-core.

All science operations at the Geotek Salt Lake City facilities were completed on 26 September 2023 and a first-round draft of the Methods section for the expedition report was completed and submitted for review.

Demobilization from Salt Lake City

The science team packed up samples and supplies on 27 September through 28 September 2023. Thirty-one individual containers of samples were shipped to eight laboratories. Equipment and supplies were consolidated into six pallets and shipped on 28 September 2023 to four laboratories. Geotek continued logging split cores during and after this time. All split cores were delivered to UT on 15 December 2023.



Helix engineers prepare to disconnect drill pipe from the Helix Q4000 top drive to insert another pipe section.
Photo credit: Peter B. Flemings

Drilling operations

Operational summary

A summary of the operations is provided in Table [T7](#) and a graphical presentation of all operations at Site H is shown in Figure [F14](#).

Surface locations

The surface locations of Hole H002 and Hole H003 are shown in Table [T8](#) and Figure [F15](#) as surveyed by Fugro U.S.A. Marine Inc (Fugro). Fugro provided its own positioning system and precisely located the vessel's position over the proposed borehole locations. The ROV was then maneuvered directly beneath the vessel using the Helix Q4000 navigation system. Buoys were then placed at the borehole locations. Before each borehole was spudded, the respective buoys were moved to allow the BHA to spud the borehole at the precise location of the buoy.

Water depth and rig floor elevation

In Hole H003, the coring bit touched the seafloor mud line at a depth of 6,506 ft RKB on 04 August 2023 (Table [T8](#)). The rig floor elevation above sea level was 52 ft, and therefore the water depth was 6,454 ft. In Hole H002, the bit also touched the seafloor mud line at a depth of 6,506 ft RKB on 17 August 2023. The rig floor elevation

Dates	Summary
04 August 23	Hole H003 was spudded with three successive G-APC hydraulic position cores (Cores H003-01H, -2H, and -3H). Undrained strength was monitored along each G-APC core as it was sectioned to aid in the G-APC to G-XCB transition.
05 August 23	The first pressure coring operations were completed (Cores H003-04CS and -05CS) and the borehole was then advanced to a total depth of 6659 ft RKB (46.6 mbsf) with the acquisition of two G-APC hydraulic position cores (H003-06H and -07H).
06 to 07 August 23	While preparing for the deployment of the coring tool, the wireline separated under tension (See Drilling Challenges). The BHA was pulled to the mudline and the wireline recovered to the rig floor. Hole H003 was re-entered and Cores H003-08CS, -09H, and -10H were acquired.
08 to 10 August 23	Cores H003-11CS to -25H were recovered.
10 to 13 August 23	The Top Drive System (TDS) blower motor failed and was removed. The replacement blower motor was delivered to the Helix Q4000 and installed in the TDS.
14 to 15 August 23	The first and only G-XCB core (Core H003-26X) was acquired followed by three pressure cores (Cores H003-27CS to -29CS).
15 to 16 August 23	Because the borehole was inclined (See Borehole Deviation Survey) the decision was made to terminate operations in Hole H003. Hole H003 was abandoned, marking the end of Hole H003 and the start of Hole H002.
17 to 18 August 23	Hole H002 was spudded with the Pressure Coring Tool with Ball Valve in the Face Bit Configuration (PCTB-FB). Three directional surveys were conducted in the shallow section of Hole H002, and the hole remained near vertical (See Borehole Deviation Survey).
19 to 21 August 23	Operations included drilling Hole H002 to a total depth of 8620 ft RKB (644.3 mbsf) and acquiring Cores H002-01FB to -03FB.
21 to 22 August 23	After cutting Core H002-04FB, the PCTB-FB became stuck in the BHA. The PCTB-FB coring BHA was pulled to the rig floor and the Pressure Coring Tool with Ball Valve in the Cutting Shoe Configuration (PCTB-CS) BHA was used to re-enter and advance the borehole to a depth of 9131 ft RKB (800.0 mbsf) (See Drilling Challenges).
23 to 27 August 23	Hole H002 was pressure cored from a depth of 9131 to 9221 ft RKB (800.0 to 827.5 mbsf), to complete the Orange sand pressure coring campaign (Cores H002-05CS to -13CS). The borehole was advanced and Cores H003-14CS and -15CS were acquired without pressure ending the Hole H002 coring campaign.
27 to 28 August 23	In preparation for cementing, the Geotek cementing liner became stuck in the BHA, the Helix Q4000 lost the ability to circulate drilling fluids through the BHA, and the BHA was pulled back to the rig floor. The BHA was run into the borehole without problems and the borehole was plugged and abandoned (See Drilling Challenges).

Table T7: High-level operational summary. G-APC = Geotek Advanced Piston Corer; G-XCB = Geotek eXtended Core Barrel; BHA = bottom-hole assembly; RKB = rotary kelly bushing or rig floor when no bushing is present

above sea level was 52 ft. Thus, the Hole H002 water depth was 6,454 ft.

Borehole deviation survey

One deviation survey was conducted in Hole H003 after the borehole was advanced to a depth of 7,505 ft RKB (Table T9). The survey was conducted from inside the drill pipe, above the BHA. One measurement was made near the mudline (6,600 ft RKB) and one near the BHA (7,451 ft RKB).

The borehole was found to trend ESE with inclination increasing from 6.06 degrees near the mudline to

7.75 degrees near the bottom of the borehole. The significant deviation of the borehole drove the decision to terminate drilling operations in Hole H003 and permanently abandon the borehole.

Four deviation surveys were conducted in Hole H002 throughout the drilling and coring of the borehole (Table T9). The surveys were conducted from inside the drill pipe above the BHA. Deviation was consistently less than 1 degree.

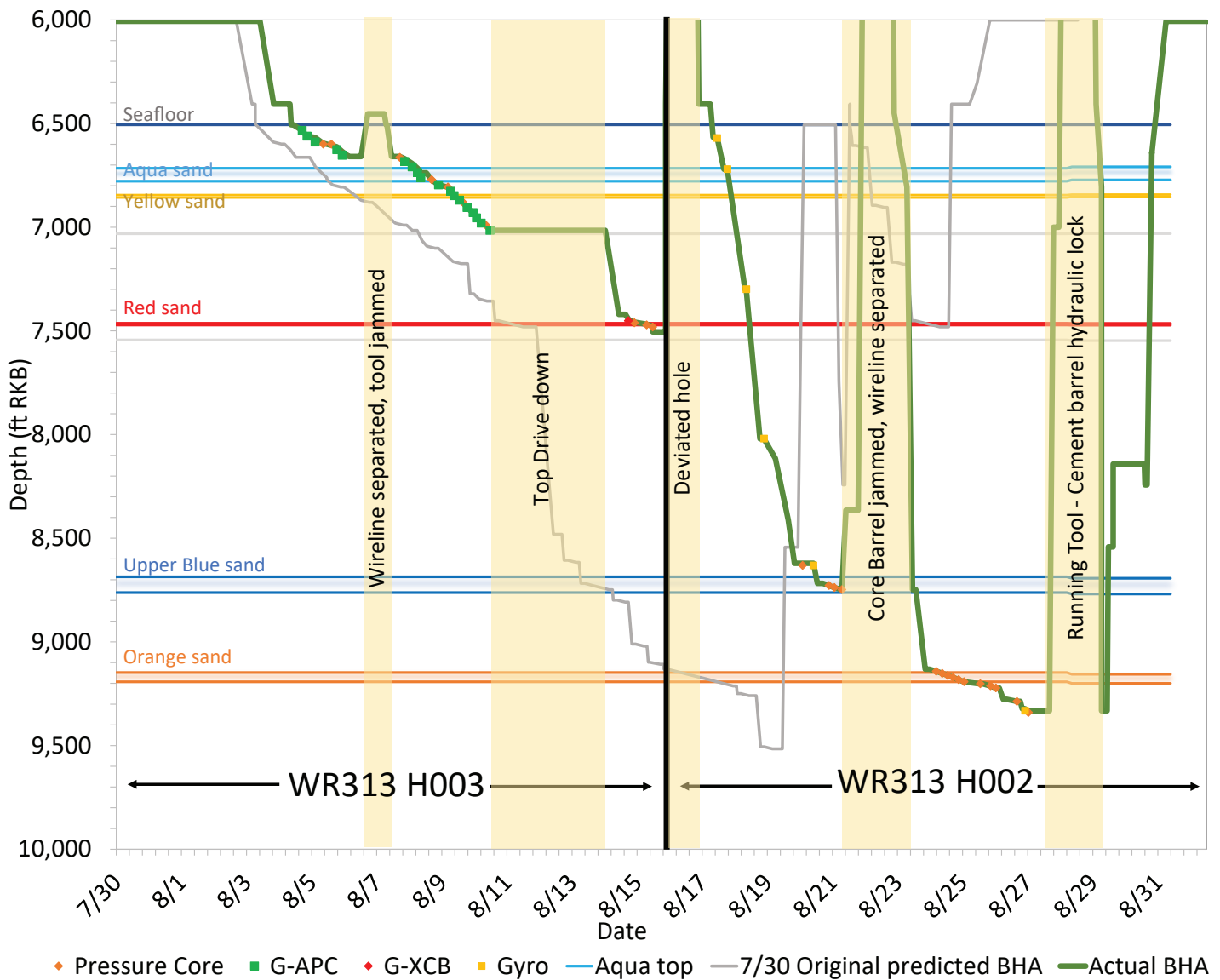


Figure F14: Bit depth as a function of time at Walker Ridge Block 313 (WR313) for Hole H002 and Hole H003. The original operational plan (Figure F13) is shown as a light gray line. The recorded bit depth is shown as a green line. On top of the green line, stops are shown for pressure coring as orange dots, conventional coring as green squares and red diamonds, and gyroscopic measurements as dark yellow squares. Operational downtime is shown as transparent yellow columns. Sands described in Table T10 are shown as aqua blue, yellow, red, blue, and orange horizontal lines.

Correlation of Hole H001 log data to Site H core data

Correlations of Hole H001 LWD log data to Hole H003 core data

The coring program assumed Hole H003 would be vertical and along geologic strike from Hole H001. Thus, the coring plan assumed strata at a given depth below the seafloor in Hole H001 would be at the same depth in Hole H003. However, while Hole H001 is nearly vertical, Hole H003 is significantly deviated (Table T9).

We correlated core measurements in H003 to LWD measurements in H001 and found that equivalent seismic horizons and stratigraphic surfaces in Hole H003 could be correlated to H001:

$$MD_{H003_{BSF}} = C * MD_{H001_{BSF}} + B$$

Equation E3

Equation E3 correlates the measured depth below seafloor in the H001 well ($MD_{H001_{BSF}}$) to the measured depth below seafloor in the H003 well ($MD_{H003_{BSF}}$). C was constrained to be 0.988 and B to be 10.9 ft (3.32 m). This estimate may be refined in the future by

Borehole	API Number	Top-Hole Location		Bottom-Hole Location		Top-Hole Depth		
		Latitude	Longitude	Latitude	Longitude	Pipe Length to Seafloor	Sea Surface	Water depth
		(NAD27)	(NAD27)	(NAD27)	(NAD27)	(ft RKB)	(ft RKB)	(ft)
WR313 H001	608124004000	26° 39' 44.85"	-91° 40' 33.75"	26° 39' 44.99"	-91° 40' 33.17"	6502	51	6451
WR313 H002	608124014800	26° 39' 44.22"	-91° 40' 33.90"	26° 39' 44.18"	-91° 40' 33.63"	6506	52	6454
WR313 H003	608124014900	26° 39' 45.45"	-91° 40' 33.59"	26° 39' 44.84"	-91° 40' 32.61"	6506	52	6454

Table T8: Final surface and bottom-hole locations and water depth at the time of drilling for Walker Ridge Block 313 (WR313) Hole H001, Hole H002, and Hole H003. Hole H001 was drilled during the 2009 Gas Hydrates Joint Industry Project Leg II (JIP II) logging while drilling (LWD) program; Hole H002 and Hole H003 were drilled during this 2023 UT-GOM2-2 Hydrates Coring Program. Hole H002 and Hole H003 top-hole locations are as surveyed by Fugro on 02 August 2023. The bottom hole locations were determined by combining these surface locations with the offset data from Gyrodata, as surveyed on 14 August 2023 and 26 August 2023, respectively (Table T9). Hole H001 top-hole and bottom-hole locations are from BSEE, 2024.

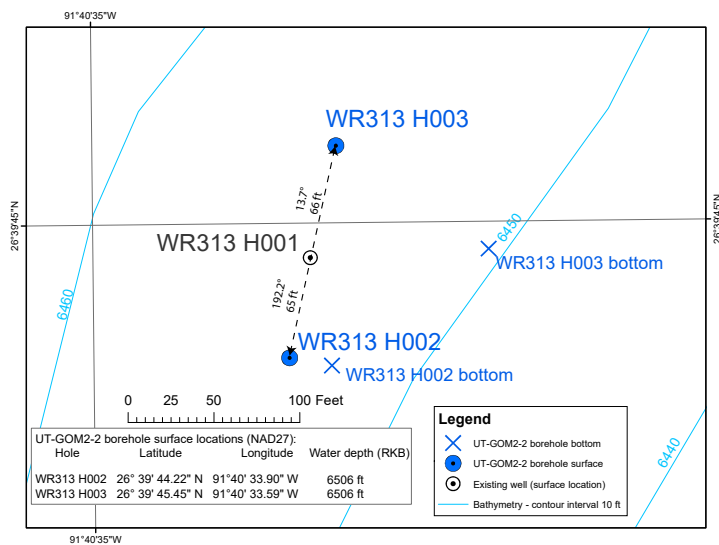


Figure F15: The locations, distances, and azimuths of the boreholes at Site H. Hole H001 location coordinates from BSEE, 2024. The locations of Hole H002 and Hole H003 as surveyed by Fugro (top-hole) and Gyrodata (bottom-hole) during UT-GOM2-2 (Table T8). Bathymetry derived from seafloor reflector in 3D seismic data. BSEE = U.S. Bureau of Safety and Environmental Enforcement; WR313 = Walker Ridge Block 313; NAD27 = North America Datum of 1927; 3D = three-dimensional

comparing measured properties of the recovered cores in Hole H003 against Hole H001 LWD measured properties. Figure F16 shows comparisons of the measured Hole H003 core densities and porosities to Hole H001 LWD derived densities and porosities.

Correlation of Hole H001 LWD log data to Hole H002 core data

The H002 coring program was based on the LWD-interpreted stratigraphy of Hole H001. Both Hole H002

and Hole H001 are essentially vertical. Furthermore, they were located along strike with each other with the intention that stratigraphic surfaces would be at the same depth in the two boreholes. Thus, stratigraphic surfaces in Holes H001 and H002 are assumed to exist at equivalent depths below seafloor.

Plotting H001, H002, and H003 down-hole data

When Hole H001 LWD and tops data are plotted with H002 and H003 downhole data, all depths to 300 mbsf in Hole H001 are first converted to Hole H003 depths using Equation E3. The depth conversion is only applied down to 300 mbsf because only Hole H003 was deviated and Hole H003 was only cored to 7,470 ft RKB (296.9 mbsf). Using this method, the resulting correlated depths of seismic horizon and stratigraphic surfaces were calculated and is shown in Table T10.

Drilling challenges

Tools became stuck inside the BHA three times. As a result, the BHA had to be either partially (06 August 2023) or completely (21 August 2023 and 27 August 2023) retrieved to the rig floor (Figure F14 and Table T11). In the first two cases, the PCTB could not be removed from the BHA. In the last case, the cement liner could not be removed. In all three cases, it was determined that the tool became stuck because coarse-grained sediment packed off around the tool within the BHA.

Borehole	Measured Depth (ft RKB)	Inclination (deg.)	Azimuth (deg.)	Dogleg Severity (deg./100 ft)	Vertical Depth (ft RKB)	Closure		Horizontal Coordinates	
						Dist. (ft)	Az. (deg.)	Y (ft)	X (ft)
WR313 H003	6600	6.06	123.32	6.45	6599.82	4.97	123.32	-2.73	4.15
	7451	7.75	124.38	0.2	7444.63	107.23	123.89	-59.79	89.02
WR313 H002	6667	0.82	110.19	0.51	6666.99	1.15	110.19	-0.4	1.08
	7667	0.35	96.79	0.05	7666.94	11.31	106.57	-3.23	10.84
	8577	0.6	99.24	0.03	8576.91	18.83	103.27	-4.32	18.32
	9268	0.47	78.33	0.03	9267.88	25.04	99.95	-4.33	24.67

Table T9: Hole H003 and Hole H002 borehole deviation surveys performed at Walker Ridge Block 313 (WR313) by Gyrodata. The gyroscopic surveys were taken inside the 9-7/8” drill pipe. All measured depths and coordinates are referenced to the Helix Q4000 rig floor (RKB) height of 6,506 ft above seafloor. All calculations assume the drill pipe is vertical (0-degree inclination) from the RKB to the seafloor (6,506 ft).

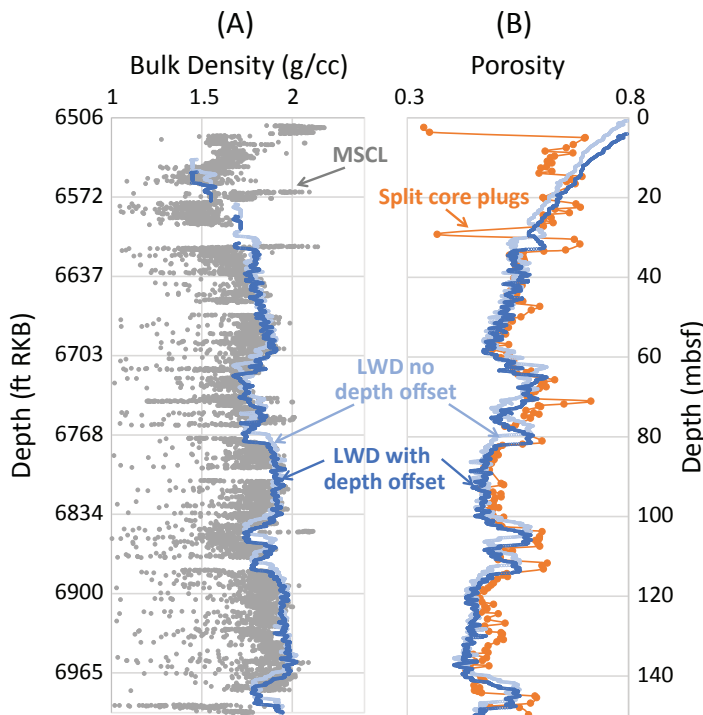


Figure F16 (left): Demonstration of correlation between Hole H001 and Hole H003 using Equation E3. A) Gray dots: Hole H003 core whole-round bulk density measurements acquired using the Geotek Multi-Sensor Core Logger (MSCL) plotted in Hole H003 compressed depth (See [Plotting core data as a function of depth](#)). Light Blue line: H001 logging while drilling (LWD) bulk density plotted as a function of Hole H001 depth. [Site H seismic and LWD interpretation](#) describes how porosity was calculated. Dark Blue line: H001 LWD bulk density projected to H003 depths using Equation E3 (B =3.2. m, C = 0.988). B) Orange circles: Hole H003 porosity from moisture and density measurements. Core porosity was calculated assuming a grain density of 2.70 g/cm³, a typical value for muds. Core porosity is not corrected for salinity. H001 LWD bulk density plotted as a function of Hole H001 depth. Dark Blue line: H001 LWD Bulk density projected to H003 depths using Equation E3 (B =3.2. m, C = 0.988). The peaks in the darker blue line correlate more closely to the peaks in the porosity data (orange line).

It is possible that part of the drilling challenge was caused by shallow sand encountered at the top of the borehole (Figure F17). During drilling, this shallow sand continued to fall into the borehole. The first core taken in Hole H003 recovered 4.5 meters described as very fine and fine sand with some silt (Figure F18). A sample from Section H003-01H-3a was measured using laser particle analysis as fine- to very fine-grained (Figure F19). These sands are coarser than the sands we sampled in the Orange sand (Figure

F19). Core CT images indicated that Sections 1 and 2 of Core H003-01H were about half-full of sediment before splitting and the rest of the core liner was full of water. Thus, the actual thickness of this seafloor sand may be thicker than the recovered amount.

During drilling, a crater developed around each borehole at the seafloor as near-surface sand slumped into the borehole. There was a large amount of fall-in throughout drilling of both Hole H003 and Hole H002. It is possible that the sand that had fallen into each

			WR313 H001		WR313 H002		WR313 H003			
Events, Sands & LWD Units			Depth (mbsf)	Depth (ft RKB)	Depth (mbsf)	Depth (ft RKB)	Depth (mbsf)	Depth (ft RKB)		
Seafloor			-	6,513	-	6,506	-	6,506		
Hzr 1200			61	6,715	61	6,708	64	6,716		
Water-bearing Aqua sand	Top	LWD Unit 1	61	6,715	61	6,708	64	6,716		
	Base		80	6,777	80	6,770	83	6,778		
Hzr 1100			101	6,846	101	6,839	104	6,846		
Water-bearing Yellow sand	Top		101	6,846	101	6,839	104	6,846		
	Base		105	6,857	105	6,850	107	6,857		
Hzr 1000			158	7,033	158	7,026	160	7,031		
JIP mud unit with low concentration hydrate	Top		LWD Unit 2	158	7,033	158	7,026	160	7,031	
Hzr 0900				292	7,471	292	7,464	292	7,463	
Hydrate-bearing Red sand	Top			292	7,471	292	7,464	292	7,463	
	Base			294	7,479	294	7,472	294	7,471	
JIP mud unit with low concentration hydrate	Base	316	7,551	316	7,544					
Hzr 0800			316	7,551	316	7,544				
Water-bearing coarse-grained interval	Top	LWD Unit 3	334	7,609	334	7,602				
	Base		335	7,613	335	7,606				
Hydrate-bearing marine mud	Top		523	8,229	523	8,222				
	Base		525	8,235	525	8,228				
Hydrate-bearing marine mud	Top		558	8,345	558	8,338				
	Base		563	8,359	563	8,352				
Hzr 0500			610	8,513	610	8,506				
Water-bearing coarse-grained interval	Top	LWD Unit 4	615	8,530	615	8,523				
	Base		622	8,555	622	8,548				
Hydrate-bearing Upper Blue sand	Top		664	8,693	664	8,686				
	Base		688	8,769	688	8,762				
Hzr 400			696	8,798	696	8,791				
Hydrate-bearing marine mud	Top	LWD Unit 5	786	9,091	786	9,084				
	Base		786	9,093	786	9,086				
Hzr 0300			805	9,155	805	9,148				
Hydrate-bearing Orange sand	Top		805	9,155	805	9,148				
	Base		819	9,199	819	9,192				
Interpolated BSR			895	9,448	895	9,441				

Table T10: Correlated seismic horizons and stratigraphic surfaces in Holes H001, H002, and H003. LWD = logging while drilling; JIP = 2009 Gas Hydrates Joint Industry Project Leg II; Hzr = horizon

borehole may have contributed to the inability of the prescribed drilling/coring fluids handling program and prescribed borehole sweeps to successfully clean each borehole. In turn, this may have contributed to the repeated pack-offs of the BHA in Hole H002 and Hole H003.

Plug and abandonment

The Plug and Abandonment Plans for Holes H003 and H002 were reviewed and certified by a professional engineer and were subsequently reviewed and approved by BSEE. Any deviation from the BSEE-

Date	Summary
6 August 2023	While preparing for the deployment of the coring tool for core H003-08CS, the wireline separated under tension while deploying the PCTB-CS pulling tool before coring. After recovering the PCTB-CS pulling tool from the borehole, the Geotek emergency pulling tool was run into the borehole and successfully latched to the PCTB-CS core barrel. However, the PCTB-CS could not be removed from the BHA, and it was interpreted that the PCTB-CS was packed-off in the BHA with mud/sand. The BHA was pulled out of the borehole. However, after the BHA cleared the seafloor, the mud/sand had cleared, and the PTCB-CS core barrel was no longer stuck.
21 August 2023	After deploying the PCTB-FB tool and cutting Core H002-04FB, multiple attempts were made to unlatch the PCTB-FB tool. The wireline separated under tension, and it was decided that the PCTB-FB inner barrel was stuck and could not be removed from the BHA. The PCTB-FB coring BHA was pulled from the borehole and recovered to the Helix Q4000 by 1200 hr on 22 August 2023.
27 August 2023	The Geotek Cement Liner was lowered into the BHA, became stuck in the BHA, and the Helix Q4000 lost the ability to circulate drilling fluids through the BHA. It was interpreted that a 'hydraulic lock' had occurred with the pressure in the drill pipe above the liner being greater than the pressure below. After making a number of attempts to pull the Cement Liner from the BHA, the decision was made to cut the wireline connected to the Cement Liner at the surface and slip/cut wireline while tripping the BHA back to near the seafloor and to try again to pull the Cement Liner from the BHA. These additional attempts to pull the liner free also failed. After several more failed attempts to pull the liner free, the BHA was pulled back to the Helix Q4000. Upon the recovery of the BHA to the vessel, it was discovered that the running tool on the wireline was stuck inside the BHA drill collars and that a great deal of barite drilling mud sediment was packed off around the running tool.

Table T11: Three incidents where tools became stuck inside the bottom-hole assembly (BHA). PCTB-CS = Geotek Pressure Coring Tool with Ball Valve in the Cutting Shoe Configuration; PCTB-FB = Pressure Coring Tool with Ball Valve in the Face Bit Configuration

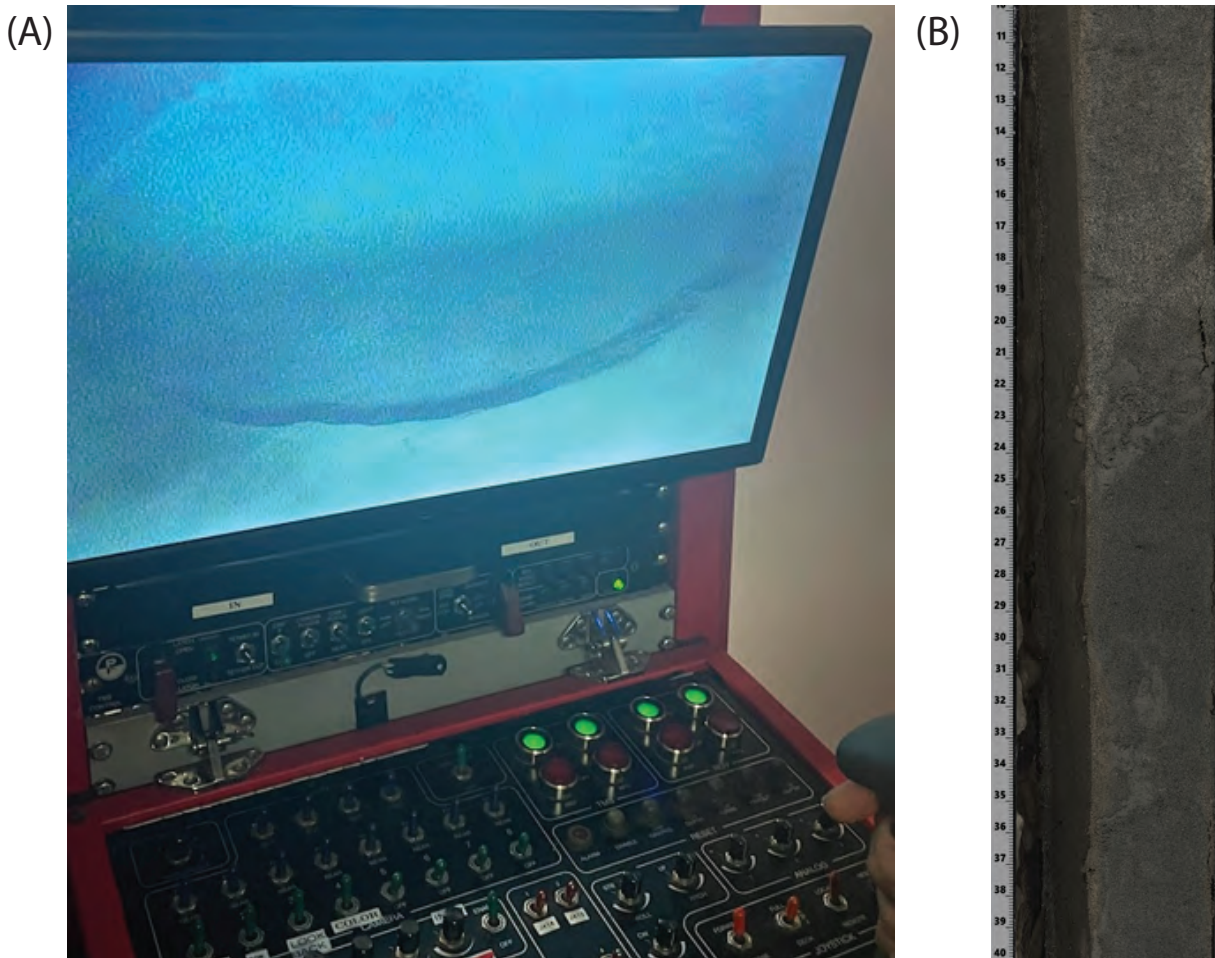


Figure F17: Images of the sandy seafloor. A) Photograph of the seafloor 'crater' present during drilling and coring. B) A 30 cm interval of split core image of Section H003-01H-2.

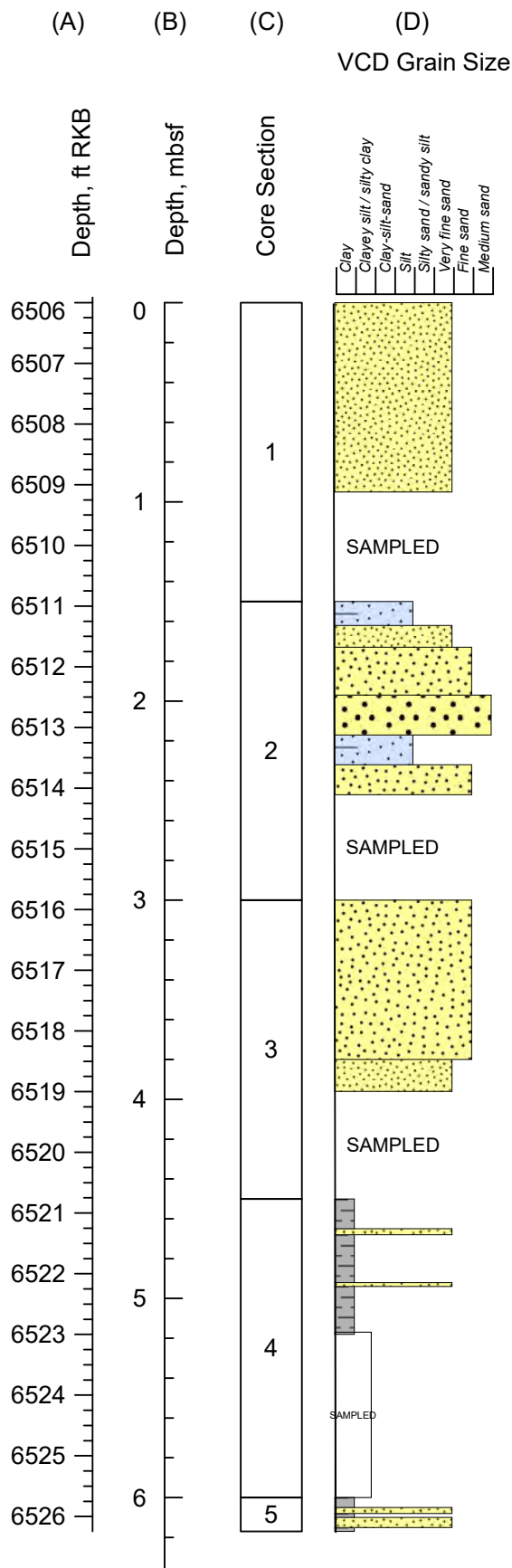


Figure F18: Visual core description (VCD) grain size at the top of Core H003-01H. This core was taken at the seafloor and was the first core taken during drilling. A) Depth below rig floor (RKB), B) Depth below seafloor, C) Core Section number, D) Visual core description of grain size. Yellow is sand. Blue is silt. Gray is clay.

approved Plug and Abandonment Plans (as described below) required additional written authorization from BSEE prior to enacting any changes. At the end of abandonment activities for Holes H002 and H003, BSEE deemed both wells to be compliant with federal regulations (30 CFR 250 Subpart Q).

The Plug and Abandonment Plan for Hole H003 required emplacement of a 300-ft cement plug about 150 ft above the uppermost significant gas hydrate-bearing zone (the Upper Blue sand). However, the total drilled depth of 7,505 ft RKB was significantly shallower than planned. UT submitted a request to BSEE to permanently abandon Hole H003 by filling the borehole with 11.0 ppg water-based mud (WBM) from total depth to seafloor. UT provided the technical justification that the weight and pumping pressure of cement in the shallow section would have exceeded the fracture gradient of the formation. BSEE subsequently approved UT's request.

Hole H003 was abandoned on 15 August 2023 by displacing the borehole from the total depth of 7,505 ft RKB to the seafloor with 115 bbls of 11.0 ppg WBM, followed by 110 bbls of 8.95 ppg seawater.

As with Hole H003, the Plug and Abandonment Plan for Hole H002 also required emplacement of a cement plug in the borehole beginning at approximately 150 ft above the uppermost significant gas hydrate-bearing zone (the Upper Blue sand) and extending upward for a minimum of 300 ft.

Upon achieving a total borehole depth of 9,332 ft RKB on 26 August 2023, the decision was made to plug and abandon Hole H002. A cementing liner was deployed into the BHA by wireline in preparation for cementing. Upon landing the cementing liner in the BHA, the BHA became blocked, and pressure increased to about 500 psi.

Repeated attempts to retrieve the cement liner were unsuccessful and the BHA was tripped out of the borehole to the rig floor by pulling double lengths of drill pipe and cutting the wireline below the top drive system. A new cementing BHA was assembled, and the borehole was successfully re-entered with

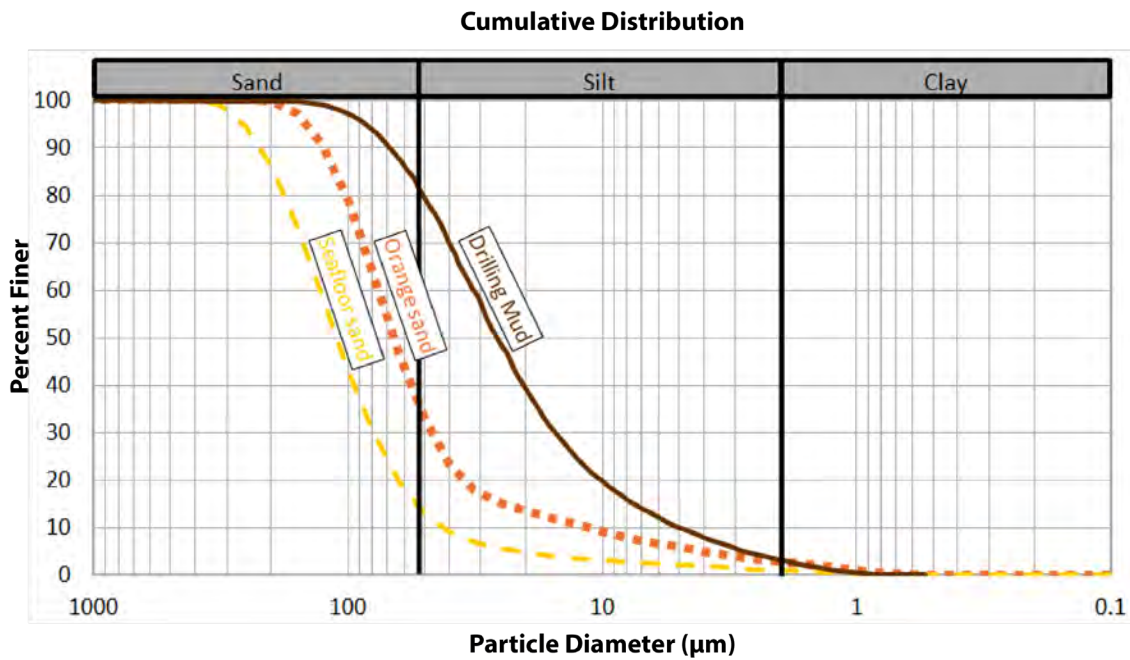


Figure F19: Examples of particle size distribution of sands encountered during drilling at Site H. Yellow dashed line: the sandy top of Hole H003 (sample H003-01H-3a_64-65 cm). Orange dotted line: the Orange sand interval from Hole H002 (Sample H002-09CS-4b_74-75 cm). Brown line: the barite in the water-based drilling mud as provided by M-I Swaco.

assistance from both Helix Q4000 ROVs to the total depth of 9,332 ft RKB on 29 August 2023.

Hole H002 was plugged on 29 August 2023 by pumping 11.5 ppg pad mud from the total depth of 9,332 ft RKB to up to 8,548 ft RKB, followed by 71 bbls of 16.4 ppg Class H cement plug. After the cementing job was completed, the cement was allowed to cure for 24 hours as required by BSEE. On 30 August 2023, after the cement had cured, the BHA was run back downhole to determine the depth of the cement plug. The top of the cement plug was encountered at a depth of 8,105 ft RKB (443 ft above the base of the cement plug). The integrity of the cement plug was tested with 15,000 lb of weight-on-bit, as required by BSEE. After confirming the integrity of the cement, the remaining upper section of the open borehole was displaced with 11.0 ppg WBM from 8,105 ft RKB to seafloor. The cementing BHA was then retrieved to the deck of the Helix Q4000.



Geotek Ltd. scientist Andrew Goodridge watches several output monitors while the Geotek pressure core and transfer system (PCATS) logs and images a pressure core. Photo credit: Geotek Ltd.

Scientific results

Coring

Figure [F20](#) illustrates the integrated coring program for Hole H002 and Hole H003. Hole H003 extended to 296.8 mbsf (Figure [F20](#), column G). In Hole H003, eighteen G-APC, one G-XCB, and ten PCTB cores were taken using one configuration of the tool (PCTB-CS) (Figure [F20](#), column I).

In Hole H003, continuous piston coring was performed to 7,015 ft RKB (155.1 mbsf) and thereafter intermittent cores were taken to a total depth of 7,480 ft RKB (296.8 mbsf) (Figure [F20](#), column I). Twelve temperature measurements were made in conjunction with some of the piston cores (APCT-3, Figure [F20](#), column H). Pressure cores were taken at about 100 ft (31 m) intervals from the seafloor down to 6,990 ft RKB (147.6 mbsf) to measure the buildup of the dissolved methane concentration with depth (Figure [F20](#), column I).

Hole H002 reached a total depth of 9,332 ft RKB (861.3 mbsf) (Figure [F20](#), column G). Only pressure cores were taken in Hole H002, and these were focused in and around the Upper Blue and Orange hydrate-bearing sands (Figure [F20](#), column I). Fifteen pressure cores were taken using two different configurations of the tool (PCTB-CS and PCTB-FB) (Figure [F20](#), column I).

Core recovery

From both boreholes, 533 ft (162.6 m) of conventional core was obtained. Cores were mostly expansive and conventional coring generally had recoveries greater than 100% (Figure [F20](#), column J). Core expansion resulted in an average recovery of sediment compared to the coring interval of 122%. G-APC cores were planned at less than the 31 ft (9.5 m) core liner length to account for expansion. This was accomplished by firing the G-APC a short distance above the top of the formation. G-APC deployments achieved full penetration through Core H003-21H (129 mbsf). G-APC refusal occurred with the acquisition of Core H003-25H when full stroke of the tool

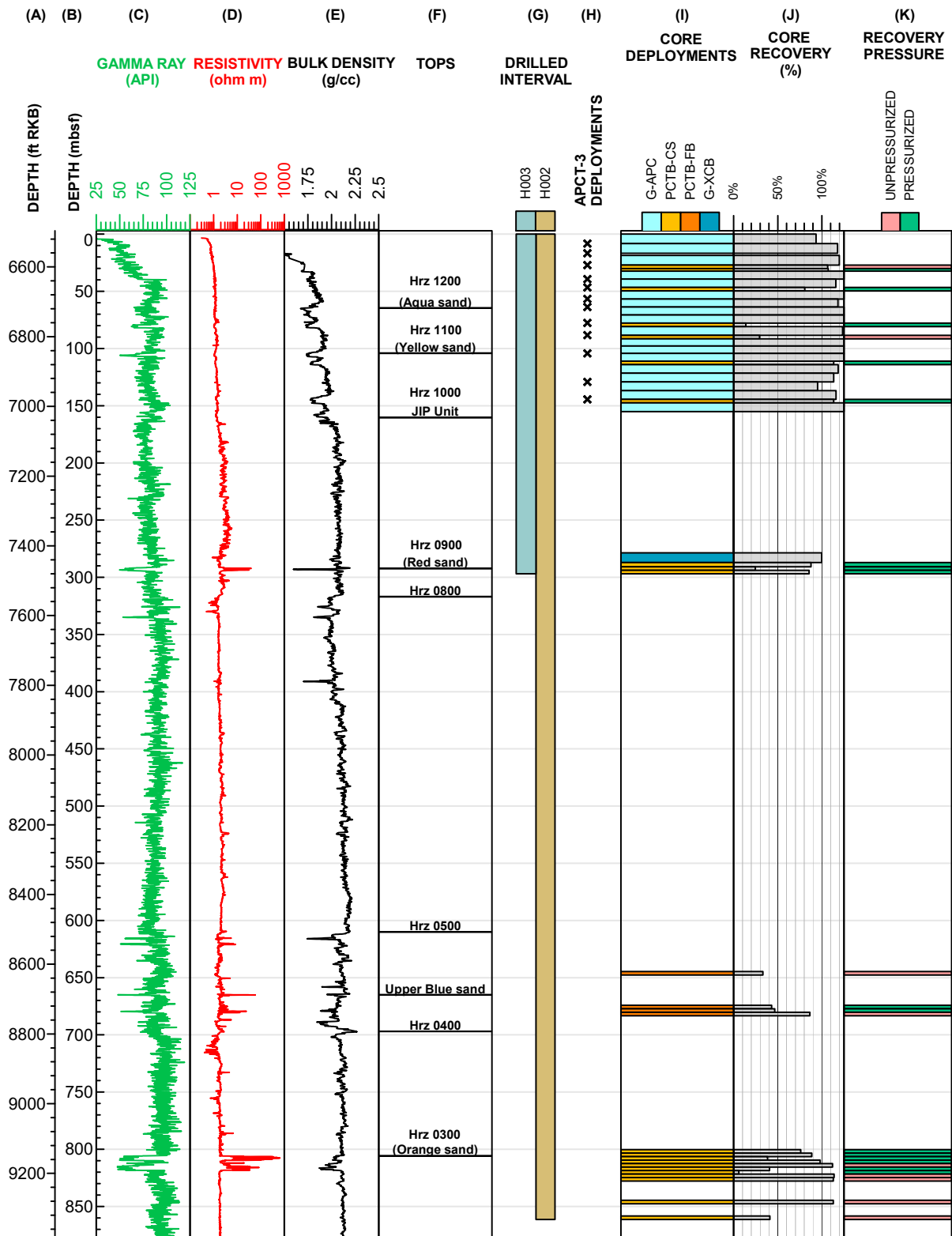


Figure F20: Core deployments and temperature measurements made during UT-GOM2-2. A) Depth in feet below rig floor (ft RKB); B) Depth in meters below the seafloor (mbsf); C) Logging while drilling (LWD) gamma ray in green; D) LWD resistivity in red; E) LWD bulk density in black; F) Seismic horizons (Hrz) and stratigraphic tops as described in Table T10; G) Drilled interval for Hole H003 in blue and Hole H002 in tan; H) In-situ temperature measurements made with APCT-3; I) Core deployments. Geotek Advanced Piston Cores (G-APC) are shown in light aqua blue. Geotek eXtended Core Barrel (G-XCB) cores are shown in dark aqua blue. Core acquired using the Pressure Coring Tool with Ball Valve (PCTB) in the Cutting Shoe Configuration (PCTB-CS) are shown in dark yellow and in the face bit configuration (PCTB-FB) in orange; J) Percent core recovery; K) Recovery pressure for the pressure cores measured with a pressure gauge on the rig. Cores recovered at elevated pressure are shown as green and at atmospheric pressure are shown as pink. The depth projection of Hole H001 LWD data onto Hole H002 and Hole H003, used in columns C, D, E, and F, is discussed in [Correlation of Hole H001 log data to Site H core data](#).

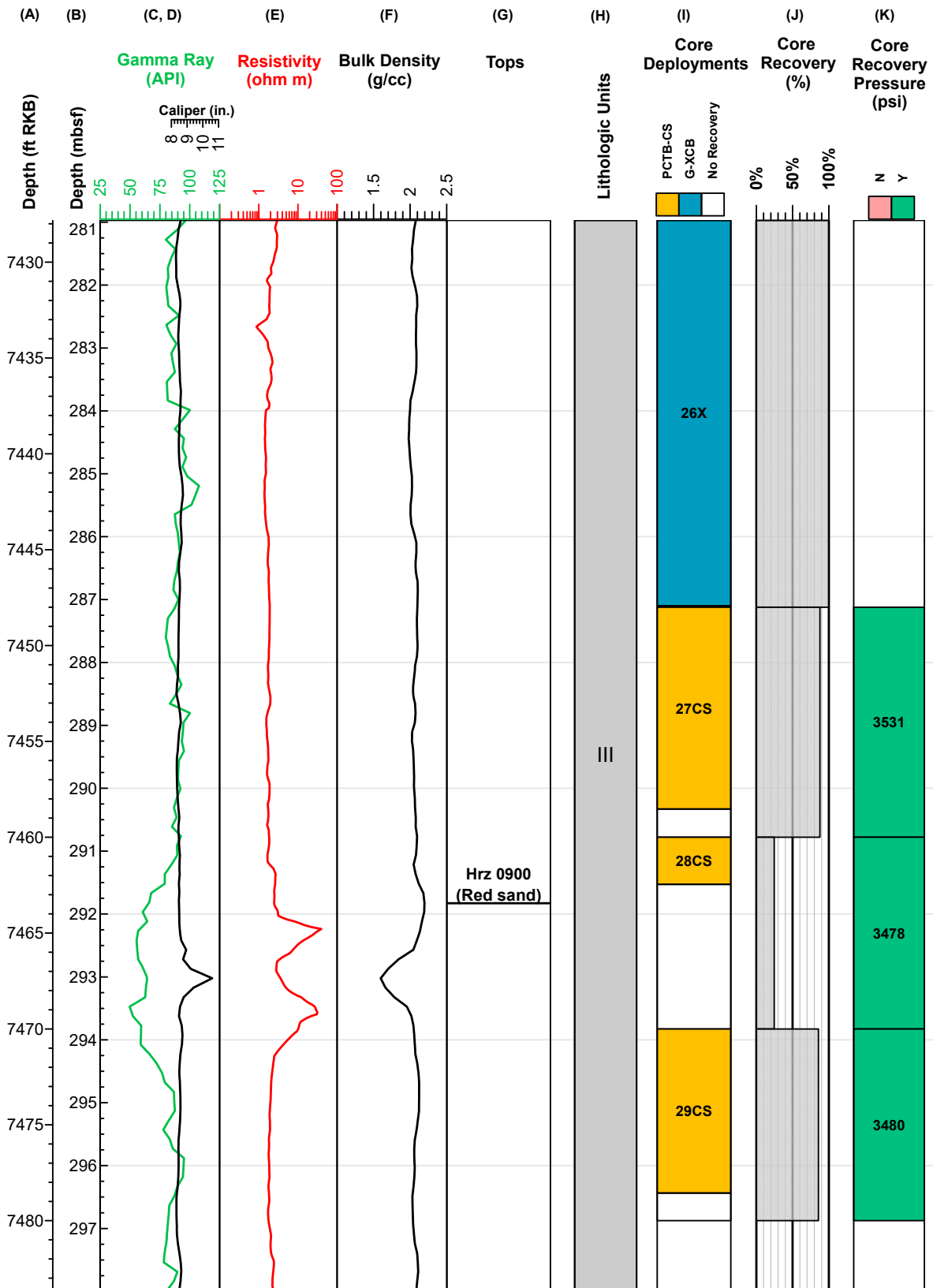


Figure F21: Core deployments at the Red sand. A) Depth in feet below rig floor (ft RKB); B) Depth in meters below the seafloor (mbsf); C) Logging while drilling (LWD) gamma in green; D) LWD caliper in black; E) LWD resistivity in red; F) LWD bulk density in black; G) Seismic horizons (Hrz) and stratigraphic tops as described in Table T10; H) Lithologic Units; I) Core deployments. Geotek eXtended Core Barrel (G-XCB) cores are shown in dark aqua blue, Pressure Coring Tool with Ball Valve (PCTB) in the Cutting Shoe Configuration (PCTB-CS) cores are shown in dark yellow. Area cored but no recovery is shown with gray diagonal hatches; J) Percent core recovery; K) Recovery pressure for the pressure cores measured with a pressure gauge on the rig. Cores recovered at elevated pressure are shown as green. The depth projection of Hole H001 LWD data onto Hole H002 and Hole H003, used in columns C, D, E, F, and G, is discussed in [Correlation of Hole H001 log data to Site H core data](#).

was not achieved. G-XCB coring was used to acquire Core H003-26X (278–287 mbsf).

Between the two boreholes, a total of 179.8 ft (54.8 m) of core was acquired from 25 deployments of the PCTB; there were four deployments of the Face Bit configuration (PCTB-FB), and 21 deployments of the cutting shoe configuration (PCTB-CS).

The PCTB-CS configuration enables the deployment of both conventional coring and pressure coring tools and was deployed in both boreholes. In contrast, the PCTB-FB has a unique BHA that does not allow the deployment of conventional coring tools and was only deployed in Hole H002. There was 105.0 ft (32.0 m) of core retrieved at elevated pressure (green zones, Figure F20, column K) and the remaining 74.8 ft (22.8 m) was processed as conventional core (pink zones, Figure F20, column K). After pressure coring, most of the pressure core was quantitatively degassed (See [Dissolved methane concentrations and hydrate saturation](#)) and processed as conventional core. There was 29.3 ft (8.92 m) of core kept at elevated pressure and transferred to UT for future testing.

During pressure coring, recovery was low in sand-prone sections. Figure F21 shows an example of the cores across the Red sand. In this case, three continuous pressure cores were taken (Core H003-27CS, -28CS, and -29CS). It is clear that in sands, where the LWD gamma ray values are low (Figure F21, column D), recovery is low (Figure F21, column J, Core H003-28CS). In contrast, where the section is more mud prone, recovery is much higher (Figure F21, column J, Core H002-27CS, and -29CS). This behavior was again observed during pressure coring of the Upper Blue and Orange sands.

Pressure coring tool performance

There were 14 pressure core deployments above HrZ 0400 (Blue). The recovery pressure of these cores was measured with a pressure gauge on the rig after the core had been chilled. The pressure and temperature history of each core was also measured during the deployment with data sensors (data storage tags) located inside the coring tool and on the wireline.

Ten pressure cores were recovered at elevated pressure (Figure F20, column J, green boxes). Four were recovered at atmospheric pressure (Figure F20, column J, pink boxes) when the PCTB failed to seal. Three of these four failures were due to fall-in sediment jamming the ball. Below HrZ 0400 (Blue), at the start of the Orange sand coring campaign, six cores were recovered at elevated pressure and five were recovered at atmospheric pressure.

All but one of the cores that sealed stayed within the hydrate stability zone (Figure F22, the orange dots lie at a higher pressure than the pressure required for hydrate stability [orange dots are below the green horizontal line]). One core, Core H003-27CS, appears to have drifted out of the stability zone for a few minutes, but the temperature sensor may not have been in contact with the core.

Most cores that sealed did not seal at coring depth (Figure F22, orange dots are above the white dots which mark the coring depth), but instead sealed as the core barrel was being raised in the pipe. Additionally, most cores showed excellent pressure boost performance, by boosting and maintaining the pressure of the core above the initial sealed pressure by several 100 psi or more (Figure F22, where the dark gray dots are at a higher pressure than the orange dots).

The pressure boost helps properly seat the upper seal ring and provides more margin between the core conditions and the hydrate stability boundary as the core is raised up the drill pipe through the warm water column.

Plotting core data as a function of depth

We plotted core data with two depth scales: 1) archived depth and 2) compressed depth (Figure F23). The archived depth for any point is determined by adding the depth of a particular measurement or sample within the core plus the depth of the top of the cored interval.

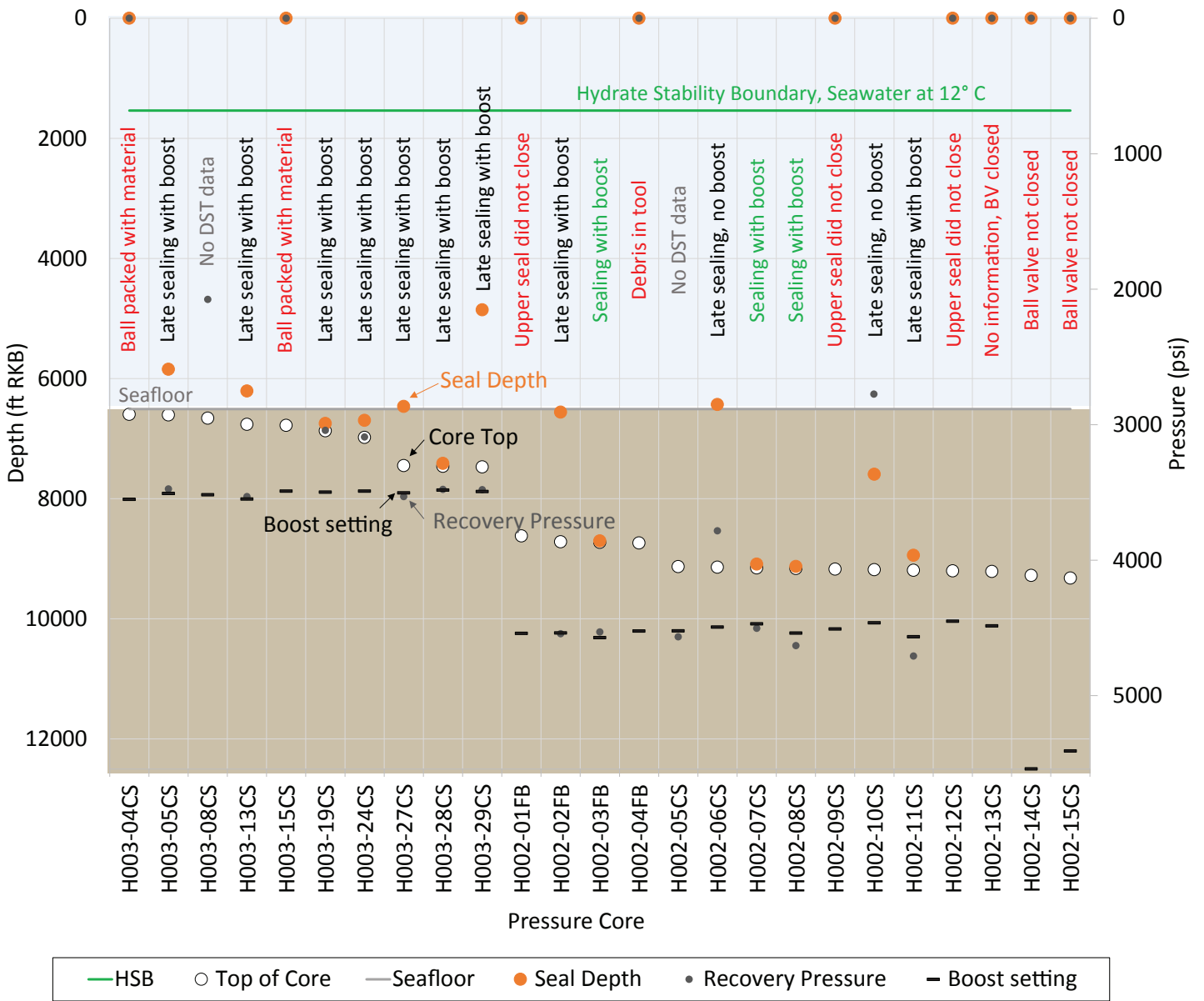


Figure F22: Interpreted depth when the pressure coring tool sealed (orange dots) for each of the 25 pressure coring deployments in Hole H002 and Hole H003. Core top depths (white dots). The boost pressure setting (black dashes) is a setting on a one-way valve that allows a pressure boost if the core pressure is lower than its set value. Seal depths and sealing times were determined from pressure and temperature data collected during the deployment using data storage tags and rig data such as the wireline depth. Recovery pressures (dark gray dots) were measured with a pressure gauge on the rig.

Due to the expansive nature of some of the cores, some of the recovered cores were longer than the cored distance. In these cases, when results from sequential cores are plotted versus archived depth, the results from one core can overlie upon results from the next core. To keep results in stratigraphic order, and to constrain any particular core data to within its cored interval, results are commonly plotted using compressed depth below seafloor (CD_{mbsf}).

The compressed depth below seafloor (CD_{mbsf}) of a specific sample (or measurement) was calculated

in the following way. First, the measured depth in section n ($D_{section, n}$) was converted to depth in core (D_{core}) by adding the depth in section ($D_{section, n}$) to the sum of the lengths of all sections above it ($\sum_{i=1}^{i=n-1} L_i$):

$$D_{core} = D_{section, n} + \sum_{i=1}^{i=n-1} L_i$$

Equation E4

Second, a compression factor (CF), which is unique to each core, was determined:

$$CF = \frac{L_{cored}}{L_{recovered}}$$

Equation E5

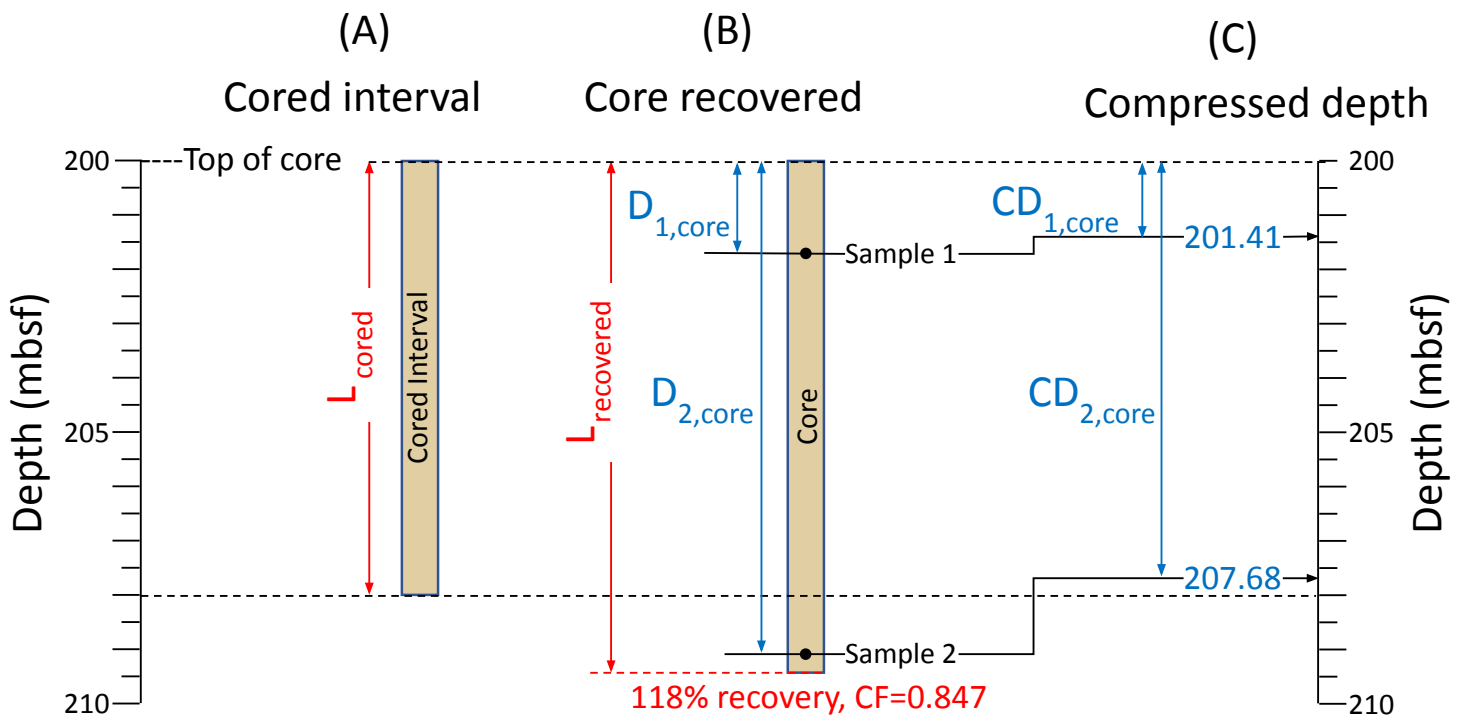


Figure F23: Illustration of how the compressed depth below seafloor (CD_{mbsf}) is calculated. A compression factor (CF) is calculated (Equation E5), which is the ratio of the length of the cored interval (L_{cored}) to the recovered interval ($L_{recovered}$). The recovered core in this case is longer than the cored interval and CF is equal to 0.847. CF is then used to convert sample depths in the core (D_{core}) to the compressed depth in the core (CD_{core}) (Equation E6). The sample compressed depth below the seafloor (CD_{mbsf}) is then calculated as the sum of the compressed depth in core (CD_{core}) plus the depth of the top of the core in meters below seafloor ($Top\ of\ core_{mbsf}$).

CF is the ratio of the cored interval (L_{cored}) to the length of the recovered core ($L_{recovered}$) for a particular core. It is the inverse of the core recovery. For example, for Core H003-02H, the cored interval was 8.53 m and the recovered length was 10.05 m, resulting in compression factor of 0.849 and a recovery of 118%.

In cases where the compression factor was less than 1 (recovery >100%), the archived sample depth in core was converted to its compressed depth in core (CD_{core}):

$$CD_{core} = D_{core} * CF$$

Equation E6

In cases where the calculated compression factor is greater than or equal to 1 (recovery \leq 100%), the compression factor was set to 1 and the compressed depth in core (CD_{core}) is equal to the measured depth in core (D_{core}).

The compressed depth below the seafloor (CD_{mbsf}) was then calculated by adding the compressed depth in core (CD_{core}) to the depth of the top of the core below the seafloor ($Top\ of\ core_{mbsf}$):

$$CD_{mbsf} = CD_{core} + Top\ of\ core_{mbsf}$$

Equation E7

This is the same approach used by the Integrated Ocean Drilling Program to determine what they call the core depth below the seafloor in compressed depths or CSF-B scale (IODP Depth Scale Task Force, 2011).

Lithostratigraphy

Lithologies

We encountered five dominant lithologies during coring at Site H. We name and describe each lithology below.

1. Massive Sand: Fine grained relatively homogenous sand (>80% sand-sized particles based on laser particle analysis (Figure F24, A, yellow circles). Smear slide composition is dominated by quartz, feldspar, and igneous and carbonate lithic grains (Figure F24, B, yellow circles).

2. Ooze: Light gray to tan carbonate ooze. Greater than 50% biogenic components (coccoliths and foraminifera) as defined in smear slide analysis (Figure F24, B, white circles). The remainder is most likely smectite clay (isotropic in smear slide).
3. Mud: Silty clay based on settling (hydrometer) analysis. Silt-sized particles within the silty clay are dominated by quartz and carbonate lithic fragments. The mud is dark gray in color (Figure F26, Photo B major lithofacies).
4. Silt: Graded silt to very fine sand in laminae to thin beds. The silts are a lighter color (Figure F26, Photo B, light tan minor lithofacies)
5. Sand: 1 – 20 cm graded beds. Sandy silt to silty sand based on laser particle size analysis. Smear slide composition dominated by quartz, feldspar, and igneous and carbonate lithic grains.

Lithofacies

Four lithofacies were defined based on the presence of one or more of these lithologies (Table T12), as illustrated in Figure F25, column I.

In zones where no core was taken (white zones,

Figure F25, column E), we inferred the lithofacies from the LWD data. We interpret the majority of these zones to be the Mud lithofacies (Figure F25, column I), which is composed of the mud lithology and the silt lithology (See [Lithologies](#)). The mud lithology (See [Lithologies](#)) is characterized by LWD gamma ray values from 80-100 API and LWD resistivity values generally between 1.2 to 2.0 Ωm . Small spikes of about 0.1 Ωm are interpreted to record the silt lithology (See [Lithologies](#)). These spikes may decrease if water is present in the pores or increase if hydrate is present in the pores. A small fraction of the section that was not cored is interpreted to be the Mud and Sand lithofacies (Figure F25, column I), which is composed of bedded sand and mud (See [Lithologies](#)). In these zones, sharp fluctuations of the LWD gamma ray and the resistivity curves record transitions from sand to mud.

Lithologic units

We described the downhole lithostratigraphy with seven successive lithologic units that are composed of one or several lithofacies (Figure F25, column H and I). These lithologic units are distinct from the LWD units (Figure F25, column G), which were determined prior to coring based only on LWD and seismic data.

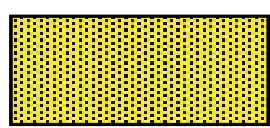
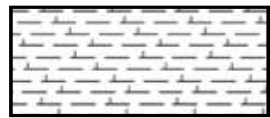
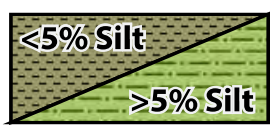
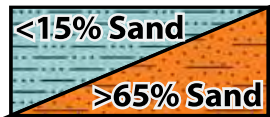
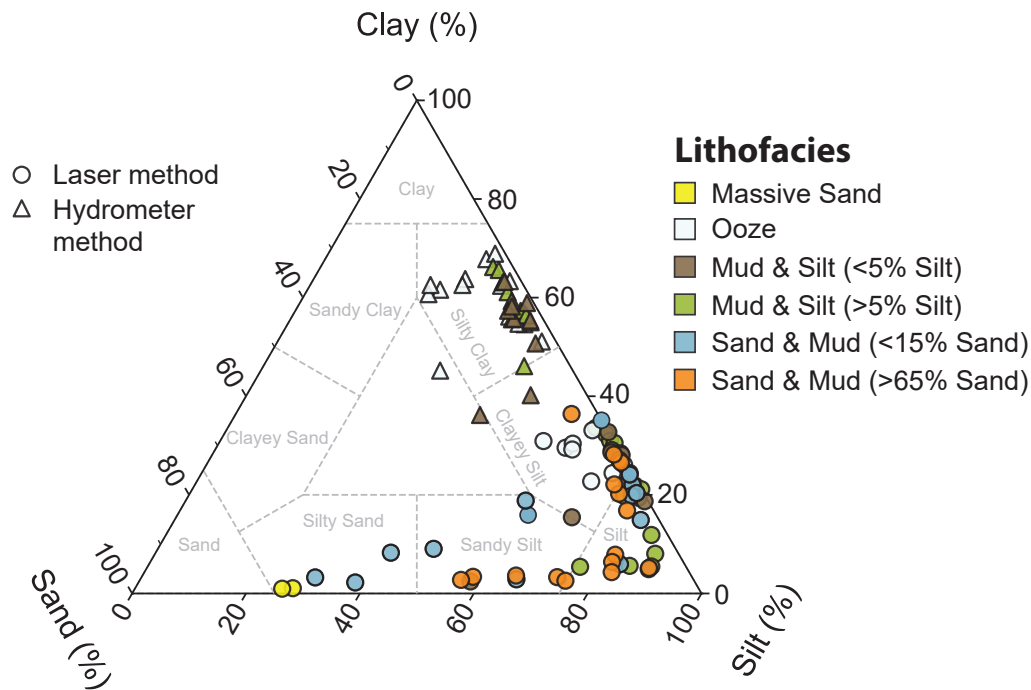
A) Lithofacies Legend	B) Lithofacies Name	C) Lithofacies Description
	Massive Sand	Massive Sand lithology
	Ooze	Ooze lithology
	Mud & Silt	Interbedded Mud and Silt lithologies. If Silt fraction is less than 5%, it is colored green. If Silt fraction is greater, it is colored light green.
	Sand & Mud	Composed of Sand and Mud lithologies. If less than 15% Sand, it is colored blue. If more than 65% Sand, it is colored orange.

Table T12: Lithofacies classification at Site H. Four lithofacies composed of one or more lithologies were defined (See [Lithostratigraphy](#)).

(A) Grain Size



(B) Composition

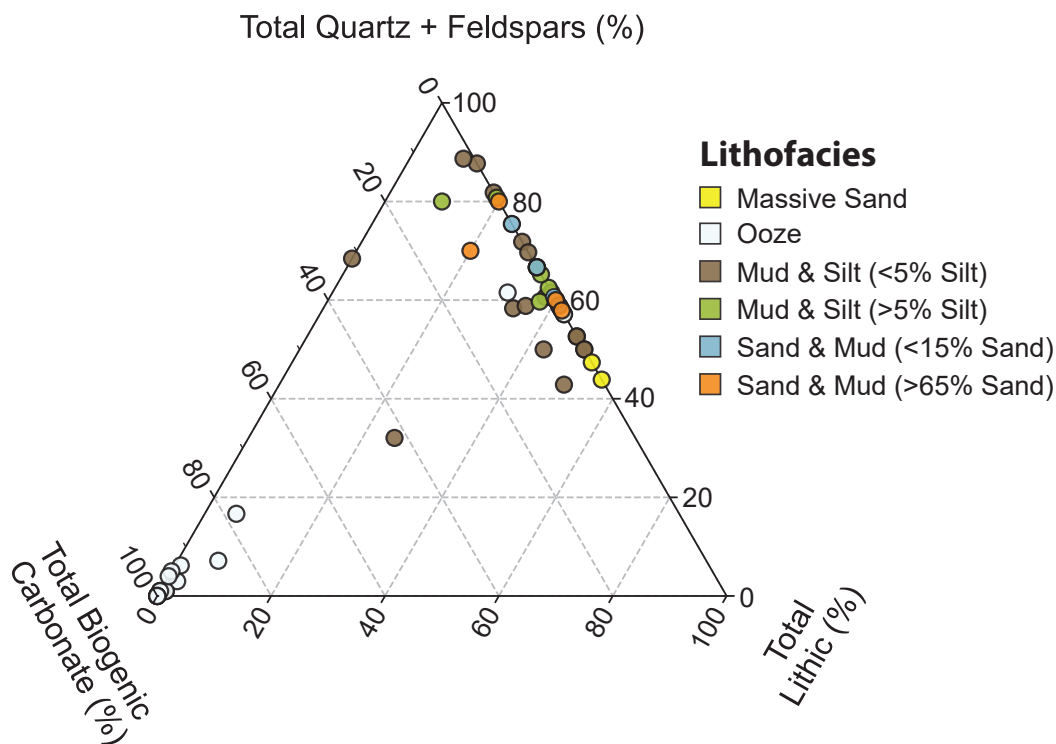


Figure F24: Ternary plots of sediment grain size and composition. Results are colored by lithofacies (e.g. Figure F25, Column I and Table T12); A) Ternary diagram modeled after Shepard's diagram (Shepard, 1954). In this representation, the clay-sized particles are assumed to be smaller than 2 microns and the silt-sized particles are assumed to be smaller than 75 microns as described in the Unified Soil Classification System (ASTM International, 2017). This approach is commonly used in geotechnical engineering and contrasts the approach commonly used by geoscientists wherein clay-sized particles are smaller than 3.9 microns and silt-sized particles are smaller than 62.5 microns (Shepard, 1954). Two methods were used to determine particle size distribution: laser particle analysis (circles) and hydrometer (triangles). The finer-grained lithofacies (Mud and Silt) plot as a clayey-silt when measured with the laser method whereas they plot as silty-clay with the hydrometer method. This is because the laser method commonly underestimates the fraction of clay-sized particles relative to the hydrometer method (Meazell et al., 2020; Wen et al., 2002). B) Ternary plot of the sediment composition derived from smear section analysis.

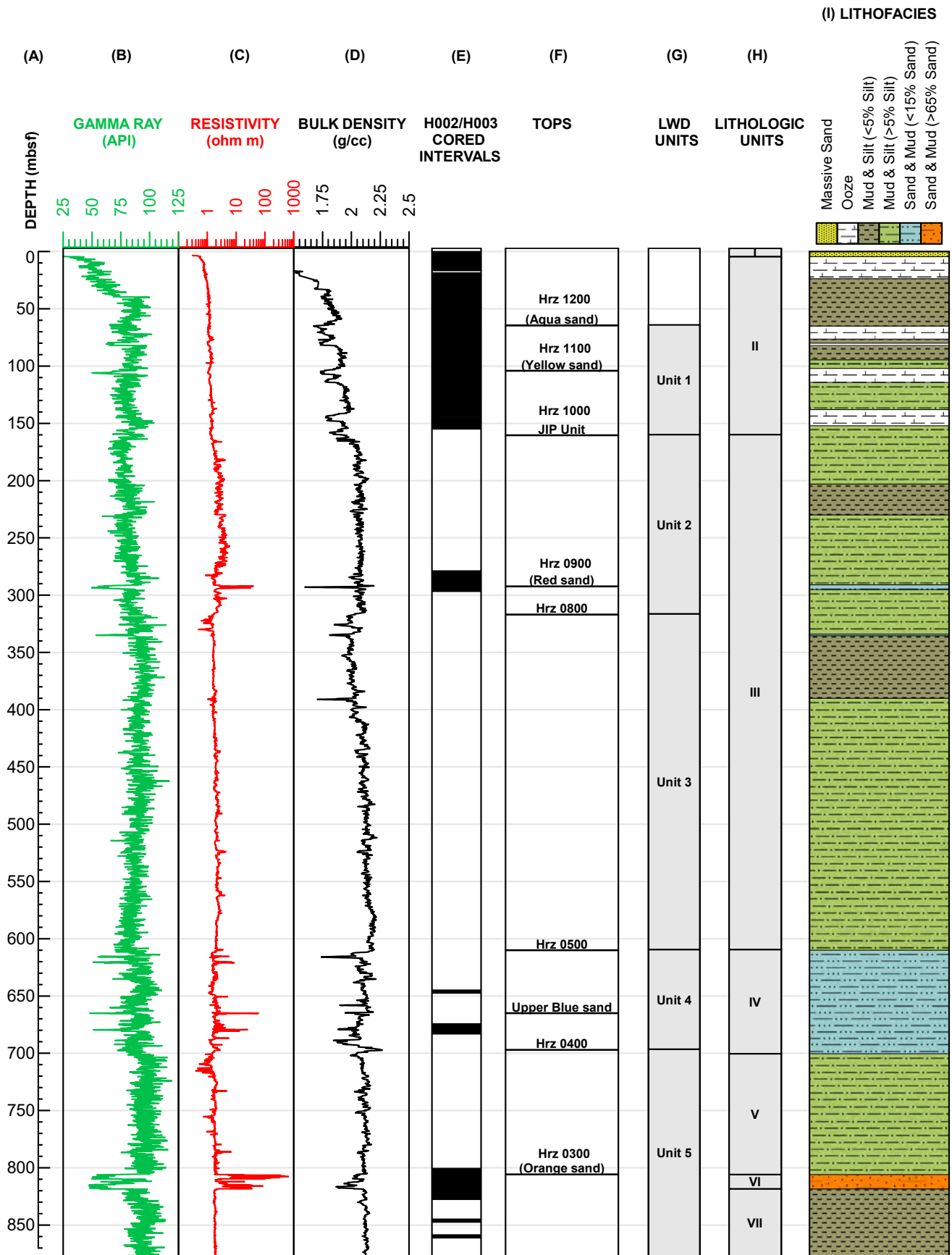


Figure F25: Site H Lithologic Units and lithofacies. A) Depth in meters below the seafloor (mbsf); B) Logging while drilling (LWD) gamma ray in green; C) LWD resistivity in red; D) LWD bulk density in black; E) Cored interval for Hole H003 and Hole H002 in black; F) Seismic events (Hrz = Horizon) and stratigraphic tops as described in Table T10; G) LWD units (See [Site H seismic and LWD interpretation](#)); H) Lithologic Units; I) Lithofacies at Site H, as defined in Table T12. The depth projection of Hole H001 LWD data onto Hole H002 and Hole H003, used in columns B, C, D, F, and G, is discussed in [Correlation of Hole H001 log data to Site H core data](#).

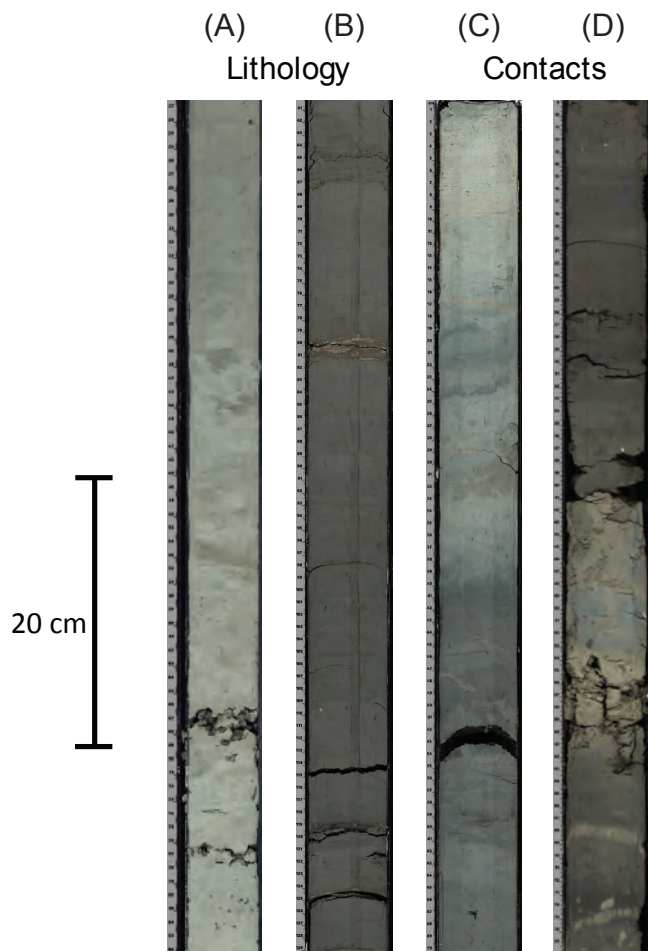


Figure F26: Lithologic Unit II (interbedded Ooze lithofacies and Mud lithofacies (Table T12) in split core line scan camera imagery. A) Foraminifera-bearing calcareous nannofossil ooze with bioturbation (Section H003-19CS-4); B) Mud lithofacies is dominated by silty clay (dark gray) but a millimeter scale silt beds are present (Section H003-20H-3); C) Gradational contact from mud to bioturbated carbonate ooze at the top (Section H003-12H-4); D) Sharp contact between bioturbated carbonate ooze, lower, and mud, upper (Section H003-25H-10-1); Rulers show archived depth.

Lithologic Unit I (0-4.5 mbsf): Lithologic unit I is composed of the Massive Sand lithofacies (Table T12) encountered at the seafloor (Figure F25; [Dissolved methane concentrations and hydrate saturation](#)). This sand was sampled by the first core, Core H003-01H, which recovered a sandy interval from 0-4.5 mbsf (Figure F18).

Lithologic Unit II (4.5-160 mbsf): The Ooze and Mud lithofacies (Table T12) are interbedded in Lithologic unit II. The Mud facies contains less Silt in the shallow part (4.5-95 mbsf) relative to the deeper section (95-152 mbsf) (Figure F25, column I, Figure F26, and Figure F27).

Relative to the Mud, the Ooze lithofacies (Table T12) has a high percentage of calcareous nannofossils (Figure F27, column H), a large porosity (Figure F27, column G), and a LWD bulk density (Figure F27, column D).

Lithologic Unit III (160-610 mbsf): Lithologic Unit III is dominated by the Mud lithofacies (Table T12). No Ooze is present. There is one Sand lithofacies present based on the LWD data (Red sand, Figures F21 and F25, column I). Recovery was poor in this interval.

Lithologic Unit IV (610-700.5 mbsf): Lithologic Unit IV is composed of the Mud and Sand lithofacies (Table T12, Figure F25, column I, and Figure F28, and expanded Figures F29 and F30). This unit represents the Upper Blue sand interval (Figure F25, column F).

Lithologic Unit V (700.5-805.75 mbsf): Lithologic Unit V contains only the Mud lithofacies.

Lithologic Unit VI (805.75-818.5 mbsf): Lithologic Unit VI is composed of the Mud and Sand lithofacies (Table T12, Figure F25, column I, and Figure F31). This unit is the Orange sand (Figure F25, column F). One conventionalized core, Core H002-09CS, was described and sampled for grain size analysis (Figure F32).

Lithologic Unit VII (>818.5 mbsf): Lithologic Unit VII is composed of the Mud lithofacies (Figures F25 and F31).

Calcareous nannofossil biostratigraphy

Discrete samples were collected onboard from core catchers (32 samples) and dockside from split core sampling (308 samples). All samples collected during operations, and a subset of 68 samples collected post-expedition, were examined for calcareous nannofossil assemblages.

Calcareous nannofossils were observed in nearly every sample examined from 0-296.4 mbsf (Hole H003). The preservation of in-situ specimens was very good. The background assemblage indicated a Pleistocene age (<0.91 Ma) through the entirety of the borehole.

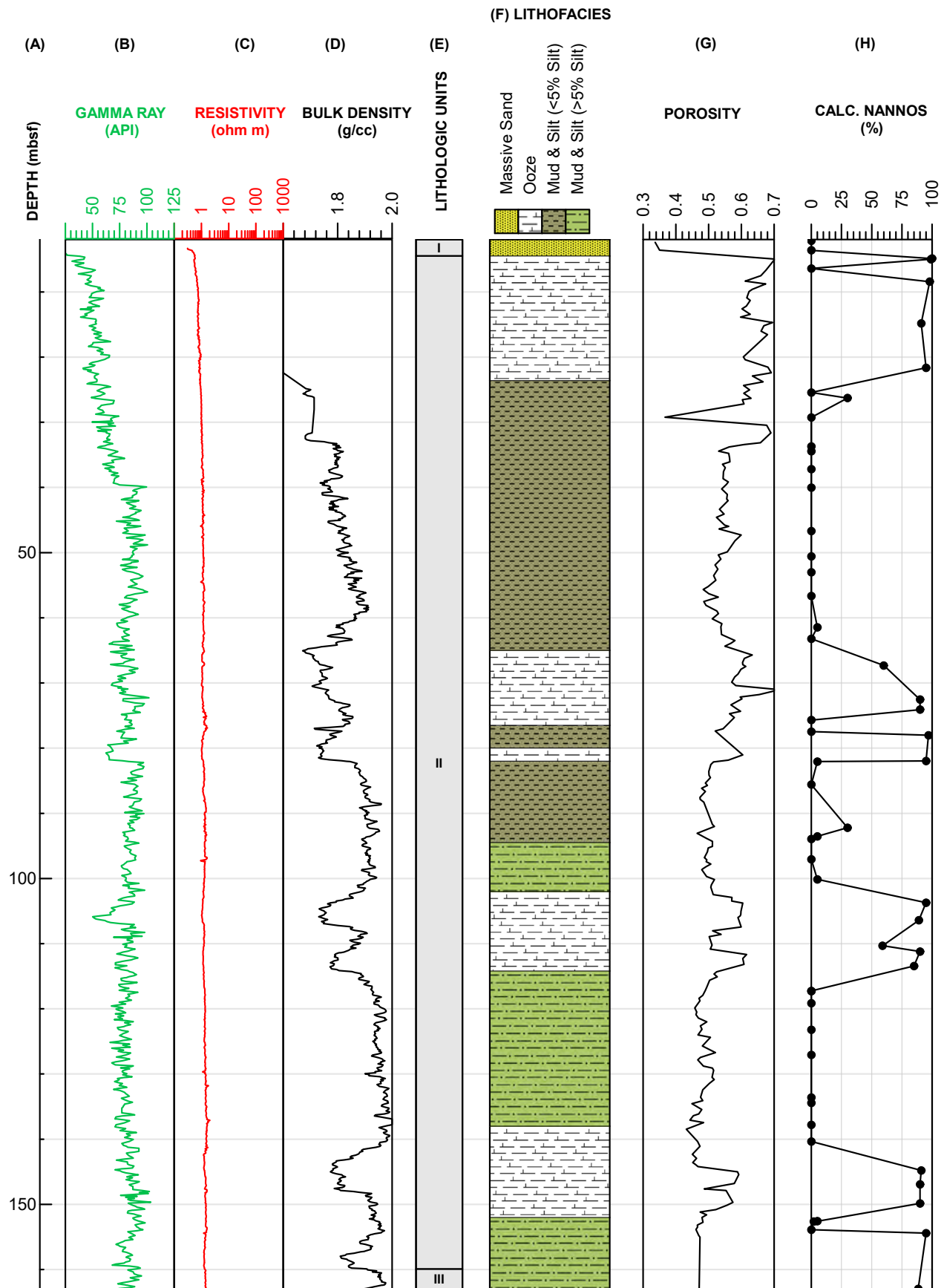


Figure F27: Lithologic Unit II. A) Depth in meters below the seafloor (mbsf); B) Logging while drilling (LWD) gamma ray in green; C) LWD resistivity in red; D) LWD bulk density in black; E) Lithologic Units; F) Lithofacies (Table T12); G) Porosity derived from moisture and density measurements on core in compressed depth. (See [Moisture and density measurements](#)); H) Fraction of calcareous nanofossils based on smear slide analysis in compressed depth. The depth projection of Hole H001 LWD data onto Hole H002 and Hole H003, used in columns B, C, and D, is discussed in [Correlation of Hole H001 log data to Site H core data](#).

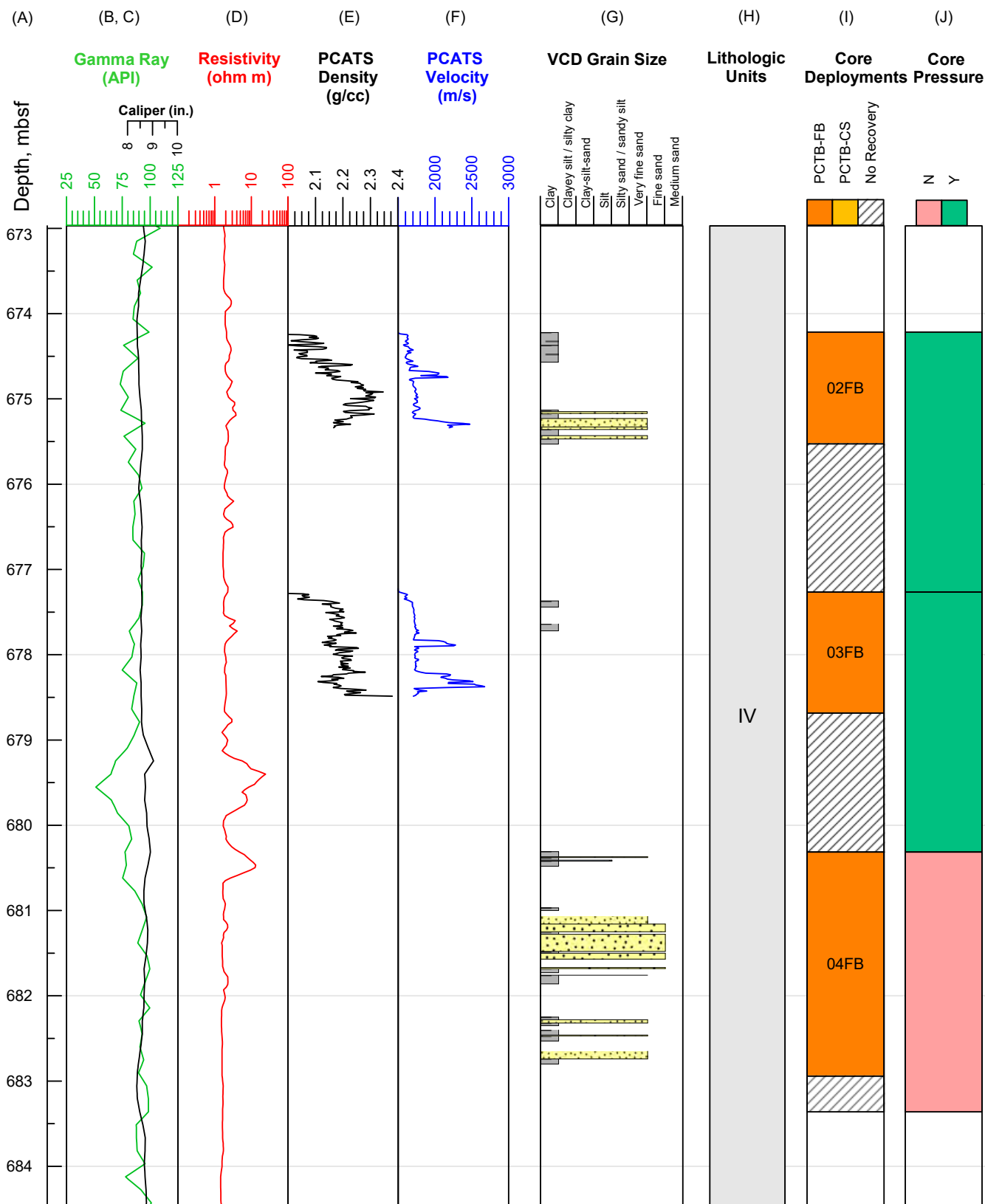


Figure F28: Representative interval of Lithologic Unit IV (the Blue sand interval). A) Depth in meters below the seafloor (mbsf); B) Logging while drilling (LWD) gamma ray in green; C) LWD caliper in black; D) LWD resistivity in red; E) Pressure Core Analysis and Transfer System (PCATS) pressure core density in black; F) PCATS pressure core P-wave velocity in blue; G) Visual Core Description (VCD) of grain size: sands = yellow, silts = blue, clay = gray; H) Lithologic Units; I) Core deployments using the Pressure Coring Tool with ball valve in the Face Bit configuration (PCTB-FB) in orange; J) Recovery pressure for the pressure cores measured with a pressure gauge on the rig. Cores recovered at elevated pressure are shown as green and at atmospheric pressure are shown as pink. The depth projection of Hole H001 LWD data onto Hole H002 and Hole H003, used in columns, B, C, and D, is discussed in [Correlation of Hole H001 log data to Site H core data](#).

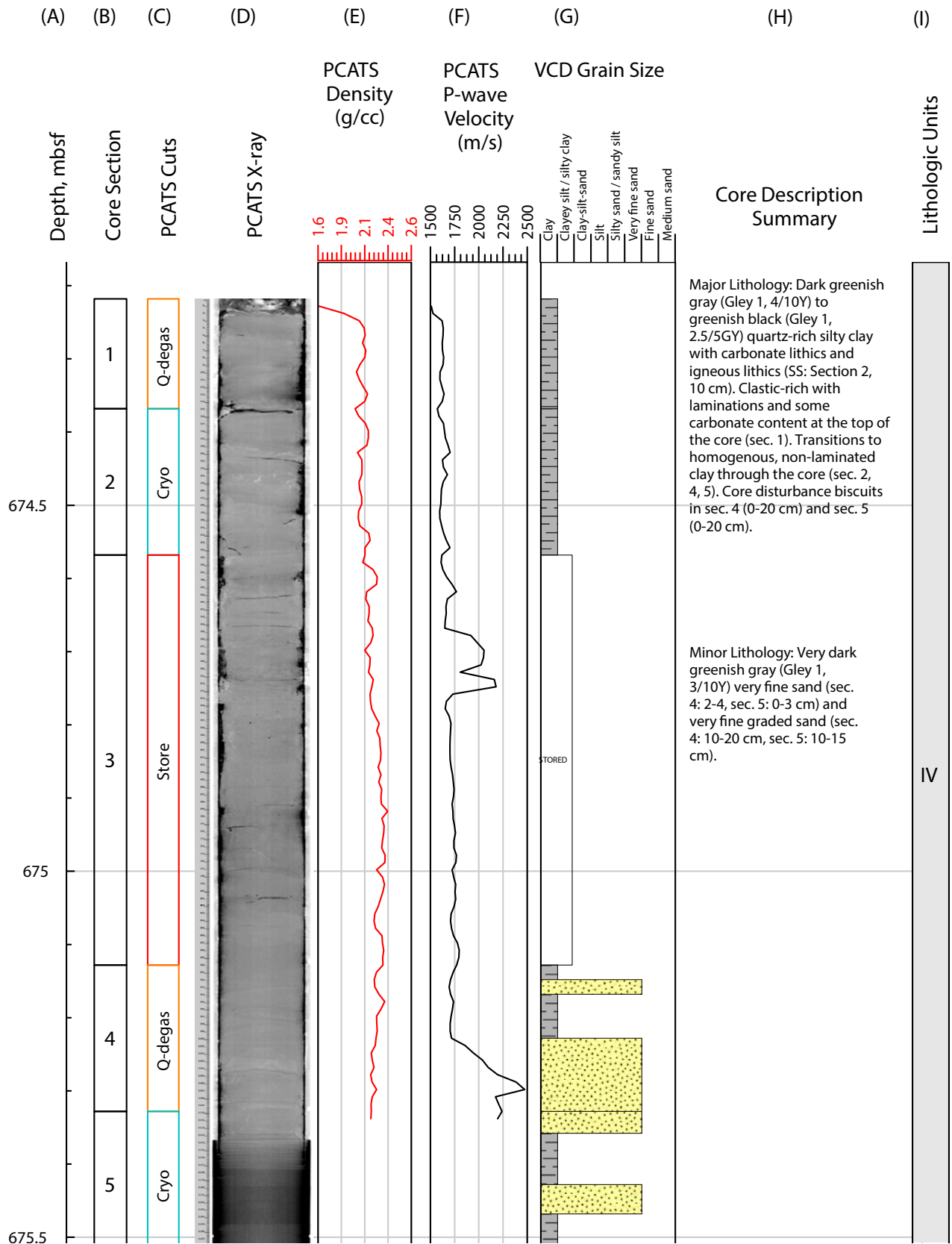


Figure F29: Expanded view of Lithologic Unit IV (the Blue sand interval), which is composed of the Sand and Mud lithofacies (Table T12) showing Core H002-02FB 674.2-677.3 mbsf (the larger interval is illustrated in Figure F28). A) Depth in meters below the seafloor (mbsf); B) Core section; C) Core allocation either to quantitative degassing (Q-degas), storage and later transported to The University of Texas at Austin (Store), or cryogenic freezing followed by depressurization for microbiology studies (Cryo); D) Pressure Core Analysis and Transfer System (PCATS) x-ray image (slab view of three-dimensional [3D] Computed Tomography [CT] data); E) PCATS pressure core P-wave velocity in red; F) PCATS pressure core density in black; G) Visual Core Description (VCD) of grain size: sands = yellow, silts = blue, clay = gray; H) VCD summary; I) Lithologic Unit.

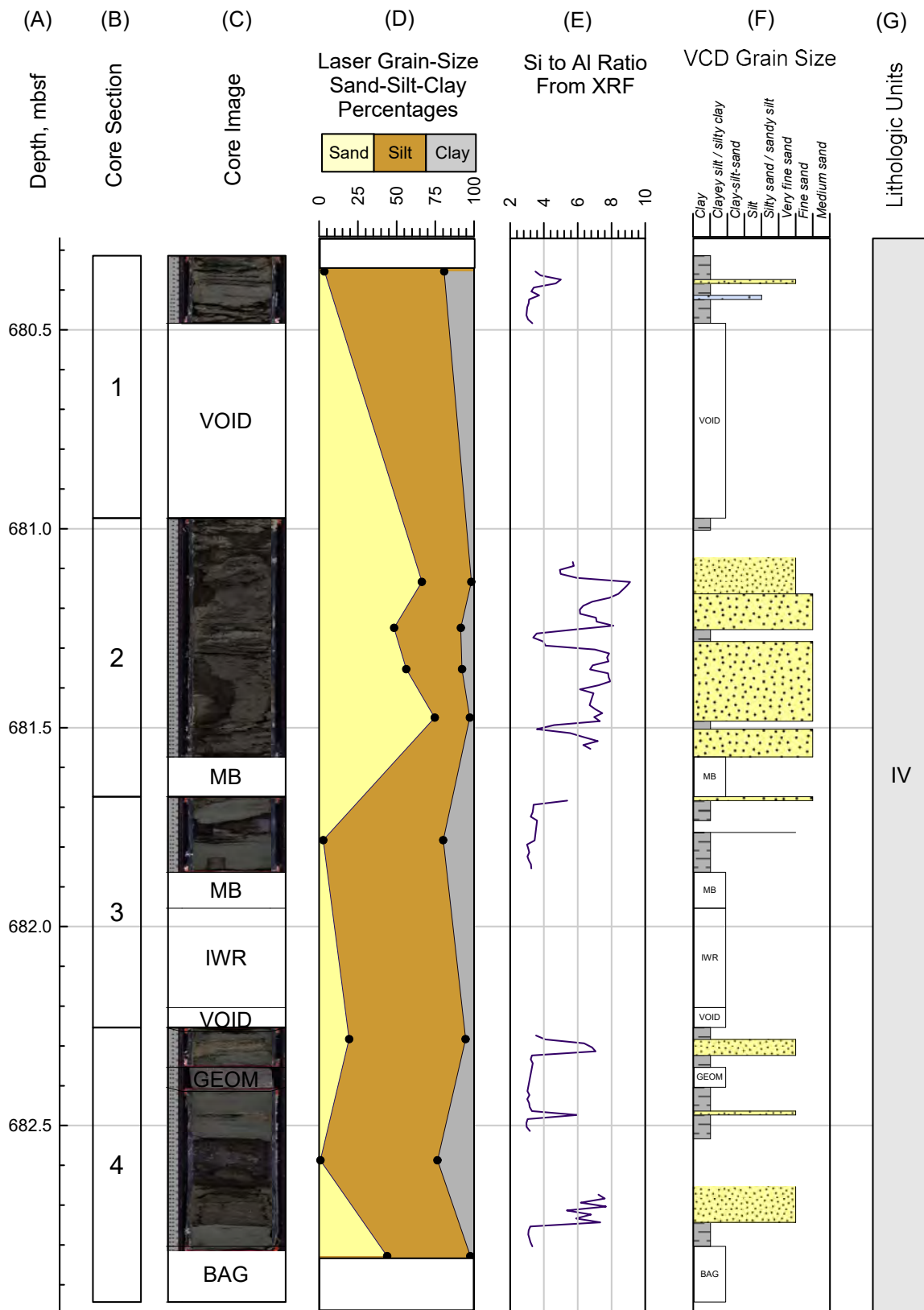


Figure F30: Expanded view of Lithologic Unit IV (Upper Blue sand) showing Core H002-04FB 680.3-683.3 mbsf (the larger interval is illustrated in Figure F28). This core was recovered at atmospheric pressure (Figure F28, column J) and thus, could be split, sampled, and described. A) Depth in meters below the seafloor (mbsf); B) Core section number; C) Split core images from the Geotek Line scanner; D) Grain size from laser particle analysis; E) Uncalibrated silicon to aluminum ratio calculated from x-ray fluorescence (XRF); F) Visual Core Description (VCD) of grain size: sands = yellow, silts = blue, clay = gray. Whole rounds removed before VCD are shown including samples for microbiology (sample code MB), routine pore water (sample code routine interstitial water or IWR). Voids (VOID) are also marked and were not described or scanned. H002-4FB recovery was less than the core throw, therefore archived and compressed depths are the same.

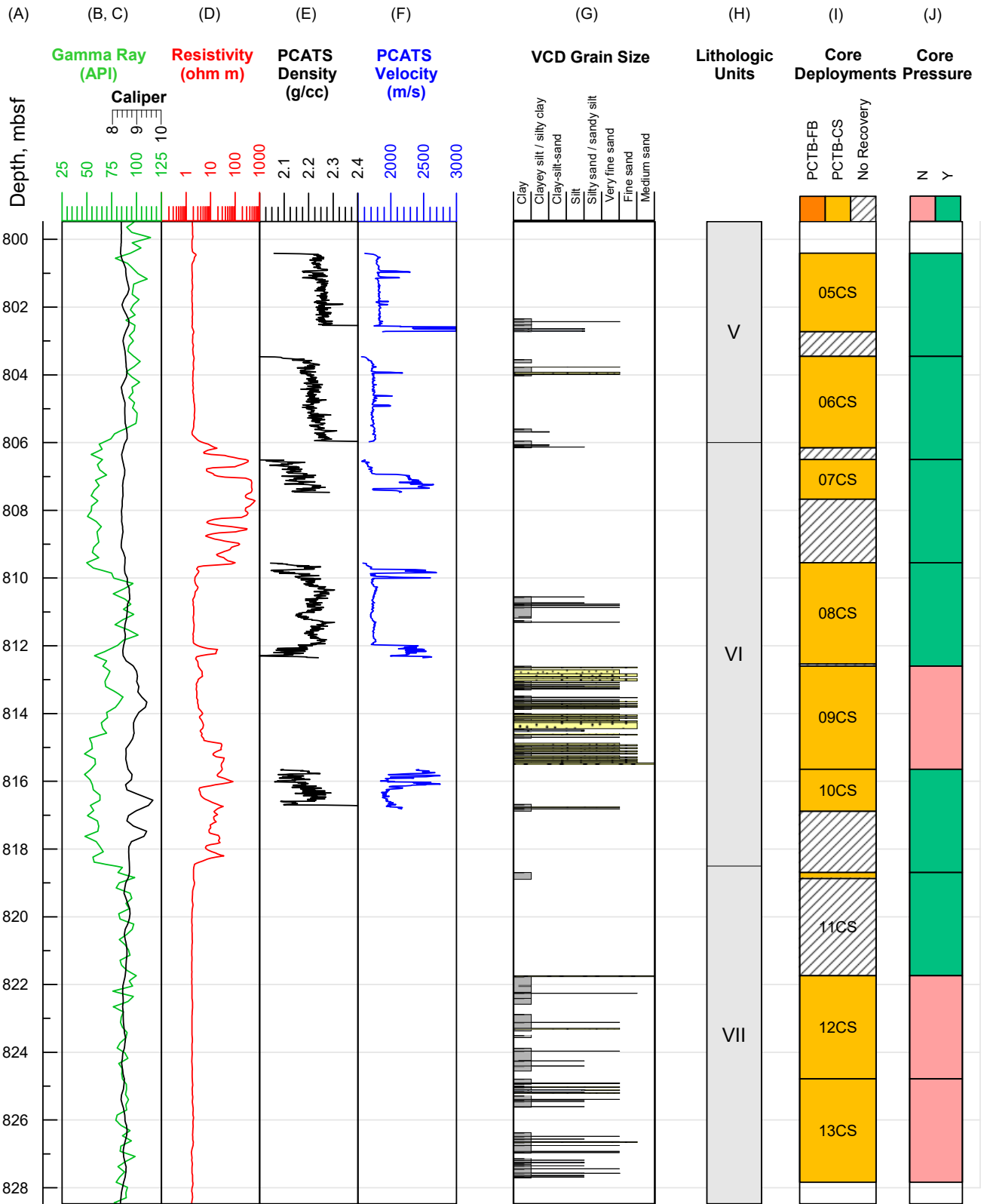


Figure F31: View of Lithologic Units V, VI and VII. Lithologic Unit VI is composed of the Mud and Sand lithofacies and is also called the Orange sand. A) Depth in meters below the seafloor (mbsf); B) Logging while drilling (LWD) gamma ray in green; C) LWD caliper in black; D) LWD resistivity in red; E) Pressure Core Analysis and Transfer System (PCATS) pressure core density in black; F) PCATS pressure core P-wave velocity in blue; G) Visual Core Description (VCD) of grain size: sands = yellow, silts = blue, clay = gray. H) Lithologic Units, I) Core deployments using the Pressure Coring Tool with ball valve in the Cutting Shoe Configuration (PCTB-CS) shown in dark yellow; J) Recovery pressure for the pressure cores measured with a pressure gauge on the rig. Cores recovered at elevated pressure are shown as green and atmospheric pressure are shown as pink. An expanded view of Lithologic Unit VI Core H002-09CS is presented in Figure F32. The depth projection of Hole H001 LWD data onto Hole H002 and Hole H003, used in columns, B, C, and D, is discussed in [Correlation of Hole H001 log data to Site H core data](#).

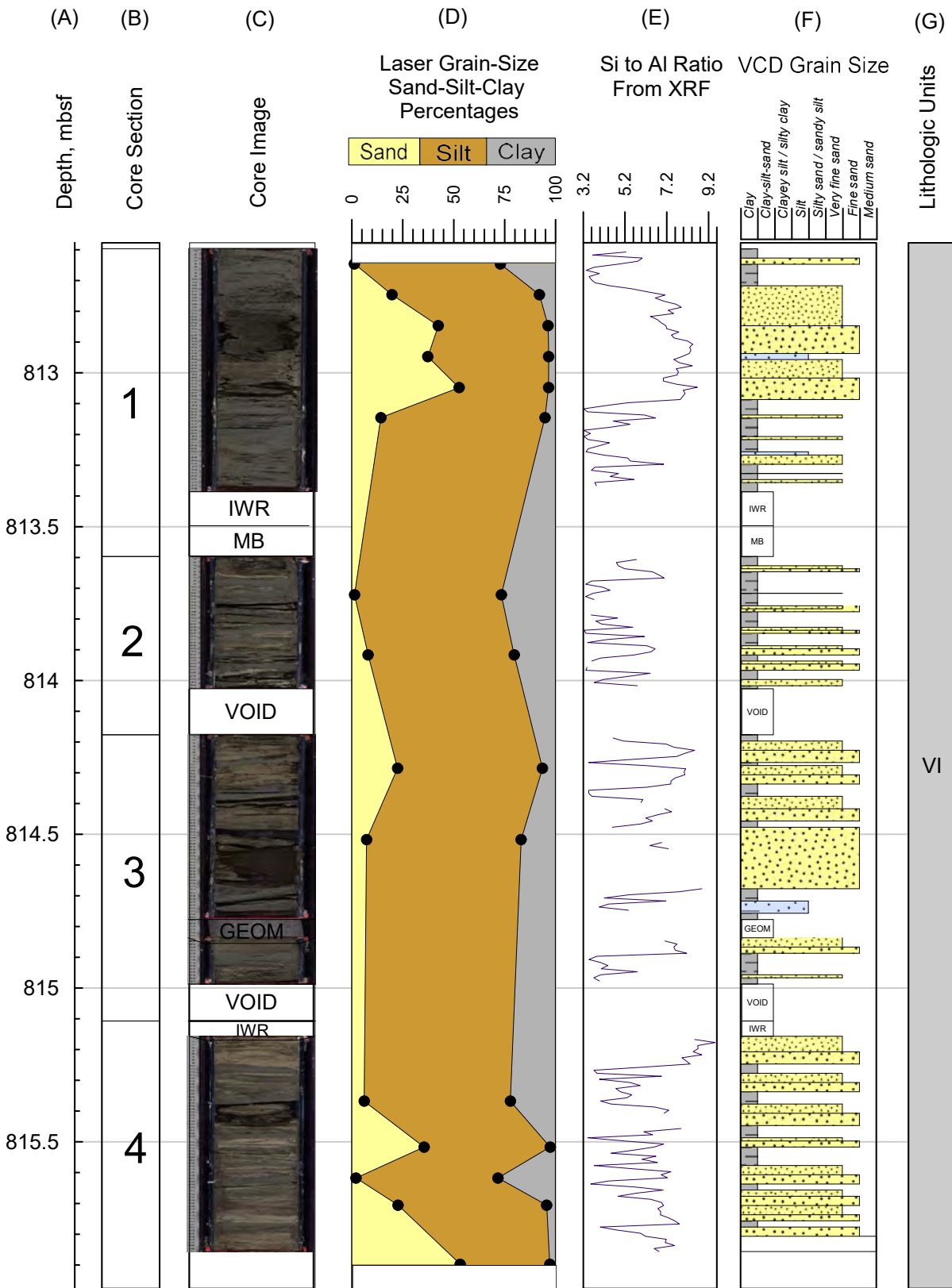


Figure F32: Expanded view of Lithologic Unit VI which is composed of Sand and Mud lithofacies. This is also part of the Orange sand (Core H002-09CS [812.6 to 815.6 mbsf]). This core was recovered at atmospheric pressure (Figure F31, column J) and thus could be split, sampled, and described. A) Depth in meters below seafloor (mbsf); B) Core section number; C) Split core images from the Geotek Line scanner; D) Grain size from laser particle analysis; E) Uncalibrated silicon to aluminum ratio calculated from x-ray fluorescence (XRF); F) Visual Core Description (VCD) of grain size: sands = yellow, silts = blue, clay = gray. Whole rounds included microbiology (sample code MB) and routine pore water (sample code routine interstitial water or IWR). Voids (VOID) are marked and were not described or scanned; H002-09CS recovery was greater than the core throw; all columns are plotted in archived, and not compressed depth.

Reworked (RW) calcareous nannofossils were accounted for and considered part of the detritus rather than of the in-situ Pleistocene microfossil assemblage. For the most part, there is an inverse relationship between assemblages dominated by RW Cretaceous and in-situ nannofossils indicating variable environmental conditions, such as changes in sea-level and/or continental runoff.

Four Pleistocene calcareous nannofossil biohorizons were observed from 0-296.4 mbsf (Hole H003) (Figure F33). Two of the age datums were cited from Gradstein et al. (2012): the crossover in dominance of *Gephyrocapsa spp.* to *Emeliana huxleyi*, and the first appearance datum (FAD, evolution) of *E. huxleyi*. The other two age datums, the last appearance datum (LAD, extinction) of *Pseudoemiliana lacunosa A* and the LAD of *P. lacunosa B* were cited from Waterman et al. (2017).

The LAD of *P. lacunosa* is a globally recognized age datum, but the LAD of *P. lacunosa B* is specific to the Gulf of Mexico and was statistically interpolated from the extensive onshore and offshore bioevent databases collected and curated by micropaleontologists at Paleo Data, a PetroStrat company (Waterman et al., 2017).

Two Pleistocene calcareous nannofossil biohorizons were observed from 644.6 to 859.6 mbsf (Hole H002) (Figure F33). The LADs of *P. pacifica* and *P. lacunosa C* are specific to the Gulf of Mexico and were also statistically interpolated from the extensive onshore and offshore bioevent databases collected and curated by micropaleontologists at Paleo Data (Waterman et al., 2017).

The first sample from Section H002-1FB-1b at 645.06 mbsf contained the marker species, *P. pacifica* (LAD 0.82 Ma), suggesting that the borehole and section is already within the *P. pacifica* biozone and that these strata are older than 0.82 Ma. The oldest biohorizon observed was the LAD of *P. lacunosa C* (0.83 Ma). The next calcareous nannofossil biohorizon would occur at 0.91 Ma, but it was not observed; therefore, the stratigraphy in the rest of the borehole is younger than 0.91 Ma.

Physical properties

Samples were collected to characterize the physical properties of sediment as a function of depth at high resolution. Initial measurements included:

- thermal conductivity
- in-situ temperature
- core logging (PCATS for pressure core and MSCL for conventional core)
- shear strength
- grain size
- moisture and density (porosity, density, saturation, and grain density)

In-situ temperature

Discrete measurements of in-situ temperature at multiple depths in Hole H003 were made. The advanced piston corer temperature tool (APCT-3) was used. The APCT-3 is an instrumented cutting shoe that measures temperature while coring with the Geotek Advanced Piston Corer (G-APC).

The in-situ temperature at a given depth is obtained by analyzing the APCT-3 temperature vs. time response during a coring deployment. For example, consider the APCT-3 deployment for Core H003-06H (Figure F34). First, the G-APC was lowered downhole until reaching the seafloor. The tool was stopped for 5 minutes, and drilling fluid pumps were turned off to thermally equilibrate the fluid in the pipe with the bottom water at the mudline.

After equilibration, the tool assembly was run into the bottom of the borehole and the G-APC shot into the formation to a depth approximately equal to the core throw (6.4-8.5 m). This generated a rapid temperature rise due to frictional heating. Heat then dissipated into the surrounding sediment, and the temperature at the APCT-3 decreases toward the formation in-situ temperature.

To allow significant dissipation, the G-APC is held in place for ~10 minutes while the APCT-3 records the temperature (dwell time). This dwell period rarely reaches in-situ temperature. Thus, temperature data

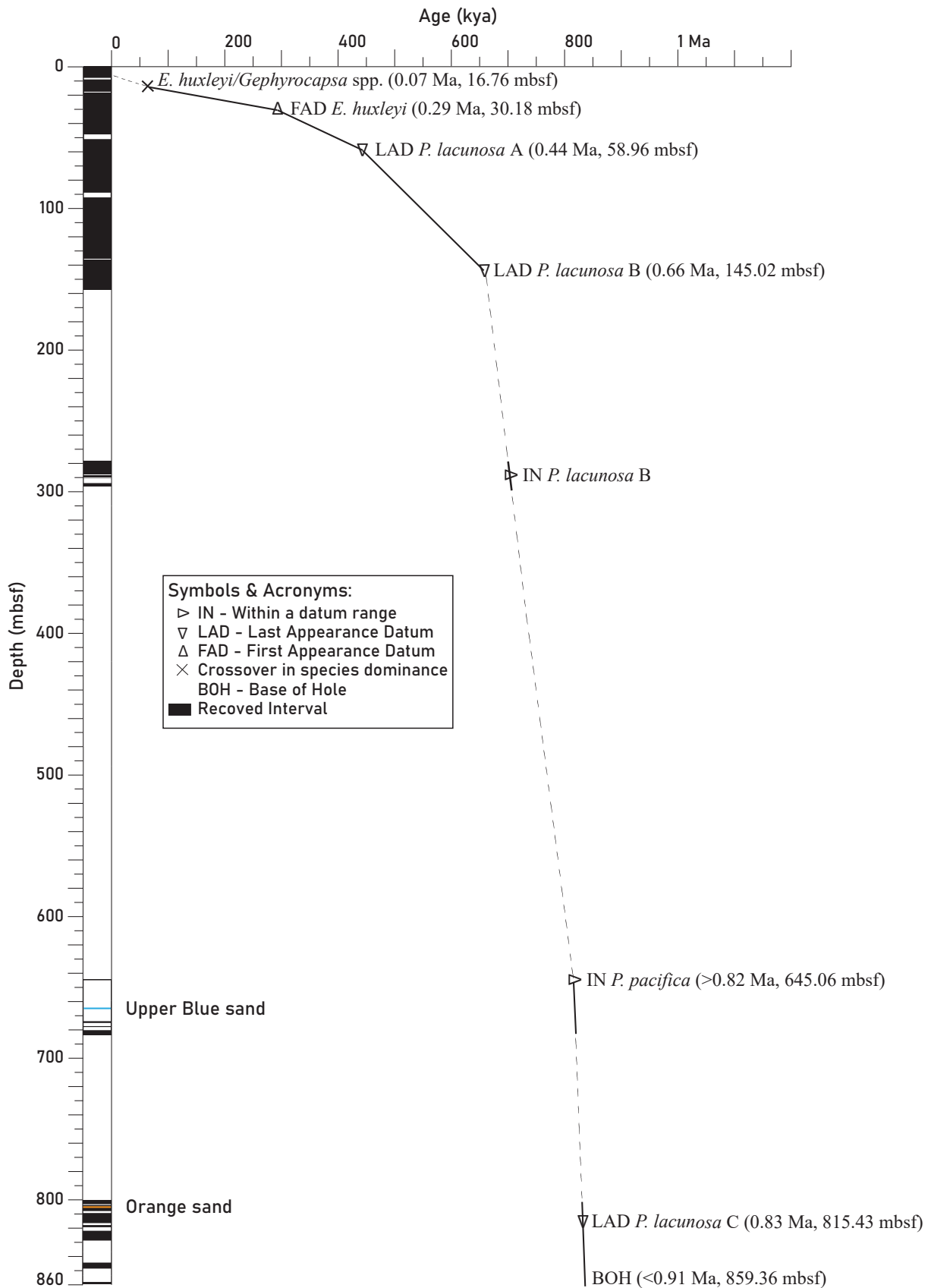


Figure F33: Composite time-depth plot of calcareous nannofossil biohorizons through Hole H003 and Hole H002 using compressed depths. Calcareous nannofossil events are from the Biostratigraphic Chart – Gulf Basin, USA (Waterman et al., 2017). Geologic time scale is that of Ogg et al. (2016). On the age-depth curve, solid black lines correlate with recovered intervals where samples were taken regularly for biostratigraphic analysis. Dashed black lines correlate with drilled intervals through which sediment samples were not recovered and biostratigraphic analysis could not be performed. First appearance datum (FAD, evolution) are shown as upright triangles, and last appearance datum (LAD, extinction) are shown as inverted triangles.

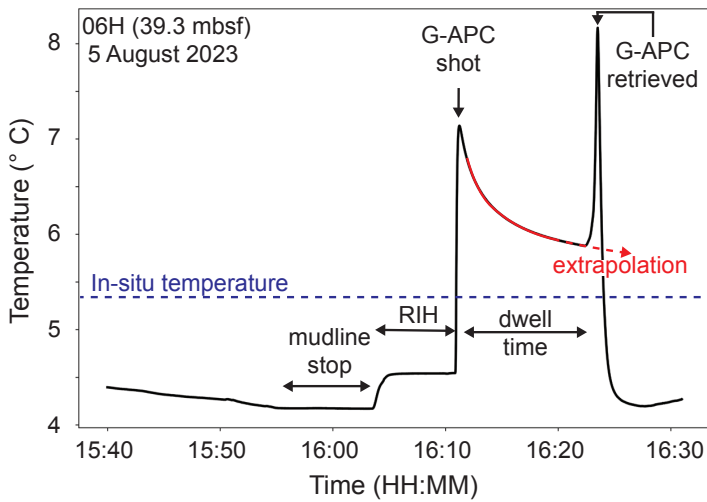


Figure F34: A typical Geotek Advanced Piston Coring Tool – 3 (APCT-3) temperature measurement. This example was collected during the deployment of Core H003-06H APCT-3 on 5 August 2023. The tool is lowered to the mudline and held for 5 minutes. Then the tool is run into the borehole and the Geotek Advanced Piston Corer (G-APC) is shot into the formation about 6.4-8.5 m, which causes the first temperature peak. The second peak corresponds to the retrieval of the coring tool, and the time in between the spikes is referred to as the dwell time. The data shown as red solid line is fitted with the theoretical impulse response of the tool to derive the in-situ temperature.

are fitted with the theoretical impulse response of the tool and extrapolated to infinite times (Figure F34, red line). The value at infinite time is estimated to be the in-situ temperature (Figure F34, blue line).

The inferred in-situ temperature profile with depth for Hole H003 is shown in Figure F35. The temperature gradient is 25° C/km. This value was obtained by fitting a linear trend of temperature with depth and disregarding the seafloor temperature, as the temperature at the seafloor may be more sensitive to environmental changes (e.g., ocean currents).

True vertical depth in meters below the seafloor (mbsf) was used rather than the archived depth to infer the temperature profile with depth. The estimated temperature gradient based on the depth of the BSR is estimated to be 17.5° C/km (Figures F35 and F36). The gradient of 17.5° C/km is an average value across the entire hydrate stability zone down to the BSR at ~895 mbsf. By contrast, this measurement-based temperature gradient of 25° C/km is for the first ~150 mbsf.

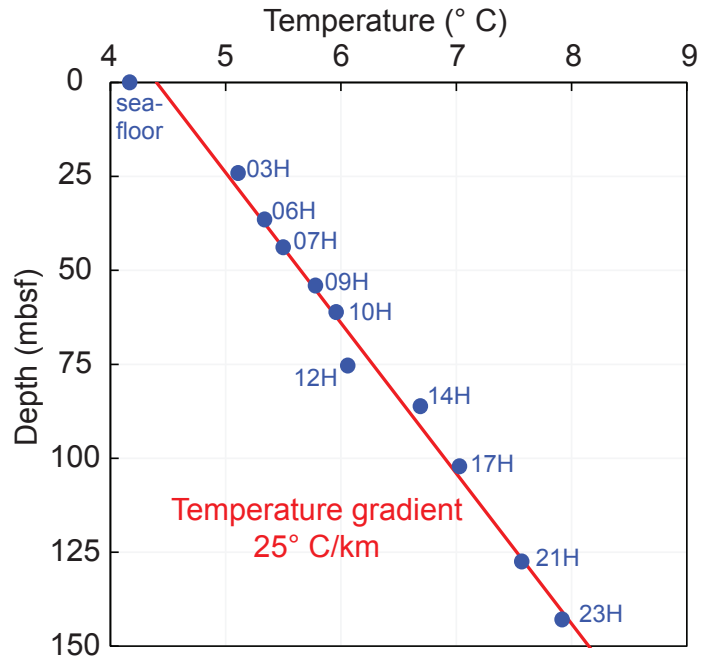


Figure F35: Interpreted in-situ temperatures at Hole H003 from seafloor to 150 mbsf (true vertical depth below the seafloor) based on Geotek Advanced Piston Coring Tool – 3 (APCT-3) measurements. The red line is a linear fit using least square regression, with an error of $R^2 = 0.99$. The seafloor temperature was excluded in this fitting procedure.

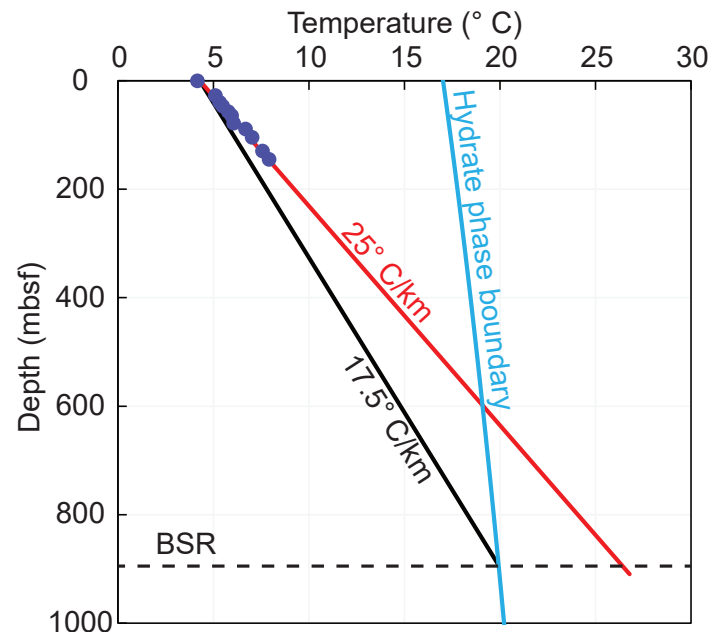


Figure F36: Temperatures with true-vertical depth below the seafloor at Hole H003. The gradient of 25° C/km (red line) is linear fit using measured temperature values (blue circles). The black line is the inferred linear temperature profile by considering the intersection between the bottom-simulating reflector (BSRs) depth (black dashed line), the hydrate phase boundary (light blue line) and the seafloor temperature.

Core logging

Pressure cores were sealed in the core barrel in the borehole to maintain close to in-situ pressure. Recovered pressure cores were maintained at pressure and logged for P-wave velocity and bulk density using PCATS on-board the vessel. Sections were identified and cut for analysis or storage. Whole round pieces were cut from depressurized sections for pore water, microbiology, and index properties. The remaining portion of the depressurized sections were then CT imaged in College Station, Texas, and logged for magnetic susceptibility at Salt Lake City, Utah.

Conventional cores were extracted from the G-APC or G-XCB and imaged with an IR scanner. The cores were then sectioned, whole round pieces were cut from sections for pore water, microbiology, and index properties, and strength measurements were made on the ends at the top and bottom of each section. Core sections were transported to College Station, Texas for MSCL logging and CT imaging. Core sections were then transported to Salt Lake City, Utah and whole round samples were cut from these cores for geomechanical analyses. All conventional and depressurized (conventionalized) sections were then split and imaged. All split cores were scanned for color spectrophotometry, magnetic susceptibility, and x-ray fluorescence; described, and sampled.

Figure [F37](#) shows an example from Hole H003 of the pressure core logs, images, and information about whole round sampling, plotted with the split core images. Figure [F38](#) shows an example of the conventional whole round core imaging, logging, sampling, and measurements plotted with the split core images. Figure [F39](#) shows an example of some split core logging and imaging data.

Strength measurements

There were 108 measurements of undrained shear strength with a pocket penetrometer and a handheld vane shear device made onboard. The majority (103 samples) were from depths 0-153 mbsf, which corresponded to G-APC cores 01H – 25H at Hole H003. An additional five samples were obtained in G-XCB

core 26X from 280-286 mbsf. Dockside, a total of 151 lab vane and fall cone measurements were collected for undrained shear strength with the majority corresponding to G-APC cores. All data are plotted in Figure [F40](#).

The undrained shear strength generally increases with depth, although not linearly, reaching 200 kPa. This increase is expected because the porosity decreases with depth, and the material gets more compacted the deeper it is buried.

Overall, the strengths measured with the handheld vane are lower than the strengths measured with the pocket penetrometer. In the onshore measurements, the strengths measured with fall cone are lower than the strengths measured with lab vane in most locations. In general, the strength measured with fall cone is the lowest, and the strength measured with pocket penetrometer is the highest in most locations. The G-XCB core 26X from 280-286 mbsf exhibited wide variations in the strengths compared to the G-APC cores 01H – 23H.

In lab measurements, the undrained shear strength varies more than three-orders of magnitude below 600 mbsf. The general trend is the strength increases with depth, reaching about 1,000 kPa at depths of about 850-860 mbsf.

Index properties

Physical property measurements are being made at Tufts University and UT. The results are still considered preliminary pending modifications based on measured grain density and salinity in the pore fluid.

Grain size analysis: Grain size analysis was done using both the laser and hydrometer methods. A cumulative distribution curve was generated for each sample. From this curve, the fractions of sand, silt, and clay were in two manners based on geological and geotechnical engineering definitions of size boundaries: 1) the engineering definitions of clay-size particles are less than 2 microns, silt-sized particles are between 2 – 75 microns, and sand-sized particles are larger than 75 microns, and 2) the

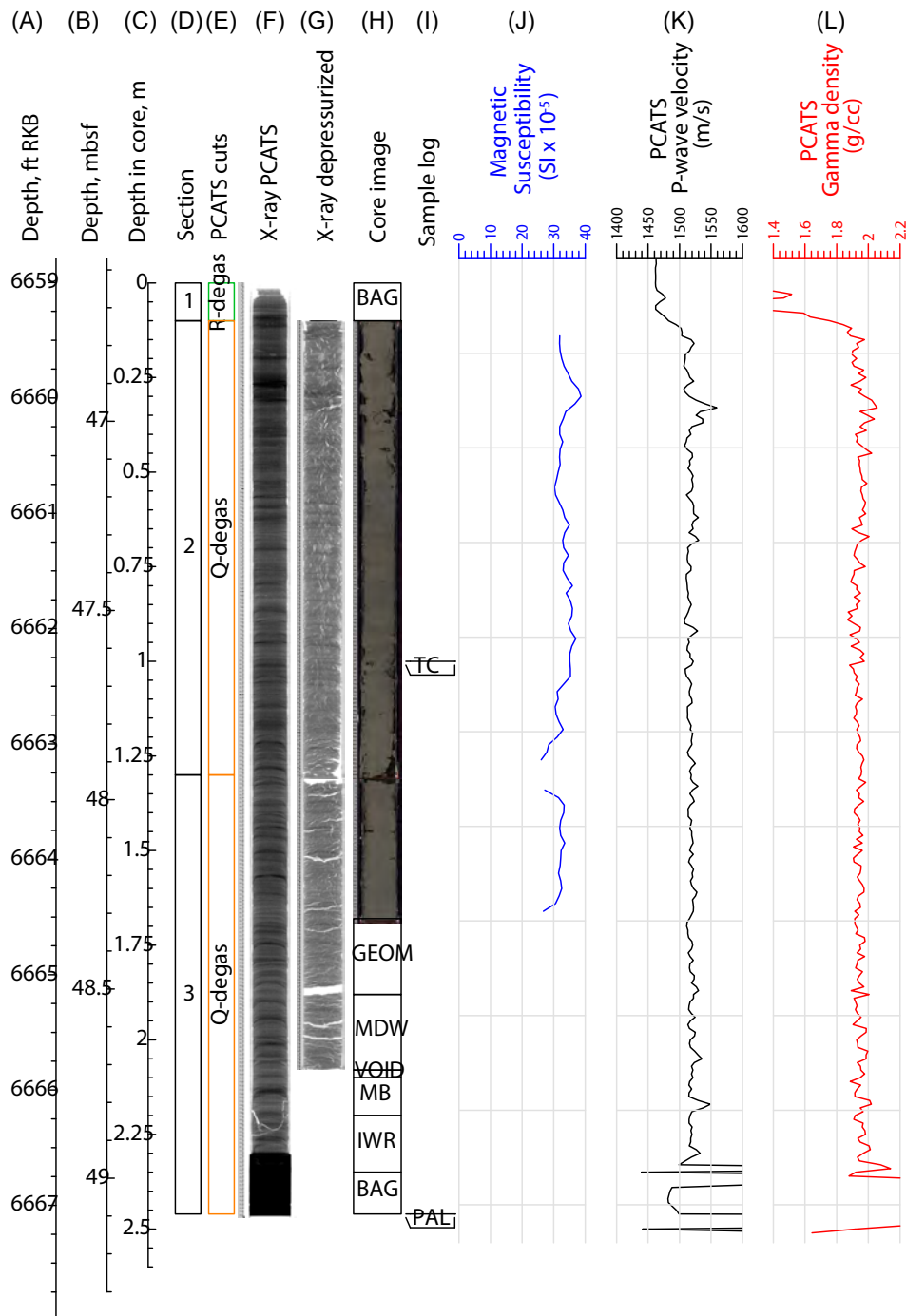


Figure F37: Example of data from analysis of a pressure core. Core H003-08CS was imaged and logged using the Pressure Core Analysis and Transfer System (PCATS) at close to in-situ pressure and temperature. H003-08CS was then cut at elevated pressure into two sections for quantitative degassing (Q-Degas, orange boxes). The remaining pressure core section, Section 1, was rapidly depressurized in PCATS (R-degas) and bagged for later assessment (sample code BAG) and a biostratigraphy sample (sample code PAL) was collected from the bagged material. After quantitative degassing, whole rounds were cut from section 3 for routine pore water analysis (sample code routine interstitial waters or IWR) and microbiology (sample code MB). The remaining whole round sections were imaged. Whole rounds were then cut for geomechanical testing (sample code GEOM) and moisture and density (sample code MDW) from section 3, and a thermal conductivity measurement was made on section 2 (code TC), magnetic susceptibility was then measured on Sections 2 and 3, and finally Sections 2 and 3 were split and processed as conventional core. A) Depth in feet below the rig floor (ft RKB); B) Depth in meters below the seafloor (mbsf); C) Depth in core; D) Core section number (number in black box); E) Core allocation (text in colored box); F) PCATS x-ray image (slab view of three-dimensional [3D] Computed Tomography [CT] data); G) Geotek Multi-Sensor Core Logger (MSCL) x-ray image (slab view of 3D CT after depressurization); H) Split core images with identification of sample locations after depressurization but before splitting; I) Measurement locations; J) Magnetic susceptibility using an MSCL loop scanner measured after depressurization but before splitting in blue; K) PCATS P-wave velocity in black; L) PCATS gamma density in red.

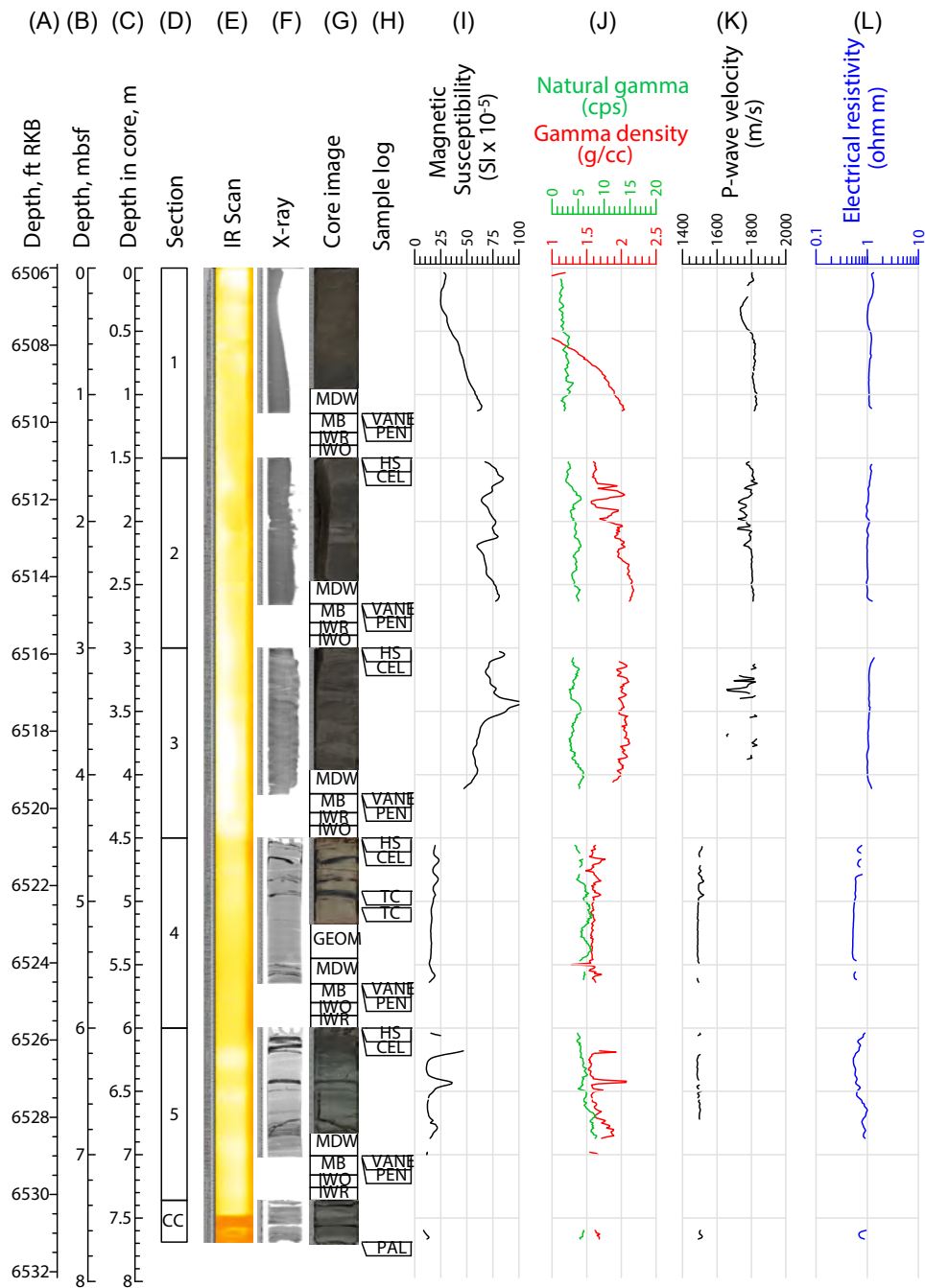


Figure F38: Example conventional core log for Core H003-01H. This mudline core penetrated the Massive Sand lithofacies. Core H003-01H was imaged with an infra-red scanner on a skate track (IR) just after the core was removed from the coring tool. Darker yellow areas are warmer. The core was then sectioned and whole rounds were cut from all sections except the core catcher (CC) section. A biostratigraphy sample (sample code PAL) was collected from the core catcher. Whole rounds included microbiology (sample code MB), routine pore water (sample code routine interstitial water or IWR), and organic pore water (sample code organic interstitial water or IWO). Headspace gas (sample code HS) and microbiology cell count (sample code CEL) samples were extracted from the top of sections 2-5. Sediment strength was measured using a hand-held vane (code VANE) and a pocket penetrometer (code PEN) at the bottom of sections 1-5. The remaining part of the sections were logged using the Geotek Multi-Sensor Core Logger (MSCL) and Computed Tomography (CT) images. The geomechanics (sample code GEOM) and moisture and density (sample code MDW) whole rounds were cut from sections after CT imaging but before splitting. Sediment strength measurements were again made on the ends of sections 1-5 using a table vane and fall-cone (locations not shown) before splitting. The split core was imaging and logging. A) Depth in feet below the rig floor (ft RKB); B) Depth in meters below the seafloor (mbsf); C) Depth in core (0 m is set at the top of the core sediment); D) Section identification (number in black box); E) Thermal image; F) MSCL x-ray image (slab view of three-dimensional (3D) CT after depressurization); G) Split core images; H) Identification of whole round sampling and measurement locations taken before splitting; I) MSCL magnetic susceptibility; J) MSCL natural gamma and gamma density; K) MSCL P-wave velocity, and L) MSCL electric resistivity.

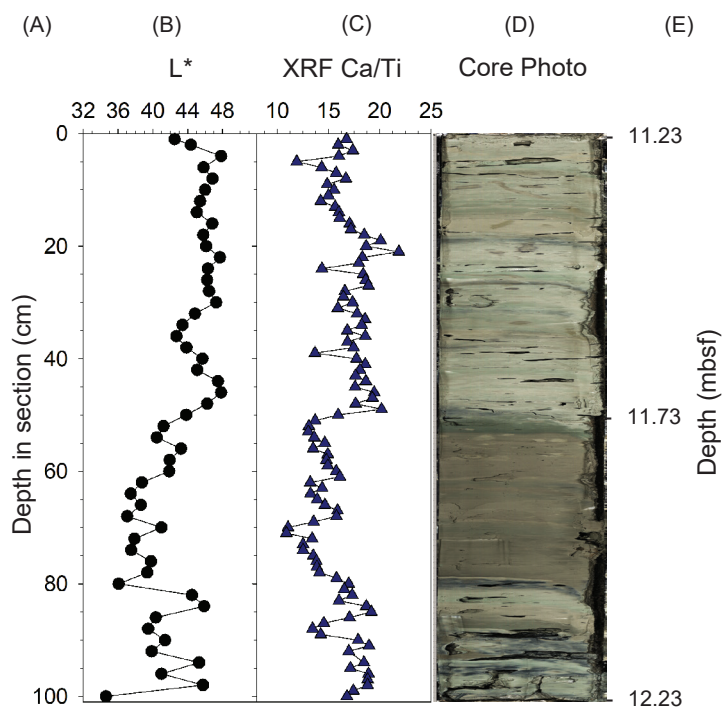


Figure F39: Example split core scan logs and split core image of core Section H003-02H-3. The archival half of the split core section was imaged and described, and smear slides were created, and the working half was sampled. After description the archival half was logging for magnetic susceptibility, x-ray fluorescence, and color spectrophotometry using the Geotek Multi-Sensor Core Logger Spectrophotometer (MSCL-S). A) Depth in core; B) Color spectrophotometry sediment lightness (L^*); C) Uncalibrated x-ray fluorescence (XRF) ratio of calcium (Ca) to titanium (Ti). Ca/Ti from XRF is a commonly used proxy for tracking the relative amount of carbonate versus lithogenic minerals (e.g. Gebregiorgis et al., 2020; Guo et al., 2021). Ca content is strongly influenced by calcium carbonate minerals (often foraminifer and calcareous nannofossil tests) and Ti is present in terrigenous minerals such as titanomagnetite and ilmenite. D) Split core photo; E) Depth in meters below seafloor (mbsf). All data is in archived depth.

geological definitions of clay-silt boundary of 3.9 microns and the sand-silt boundary of 62.5 microns. The results of these analyses using the engineering definition are presented in Figure F24, A. The size distributions for different lithofacies are discussed in [Lithostratigraphy](#).

Moisture and density measurements: Wet density (mass of wet sediment per unit volume) and water content (% ratio of water mass to dry sediment mass) were calculated from the measured sample volume, sample wet mass and sample dry mass. Core porosity was calculated using the measured density and saturation and assuming a grain density of 2.7 g/cc, a

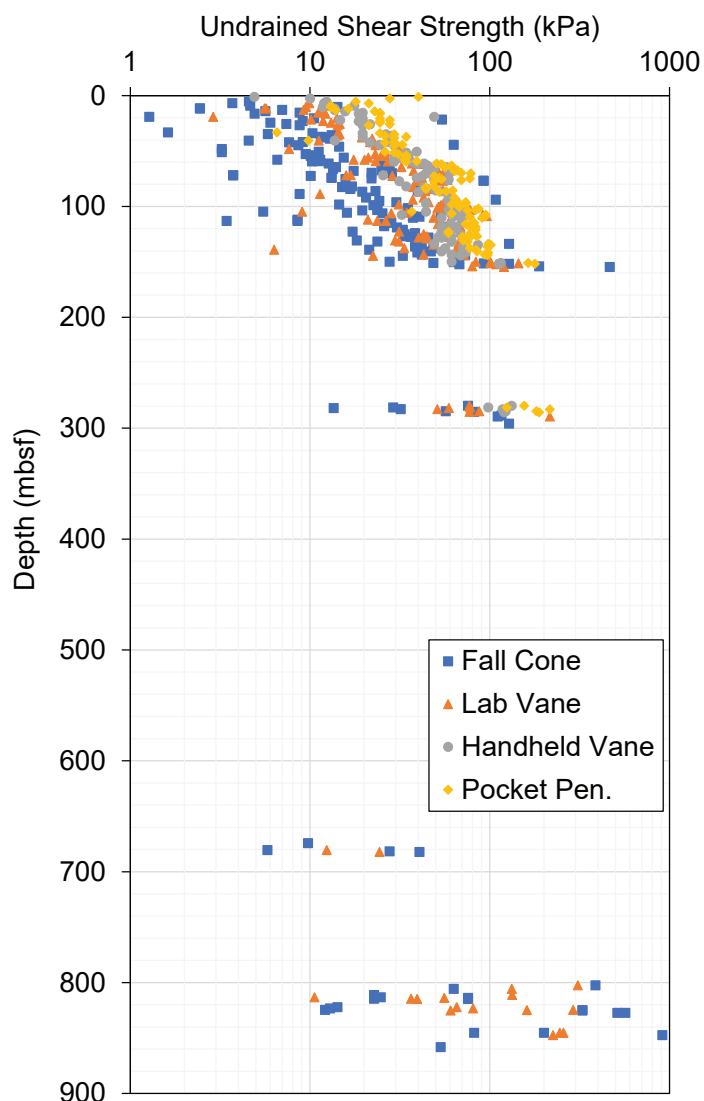


Figure F40: Undrained shear strength measurements using compressed depths. A pocket penetrometer (Pen.) and a handheld vane shear were deployed offshore. A lab vane and fall cone were deployed onshore. Geotek Advanced Piston Corer (G-APC) coring ended at 153 mbsf (Core H002-25H).

typical value for silty clay mixtures. The porosity is not corrected for salinity.

Figure F41 plots moisture and density data from benchtop experiments conducted on discrete plug samples from the split core working halves and both discrete plug and wedge samples from the moisture and density whole rounds. Figure F41 column D plots porosity calculated from the core density measurements assuming a grain density of 2.7 g/cc and 100% water saturation ($S = 100$). Both the density and the porosity trend with the LWD-derived data and variations are driven by the lithology as shown in Figure F27.

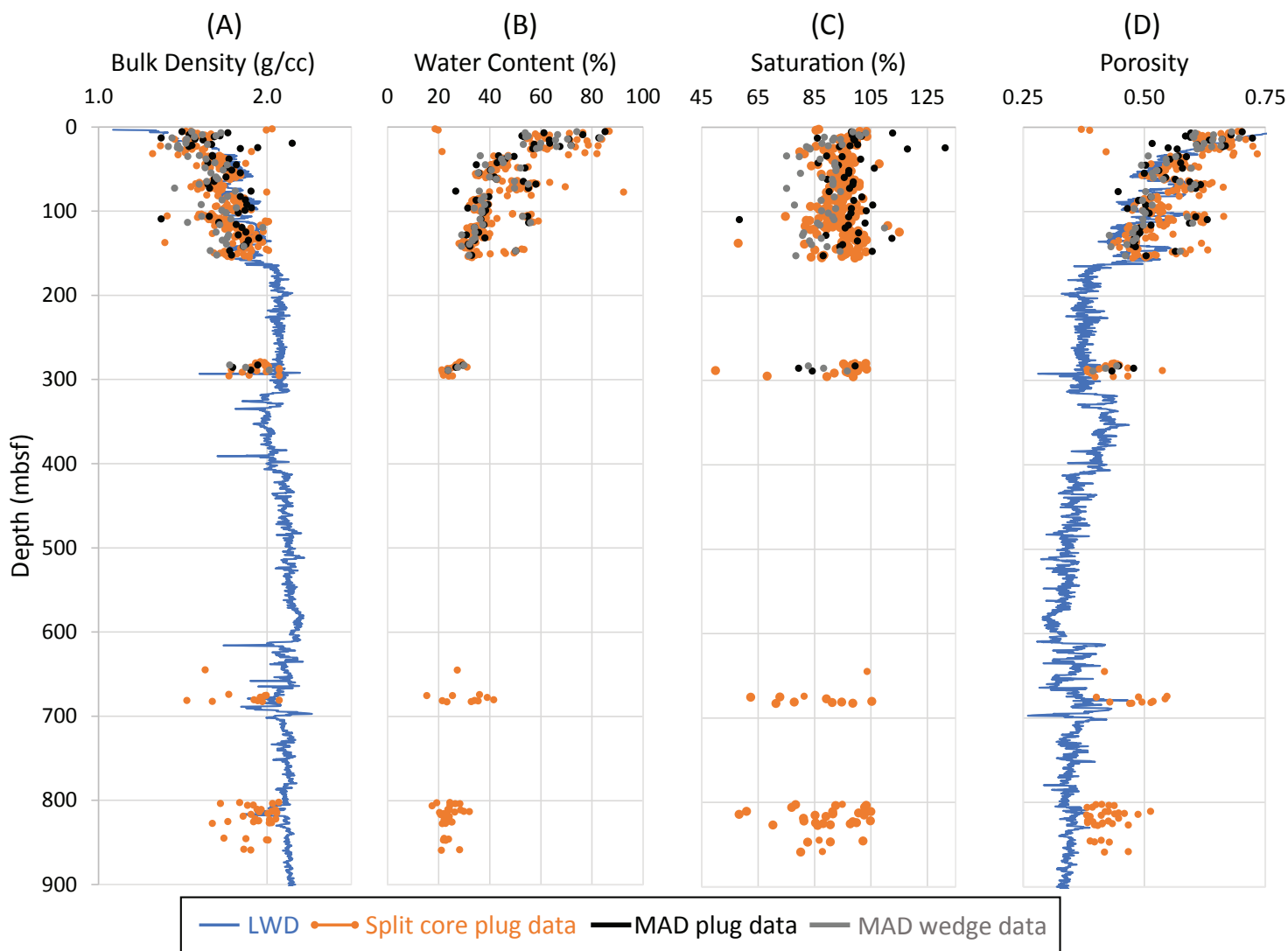


Figure F41: Measured core A) Bulk density, B) Water content, C) Water saturation, and D) Porosity using compressed depth. Data from discrete split core plugs are shown as orange circles. Data from discrete plugs taken from moisture and density whole round (sample code MAD) are shown as black circles. Data from wedges collected from the MAD whole rounds are shown as gray circles. All samples used an assumed grain density of 2.7 g/cm³, but porosity is not corrected for salinity. Logging while drilling (LWD) data are shown as a blue line. Data was projected to equivalent stratigraphic depths (See [Correlation of Hole H001 log data to Site H core data](#)). The porosity from the LWD data was calculated assuming a fluid density of 1.038 g/cc and a solid density of 2.65 g/cc within sands and 2.70 g/cc within muds. (See [Moisture and Density Measurements](#).)

Dissolved methane concentrations and hydrate saturation

Quantitative measurement of the volume of gas and liquid produced during the stepwise depressurization of pressure cores to atmospheric pressure (quantitative degassing) was conducted on 22 pressure core sections. All quantitative degassing on samples from 0-296.4 mbsf (Hole H003) were performed on mud-rich material. All quantitative degassing on samples from 644.6-859.6 mbsf (Hole H002) were performed on cores from the bounding

muds of the Upper Blue and Orange sands. One sample contained a transition from clay to sand rich layers of the Upper Blue sand at 675.13-675.33 mbsf (Section H002-2FB-4).

Hydrocarbon gases produced during quantitative degassing were analyzed (See [Gas Geochemistry](#)) and found to all be > 99.99% methane. The total volume of gas produced (including atmospheric contamination) was used to determine the in-situ concentration of dissolved methane in the pore water, the presence of methane hydrate, and the saturation of the pore space with methane hydrate.

Figure F42 illustrates the difference in the total volume of methane produced for three samples, one where the dissolved methane concentration of the pore water was below saturation (thus without methane hydrate, Figure F42, Section H003-24CS-2 brown circles) and two where the dissolved methane concentration of the pore water was saturated and the core contained methane hydrate (Figure F42, Section H003-29CS-3 orange diamonds and Section H002-02FB-4 blue triangles).

During depressurization of the unsaturated sample, Section H003-24CS-2, the change in total volume of methane as the pressure was decreased was initially driven by water displacement by gas under pressure and finally by gas displacement as methane solubility decreased. Only 1.66 L of methane was produced from a 94-cm long section of pressure core.

When the pore water is saturated with methane and methane hydrate is present, as during the depressurization of Section H003-29CS-3, the change was similar except the total volume of methane approximately follows the hydrate stability boundary (about 6 MPa in this example) as hydrate dissociated into methane and water. From this sample, 4.28 L of methane was produced from a 65-cm long section of pressure core. A similar volume of methane was produced from the 20 cm section, Section H002-02FB-4, due to its higher hydrate saturation.

Once the total volume of methane produced from a sample is known, the concentration of methane present or methane hydrate saturation was calculated based on the volume of the sample, a calculated porosity, a typical hydrate stoichiometry, and a typical hydrate density. If the total amount of methane present was less than the in-situ maximum solubility of methane in water, then the sample did not contain methane hydrate, and the dissolved methane concentration was calculated. If the total amount of methane was greater than the in-situ maximum solubility of methane in water, the consequent hydrate saturation of the pore space was calculated based on the amount of methane in excess of the solubility limit.

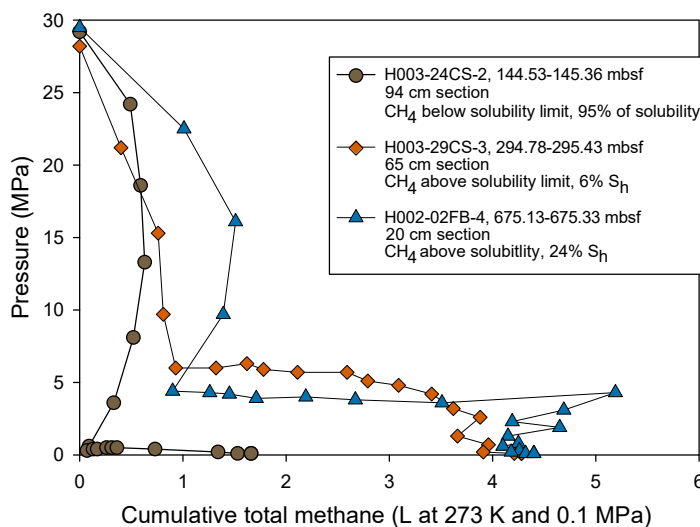


Figure F42: Example quantitative degassing results: Cumulative total volume of methane (CH_4) (including total methane expelled and remaining in the core storage chamber) produced from a pressure core as the pressure is decreased in steps for three samples. The brown circles show a long (94 cm) unsaturated sample (dissolve methane concentration is less than 100% and there is no hydrate, Section H003-24CS-2). The orange diamonds show a shorter (65 cm) saturated sample with a small amount of methane hydrate (dissolve methane concentration is 100% and the methane hydrate concentration was 6% of the pore space, Section H003-29CS-3). The blue triangles show and even shorter (20 cm) saturated sample with a higher concentration of methane hydrate (dissolve methane concentration is 100% and the average methane hydrate concentration in the pore space was 24%, but with most of the hydrate residing in only at one end, Section H002-02FB-4). Decreases in total methane are not real but artifacts introduced when accounting for the change in volume of equipment as the pressure decreases.

Dissolved methane concentration was observed to increase with depth and reaches 100% saturation at 146.6-147.5 mbsf (Section H003-24CS-5). In the muds bounding the Red sand interval, 287.1 to 296.4 mbsf (Cores H003-27CS, -28CS, and -29CS), methane hydrate exists in small saturations of ~1 to 6% (Figure F43).

Section H002-02FB-4 (675.13-675.33 mbsf) represents a transition from the bounding clay to a hydrate-bearing sand bed associated with the Upper Blue sand, as shown by an increase in core P-wave velocity in the lower part of the sample. The bulk hydrate saturation of this sample is 24.4%. The hydrate saturation of the sand is higher than the bulk saturation. In a section of mud 2 m below (677.4-677.7 mbsf, Section H002-03CF-2), the dissolved methane concentration is 72% of solubility (Figure F43).

Three sections were degassed in the interval 802.0-805.7 mbsf, which is within the seal of the Orange sand (Sections H002-05CS-3, -06CS-2, and -06CS-5). Sections H002-05CS-3 and H002-06CS-2 have methane concentrations of 94% and 83% of methane solubility, respectively. Section H002-06CS-5 was fully saturated with dissolved methane, but with a methane hydrate saturation of less than 1 of the pore space%. A clay-rich interval of the Orange sand was also characterized (810.8-811.3 mbsf, Section H002-08CS-3). It was also fully saturated with dissolved methane, but with a methane hydrate saturation of less than 1%.

Microbiology

Samples were collected to investigate microbial communities in recovered sediments from both coarse- and fine-grained materials, where hydrates occur and where they are absent, and from below the hydrate-bearing sediments (below the BSRs). Using these samples, the following will be determined:

1. Deoxyribonucleic acid (DNA) based microbial community diversity and genetic/functional capacity of single microbial cells (Oregon State University)
2. Complex organic matter degradation capacity (University of South Alabama)
3. Calcium carbonate-precipitating capacity of microbial cells (The University of Texas of Austin)
4. Presence and type of foraminifera as well as visual evidence of carbonates or sulfides (USGS)
5. Presence of heterotrophic organisms (University of Chicago)
6. Microbial cell counts (JAMSTEC)

All samples collected for these microbiological determinations were obtained from samples adjacent to other measurements or core samples acquired for pore water geochemistry, sediment texture, hydrate analysis, and geophysical properties. Throughout the expedition, control samples were collected to assess the degree of drilling fluid contamination in the cores, if any, and the potential for lab-based contamination from confining waters and lab airborne contaminants.

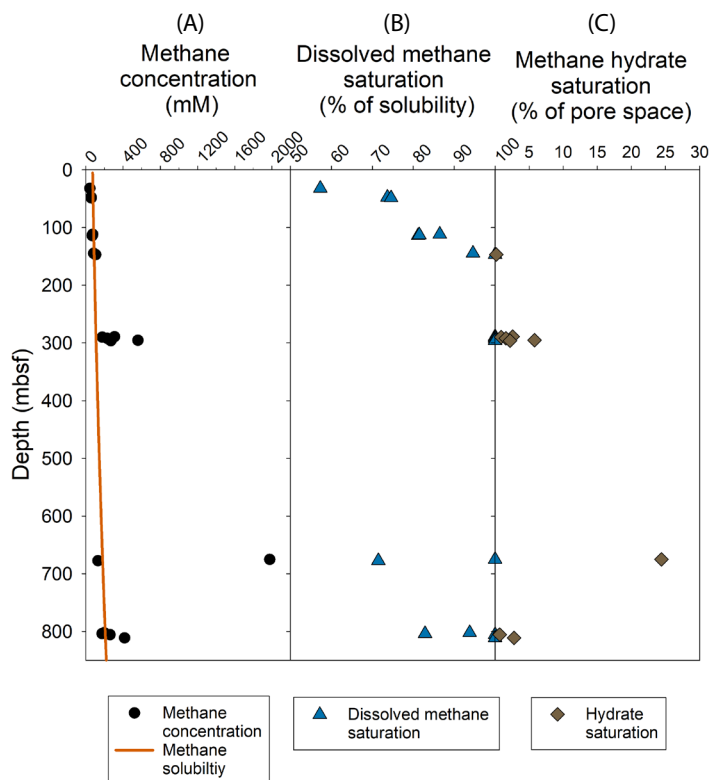


Figure F43: Downhole dissolved methane concentration using compressed depths. A) Dissolved methane concentration (mM) with depth (black dots) with calculated maximum methane solubility (burnt orange line); B) Dissolved methane as a percent of the methane solubility limit (blue triangles); C) Methane hydrate saturation as a percentage of the pore space (brown diamonds).

A subset of extracted DNA samples was submitted for 16S ribosomal DNA sequencing. These samples originated from GOM2-2 sub-cored sediments acquired from several depths and from selected contamination controls (i.e., drilling mud, lab air, PCATS fluid), and lab blanks. The sequencing data will be used as a preliminary assessment of sediment community characteristics and potential sources of contamination.

Geochemistry

Figures [F44](#) and [F45](#) summarize many of the geochemical measurements made to date. Geochemical analyses were carried out to characterize the pore water squeezed from pore water whole rounds; gases collected during pressure core depressurization and collected from voids; and sediments from pore water whole rounds.

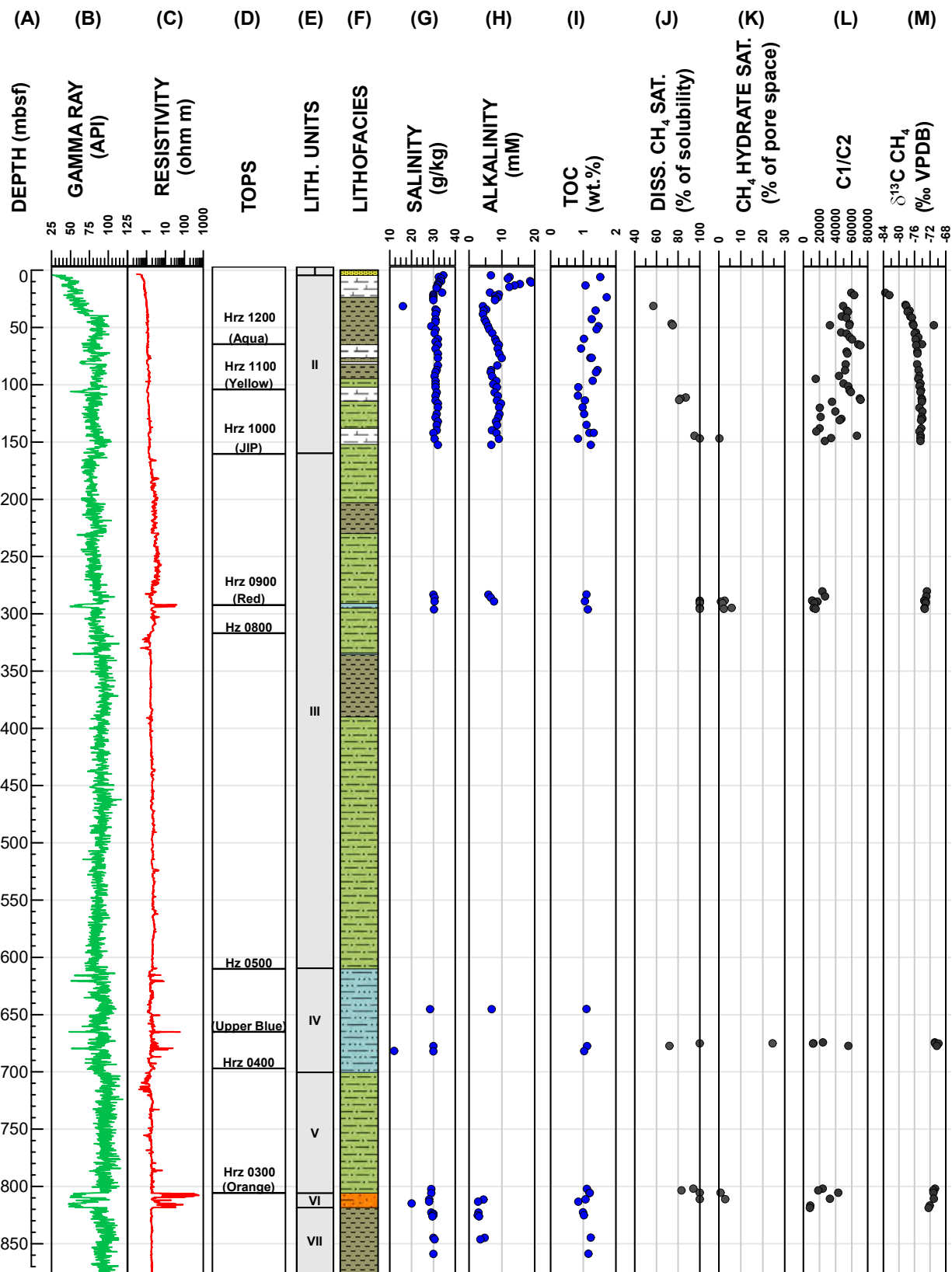


Figure F44: Geochemistry summary at Site H. A) Depth in meters below the seafloor (mbsf); B) Logging while drilling (LWD) gamma ray in green; C) LWD resistivity in red; D) Seismic horizons (Hrz) and stratigraphic tops as described in Table T10; E) Lithologic Units; F) Lithofacies (Table T12); G) Uncorrected salinity (See [Pore water geochemistry](#)); H) Uncorrected alkalinity (See [Pore water geochemistry](#)); I) Total organic carbon (TOC, see [Sediment geochemistry](#)); J) Dissolved methane saturation as a percent of solubility; K) Methane hydrate saturation of the pore space (See [Dissolved methane concentrations and hydrate saturation](#)); L) Methane to ethane (C₁:C₂) ratio, M) Carbon-13 isotopes (δ¹³C) of methane (CH₄) measured post-expedition using a cavity ringdown spectrometer, CRDS. (See [Sediment geochemistry](#).) G-M use compressed depths. The depth projection of Hole H001 LWD data onto Hole H002 and Hole H003, used in columns, B, C, and D, is discussed in [Correlation of Hole H001 log data to Site H core data](#).

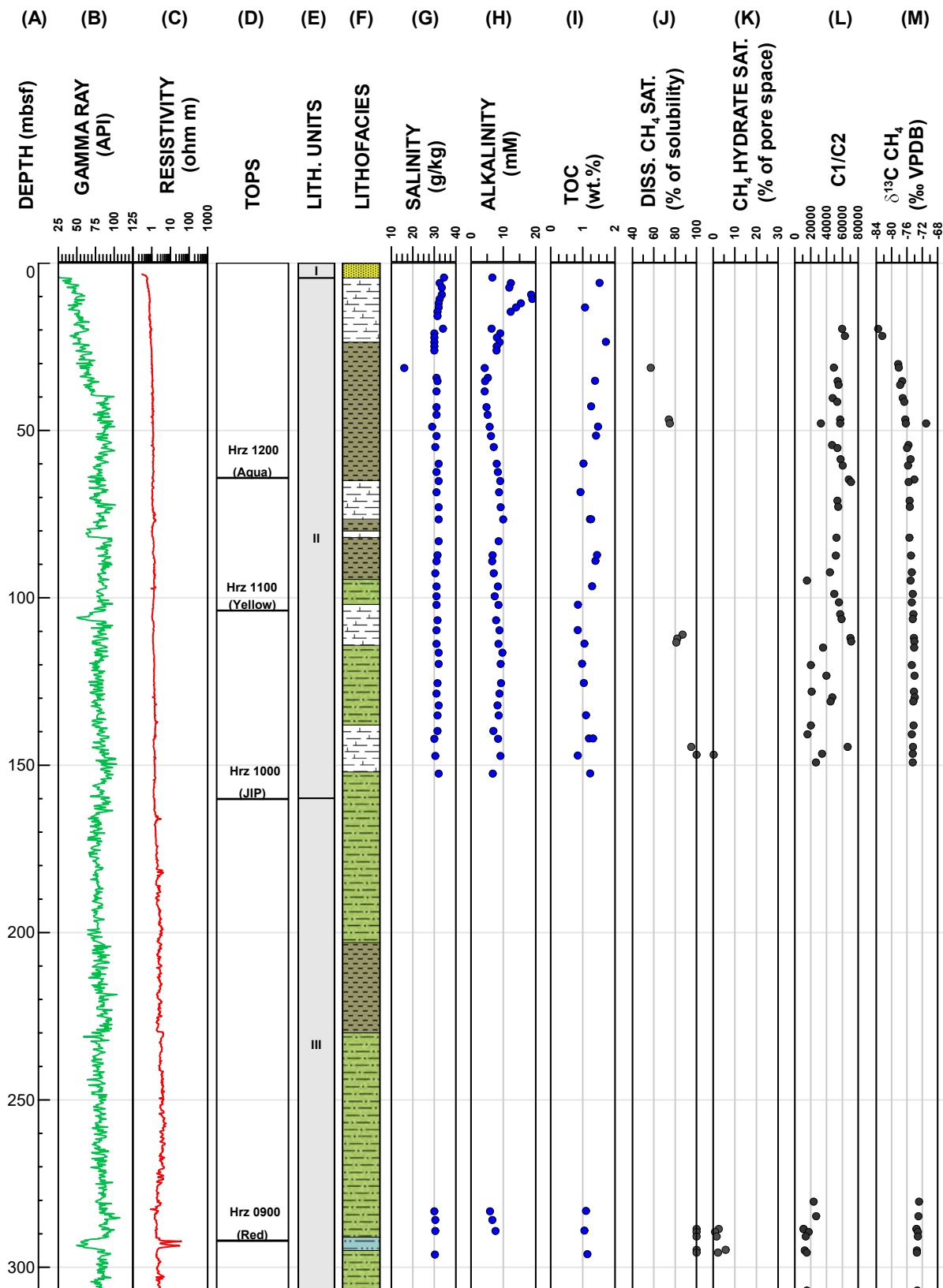


Figure F45: Expanded view of the Geochemistry Summary 0-300 mbsf. A) Depth in meters below the seafloor (mbsf); B) Logging while drilling (LWD) gamma ray in green; C) LWD resistivity in red; D) Seismic horizons (Hrz) and stratigraphic tops as described in Table T10; E) Lithologic Units; F) Lithofacies (Table T12); G) Uncorrected salinity (See [Pore water geochemistry](#)); H) Uncorrected alkalinity (See [Pore water geochemistry](#)); I) Total organic carbon (TOC, See [Sediment geochemistry](#)); J) Dissolved methane saturation as a percent of solubility; K) Methane hydrate saturation of the pore space (See [Dissolved methane concentrations and hydrate saturation](#)); L) Methane to ethane (C₁:C₂) ratio, M) Carbon-13 isotopes ($\delta^{13}\text{C}$) of methane (CH₄) measured post-expedition using a cavity ringdown spectrometer, CRDS. (See [Sediment geochemistry](#).) G-M use compressed depths. The depth projection of Hole H001 LWD data onto Hole H002 and Hole H003, used in columns, B, C, and D, is discussed in [Correlation of Hole H001 log data to Site H core data](#).

Pore water geochemistry

Pore water samples were squeezed from whole rounds and the salinity and alkalinity were measured on the vessel. Seventy-two routine pore water whole-round (sample code routine interstitial water or IWR) samples were collected and squeezed for shipboard and shore-based chemical analyses. Forty-six non-routine organic whole-round (sample code organic interstitial water or IWO) samples were collected from G-APC cores, immediately adjacent to the IWR whole-rounds, and squeezed for shore-based analysis of trace metal concentrations, trace metal isotope ratios, dissolved organic carbon characterization, dissolved sulfide concentrations, and sulfate concentrations.

The initial salinity and alkalinity data are presented in Figure [F46](#) and are not corrected for drilling or PCATS contamination. Salinity is expressed using a standard from the International Association for the Physical Sciences of the Oceans and is unitless. Samples of drilling seawater, drilling mud, and PCATS fluid were collected and will be used to assess contamination at a later date.

Uncorrected salinity decreases from 34.5 at 4.35 mbsf to 30 at 21 mbsf (Top of Hole H003, Figure [F47](#), column A), then remains relatively constant to 296.4 mbsf (Hole H003 total depth) (Figures [F46](#) and [F47](#), column A). The low salinity value at 30.2 mbsf (Core H003-05CS) likely reflects contamination with PCATS fluid prior to whole-round sampling in the core receiving laboratory and will be confirmed by shore-based cesium concentration analyses. Background salinity ranges from 28 to 30.5 from 644.6-859.6 mbsf (Hole H002, Figure [F46](#), column A). The two distinct salinity anomalies at 681.6 and 814.9 mbsf (Core H002-04FB-2 and -09CS-4) suggest the freshening of pore water from the dissociation of methane hydrate at relatively high saturations.

The pore water alkalinity profile is Z-shaped in the upper 10 mbsf (Figure [F47](#), column B) with a sharp increase to a peak of 12.3 mM at 6 mbsf, then a decrease to 11.8 mM at 7.3 mbsf, then a sharp increase to a maximum concentration of 18.6 mM at

9.5 mbsf. Below this depth, alkalinity decreases to a concentration of 4.2 mM at 31 mbsf, and increases more gradually to the third concentration maxima of 9.9 mM at 76.6 mbsf. Alkalinity concentrations again decrease sharply below the third concentration maxima to 6.7 mM at 87.3 mbsf.

Below this depth, alkalinity concentrations are variable but do not exhibit sharp increases or decreases to 297 mbsf, with concentrations ranging between 5.9 and 9.7 mM. The reason for the changes in alkalinity concentrations in the upper sediment column will be one of the major focuses of the shore-based pore water geochemistry program. Alkalinity concentrations 644.6-861.3 mbsf (Hole H002, Figure [F46](#), column B) range from 2.6 mM to 6.8 mM, with the lowest measured concentrations between 813 mbsf - 825 mbsf and the highest concentration at 645 mbsf.

Gas geochemistry

Gas samples from voids inside the core liner were extracted into syringes and gas bags. Void gases in syringes were measured onboard via gas chromatography with a thermal conductivity detector (GC-TCD) within hours of collection. Void gases could only be collected on conventional cores.

Pressure core gas samples were also collected during depressurization in syringes and a subset in gas bags. Syringe samples were measured onboard via GC-TCD within hours of collection. Intact gas hydrate was discovered while splitting three cryo-frozen core sections. Dissociated hydrate gas samples from this gas hydrate were only collected in gas bags. Bagged samples were measured post-expedition on a higher sensitivity gas chromatograph with a Flame Ionization Detector (GC-FID) in line with a Cavity Ring-Down Spectrometer (CRDS) to measure the $\delta^{13}\text{C}$ isotopic ratio of carbon.

Methane (C_1)/ethane (C_2) and $\text{C}_1/(\text{C}_2+\text{C}_3)$ decrease with depth, mainly driven by the increase in ethane with depth (Figure [F48](#)). Ethane is present only in trace amounts (9 to 114 ppm) in all samples. Most samples contain trace propane (< 9 ppm) and fewer contain i-butane or n-butane (< 4 ppm). This trend exists in

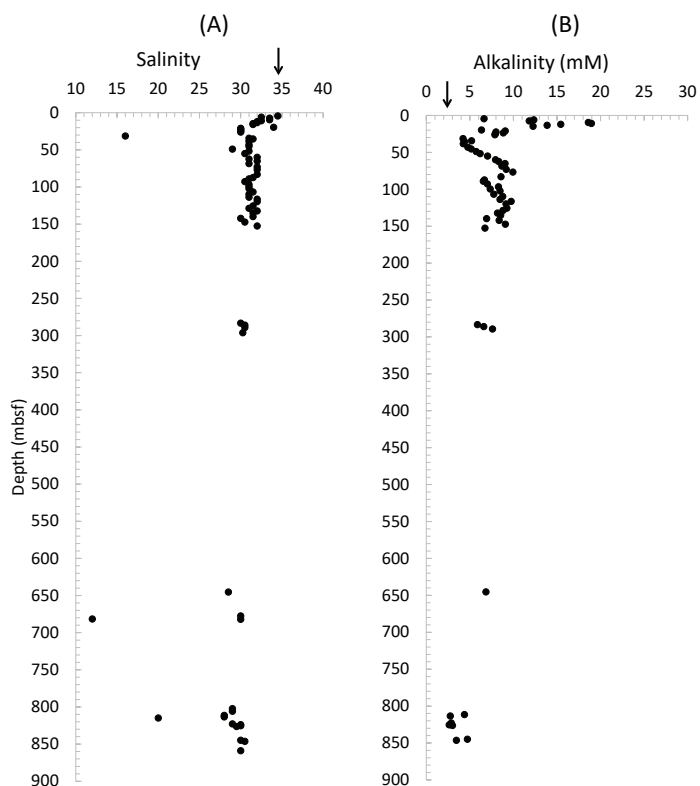


Figure F46: Uncorrected concentration profiles of A) Salinity and B) Alkalinity using compressed depths (0–900 mbsf). Arrows indicate seawater values. All measured concentrations will be corrected for contamination in the future. Salinity is expressed using a standard from the International Association for the Physical Sciences of the Oceans and is unitless.

both the GC-TCD (Figure F48, right-most column, syringe samples) and CRDS-GC-FID measurements (F48, middle columns, bagged samples). All values of C_1/C_2 and $C_1/(C_2+C_3)$ are relatively high (>1000). $\delta^{13}\text{C}-\text{CH}_4$ (Figure F48, left-most column) increases with depth, but all values are lighter than -69.3‰ Vienna Pee Dee Belemnite (VPDB) (mean: -73.9‰ VPDB). The decrease in C_1/C_2 and increase in $\delta^{13}\text{C}-\text{CH}_4$ is most apparent in the continuously cored section (0-155.1 mbsf) but the values near the Red sand (~280-300 mbsf) and through the Upper Blue sand unit (about 674-678 mbsf) are consistent with the overall trend of the shallower sediments. The highest variability was observed in the cores through the Orange sand interval (about 800-820 mbsf). It is unclear at this point whether there is a trend throughout this interval. No gas samples have yet been collected from quantitative degassing of the high-saturation intervals.

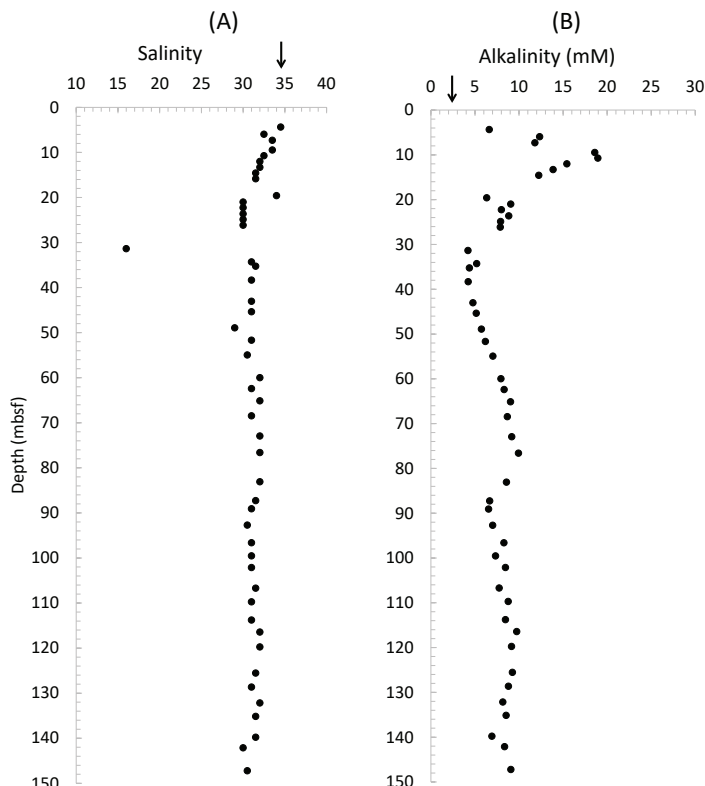


Figure F47: Expanded view of the uncorrected concentration profiles of A) Salinity and B) Alkalinity using compressed depths (0–150 mbsf).

Overall, the gas composition of light $\delta^{13}\text{C}-\text{CH}_4$ and high $C_1/(C_2+C_3)$ is consistent with a mainly microbial source of methane with only very minor thermogenic components. Future gas chemistry analyses will be necessary to determine the specific methanogenesis pathways, possible secondary methane generation, or the possible presence of microbial ethane.

Sediment geochemistry

Elemental analysis of bulk sediment from pore water whole round squeeze cakes ($n=36$) were completed (Figures F49 and F50).

Total organic carbon (TOC) measurements 0-296.4 mbsf (Hole H003) vary between 0.84 wt.% and 1.72 wt.% (Figure F49, column A). The variation in the TOC content is driven largely by the relative contributions and dilution effects of pelagic versus hemipelagic sedimentation. TOC measurements 644.6-859.6 (Hole H002) are noticeably less and vary between 0.85 wt.% and 1.29 wt.%, with a mean of 1.09 wt.% ($1\sigma = 0.11$ wt.%). Total nitrogen (TN) was measured. TOC/TN

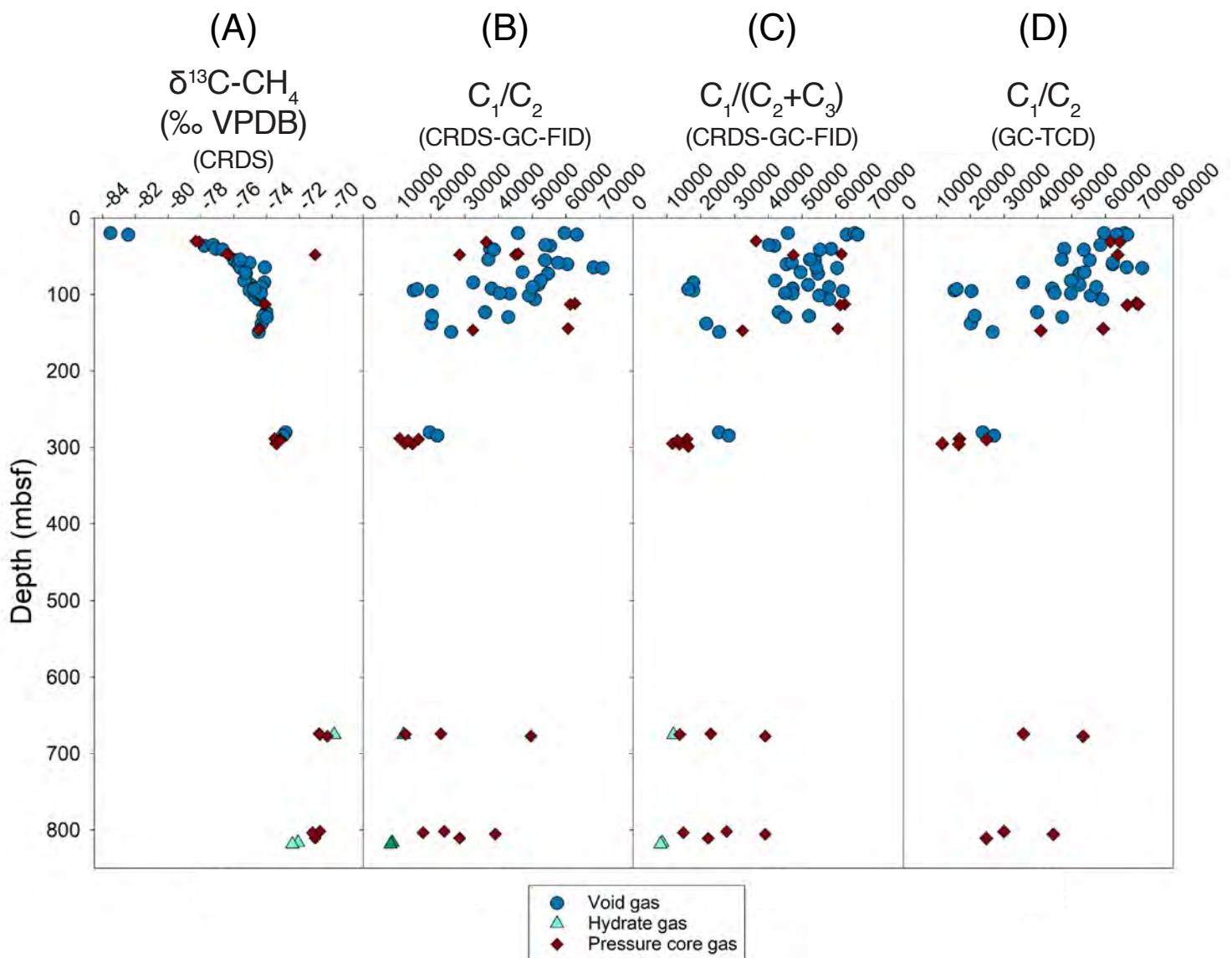


Figure F48: Carbon-13 isotopes ($\delta^{13}\text{C}$) of methane (CH_4) and molecular ratios for void, pressure core, and hydrate gases from Hole H003 and Hole H002. A) $\delta^{13}\text{C}-\text{CH}_4$ measured post-expedition using a Cavity Ring-Down Spectrometer (CRDS); B) Methane (C_1)/ethane (C_2) measured post-expedition using higher-sensitivity gas chromatography with a Flame Ionization Detector (GC-FID) in line with a CRDS; C) $\text{C}_1/(\text{C}_2+\text{C}_3)$ measured post-expedition using GC-FID in line with a CRDS; D) C_1/C_2 measured onboard within hours of collection using gas chromatography with a thermal conductivity detector (GC-TCD). Results are plotted using compressed depths.

(Figure F49, column B) documents a mixed TOC origin from both terrestrial and marine organic carbon.

CaCO_3 content was calculated by multiplying inorganic carbon (IC) weight percentages ($\text{IC} = \text{TC}-\text{TOC}$) by 8.33 to account for the non-carbon mass fraction. The CaCO_3 content 0-296.4 mbsf (Hole H003) is generally high and variable, with a range of 1.50 to 26.82 wt.% (Figure F49, column C). The CaCO_3 content 644.6-859.6 (Hole H002) is moderately high and variable, with a range of 0.00 to 20.66 wt.%. The presence and amounts of CaCO_3 are consistent with

detrital carbonate lithic fragments, foraminifera, and calcareous nannofossils observed in smear slides.

Total Sulfur (TS) measurements 0-296.4 mbsf (Hole H003) are variable, with a range of 0.07 wt.% to 3.14 wt.% (Figure F49, column D). Intervals of elevated TS relative to a low background level may be diagnostic of sulfides produced via anaerobic oxidation of methane (AOM) (Borowski et al., 2013; Peketi et al., 2012). Cyclic variation in TS in the upper 150 m also appears to be anticorrelated with magnetic susceptibility, suggesting AOM influenced diagenesis

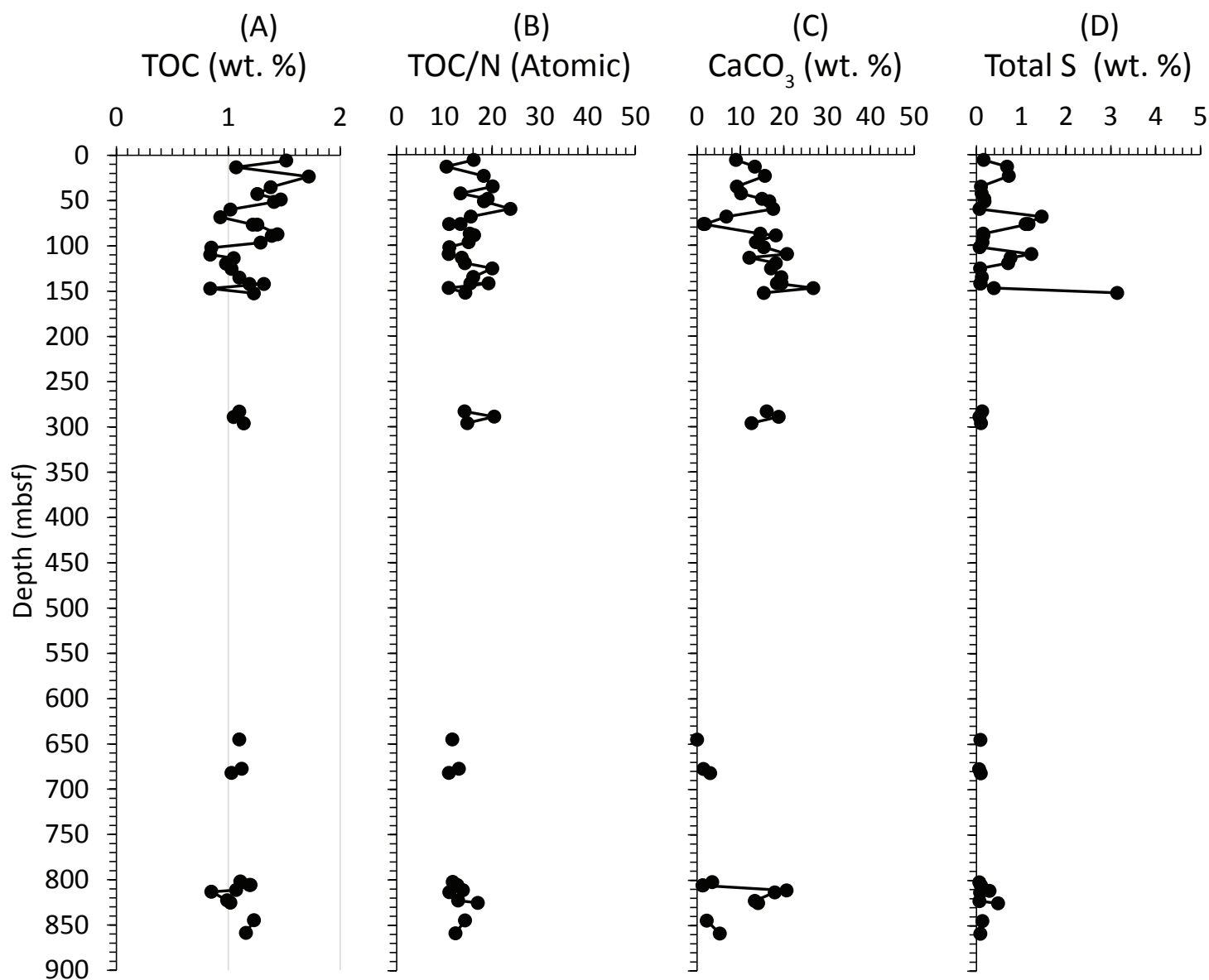


Figure F49: Initial downhole carbon, nitrogen, and sulfur (CNS) element analysis results using compressed depths. A) Total organic carbon (TOC), B) Atomic ratio of total organic carbon to total nitrogen (TOC/TN), C) Calcium carbonate (CaCO_3), and D) Total sulfur (TS).

in this interval (Johnson et al., 2021). AOM diagenetic overprints occurred in the presence of pore water sulfate and methane and thus occurred during early diagenesis, prior to compaction/dewatering. TS measurements 644.6-859.6 mbsf (Hole H002) are lower and less variable ranging from 0.06 wt.% to 0.48 wt.%. The lack of intervals with elevated TS suggested organoclastic sulfate reduction (OSR) is the dominant pathway for sulfide mineralization.

Measured TS/TOC (Figure F50, black dots) is compared to values of typical marine sediments and phytoplankton. Intervals of elevated TS (relative to TOC) above the typical marine sediment (Berner

and Raiswell, 1983) (Figure F50, solid black line) are consistent with the occurrence of early, AOM related, diagenesis in the sediments. TS data points (relative to TOC) below typical marine sediments and close to the marine phytoplankton end member line (Suits and Arthur, 2000) (Figure F50, dashed black line), suggest a dominance of OSR for these sediment samples.

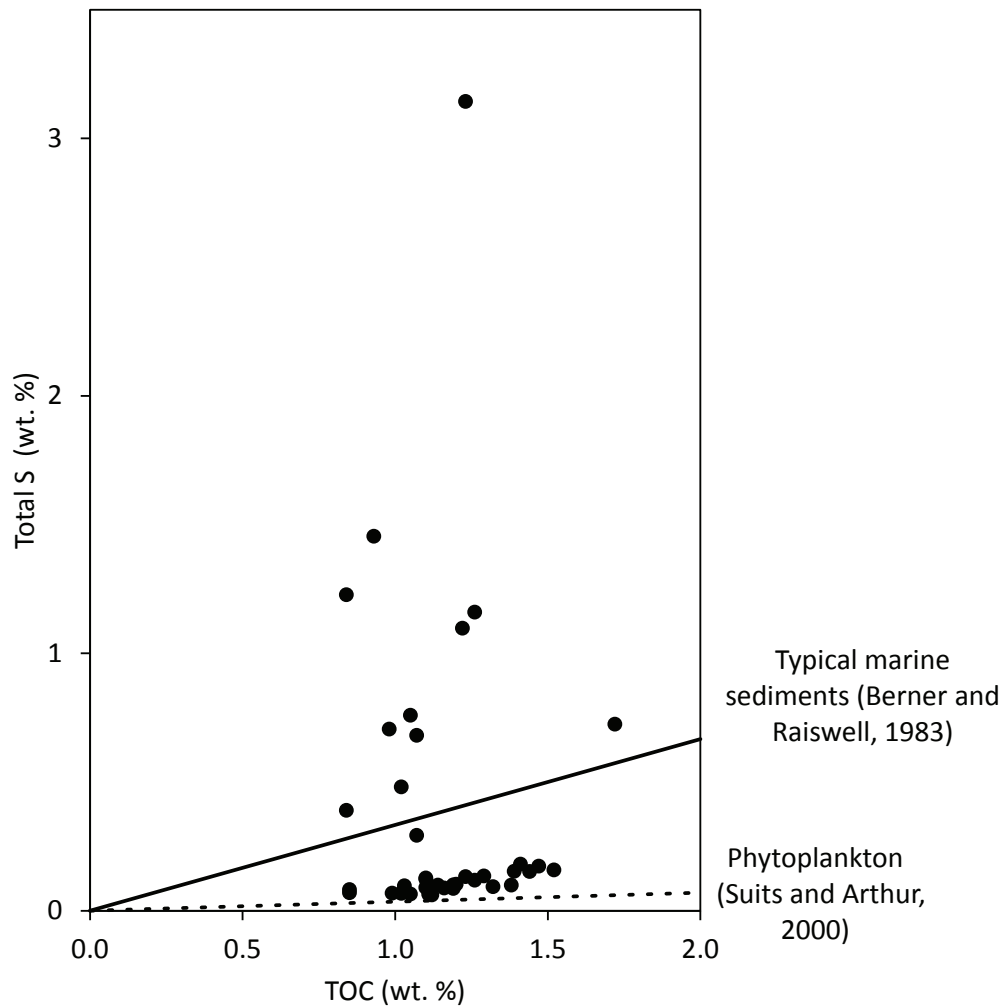


Figure F50: Total sulfur (TS) vs total organic carbon (TOC) cross-plot. The solid black line expresses the typical marine sediment ratio expected to be produced by organoclastic sulfate reduction (OSR) (Berner and Raiswell, [1983](#)). The dashed black line is the phytoplankton end member TS/TOC relationship of Suits and Arthur ([2000](#)).

References

- Archie, G. E., 1942, The Electrical Resistivity Log as an Aid in Determining Some Reservoir Characteristics, Transactions of AIME, Volume 146, p. 4, <https://doi.org/10.2118/942054-g>.
- ASTM International, 2017, ASTM D2487-17e1: Standard Practice for Classification of Soils for Engineering Purposes (Unified Soil Classification System): ASTM International, <https://doi.org/10.1520/D2487-17E01>.
- Berner, R. A., and Raiswell, R., 1983, Burial of organic carbon and pyrite sulfur in sediments over phanerozoic time: a new theory: *Geochimica et Cosmochimica Acta*, v. 47, no. 5, p. 855-862, [https://doi.org/10.1016/0016-7037\(83\)90151-5](https://doi.org/10.1016/0016-7037(83)90151-5).
- Bhandari, A. R., Cardona, A., Flemings, P. B., and Germaine, J. T., 2024, The geomechanical response of the Gulf of Mexico Green Canyon 955 reservoir to gas hydrate dissociation: A model based on sediment properties with and without gas hydrate: *Marine and Petroleum Geology*, v. 167, p. 107000, <https://doi.org/10.1016/j.marpetgeo.2024.107000>.
- Bhati, A., Kar, A., and Bahadur, V., 2024, Analysis of CO₂ hydrate formation from flue gas mixtures in a bubble column reactor: *Separation and Purification Technology*, v. 330, <https://doi.org/10.1016/j.seppur.2023.125261>.
- Biaostoch, A., Treude, T., Rüpke, L. H., Riebesell, U., Roth, C., Burwicz, E. B., Park, W., Latif, M., Böning, C. W., Madec, G., and Wallmann, K., 2011, Rising Arctic Ocean temperatures cause gas hydrate destabilization and ocean acidification: *Geophysical Research Letters*, v. 38, no. 8, p. L08602, <https://doi.org/10.1029/2011GL047222>.
- Borowski, W. S., Rodriguez, N. M., Paull, C. K., and Ussler, W., 2013, Are 34S-enriched authigenic sulfide minerals a proxy for elevated methane flux and gas hydrates in the geologic record?: *Marine and Petroleum Geology*, v. 43, p. 381-395, <https://doi.org/10.1016/j.marpetgeo.2012.12.009>.
- Boswell, R., 2009, Is gas hydrate energy within reach?: *Science*, v. 325, no. 5943, p. 957-958, <https://doi.org/10.1126/science.1175074>.
- Boswell, R., and Collett, T. S., 2011, Current perspectives on gas hydrate resources: *Energy & Environmental Science*, v. 4, no. 4, p. 1206-1215, <https://doi.org/10.1039/C0EE00203H>.
- Boswell, R., Collett, T. S., Frye, M., Shedd, W., McConnell, D. R., and Shelander, D., 2012a, Subsurface gas hydrates in the northern Gulf of Mexico: *Marine and Petroleum Geology*, v. 34, no. 1, p. 4-30, <https://doi.org/10.1016/j.marpetgeo.2011.10.003>.
- Boswell, R., Frye, M., Shelander, D., Shedd, W., McConnell, D. R., and Cook, A., 2012b, Architecture of gas-hydrate-bearing sands from Walker Ridge 313, Green Canyon 955, and Alaminos Canyon 21: Northern deepwater Gulf of Mexico: *Marine and Petroleum Geology*, v. 34, no. 1, p. 134-149, <https://doi.org/10.1016/j.marpetgeo.2011.08.010>.
- Boswell, R., Shipp, C., Reichel, T., Shelander, D., Saeki, T., Frye, M., Shedd, W., Collett, T. S., and McConnell, D. R., 2016, Prospecting for marine gas hydrate resources: Interpretation, v. 4, no. 1, p. SA13-SA24, <https://doi.org/10.1190/int-2015-0036.1>.
- Boswell, R., Schoderbek, D., Collett, T. S., Ohtsuki, S., White, M., and Anderson, B. J., 2017, The Iñik Sikumi Field Experiment, Alaska North Slope: Design, Operations, and Implications for CO₂-CH₄ Exchange in Gas Hydrate Reservoirs: *Energy & Fuels*, v. 31, no. 1, p. 140-153, <https://doi.org/10.1021/acs.energyfuels.6b01909>.
- Boswell, R., Myshakin, E., Moridis, G., Konno, Y., Collett, T. S., Reagan, M., Ajayi, T., and Seol, Y., 2019a, India National Gas Hydrate Program Expedition 02 summary of scientific results: Numerical simulation of reservoir response to depressurization: *Marine and Petroleum Geology*, v. 108, p. 154-166, <https://doi.org/https://doi.org/10.1016/j.marpetgeo.2018.09.026>.
- Boswell, R., Yoneda, J., and Waite, W. F., 2019b, India National Gas Hydrate Program Expedition 02 summary of scientific results: Evaluation of natural gas-hydrate-bearing pressure cores: *Marine and Petroleum Geology*, v. 108, p. 143-153, <https://doi.org/10.1016/j.marpetgeo.2018.10.020>.
- Boswell, R., Hancock, S., Yamamoto, K., Collett, T., Pratap, M., and Lee, S.-R., 2020, 6 - Natural Gas Hydrates: Status of Potential as an Energy Resource, in Letcher, T. M., ed., *Future Energy (Third Edition)*, Elsevier, p. 111-131, <https://doi.org/10.1016/B978-0-08-102886-5.00006-2>.
- Boudreau, B. P., Luo, Y., Meysman, F. J. R., Middelburg, J. J., and Dickens, G. R., 2015, Gas hydrate dissociation prolongs acidification of the Anthropocene oceans: *Geophysical Research Letters*, v. 42, no. 21, <https://doi.org/10.1002/2015gl065779>.
- Boyer, T. P., Baranova, O. K., Coleman, C., Garcia, H. E., Grodsky, A., Locarnini, R. A., Mishonov, A. V., O'Brien, T. D., Paver, C. R., Reagan, J. R., Seidov, D., Smolyar, I. V., Weathers, K., and Zweng, M. M., 2018, World Ocean Database 2018, NOAA Atlas NESDIS 87: Silver Spring, MD, NOAA, <https://doi.org/10.7289/V5NZ85MT>.
- BSEE, 2024, BSEE Data Center, <https://www.data.bsee.gov/>.
- Cardona, A., Bhandari, A. R., Heidari, M., and Flemings, P. B., 2023, The Viscoplastic Behavior of Natural Hydrate-Bearing Sandy-Silts Under Uniaxial Strain Compression (K₀ Loading): *Journal of Geophysical Research: Solid Earth*, v. 128, no. 7, p. e2023JB026976, <https://doi.org/10.1029/2023JB026976>.

- Claypool, G. E., and Kvenvolden, K. A., 1983, Methane and Other Hydrocarbon Gases in Marine Sediment: Annual Review of Earth and Planetary Sciences, v. 11, no. Volume 11, 1983, p. 299-327, <https://doi.org/10.1146/annurev.ea.11.050183.001503>.
- Collett, T. S., Boswell, R., Frye, M., Shedd, W., Godfriaux, P., Dufrene, R., McConnell, D., Mrozewski, S., Guerin, G., Cook, A., Jones, E., and Roy, R., 2009, Gulf of Mexico Gas Hydrate Joint Industry Project Leg II: Operational Summary: Proceedings of the Drilling and Scientific Results of the 2009 Gulf of Mexico Gas Hydrate Joint Industry Project Leg II, p. 27, <https://netl.doe.gov/sites/default/files/netl-file/OpSum%5B1%5D.pdf>.
- Collett, T. S., Boswell, R., Frye, M., Shedd, W. W., Godfriaux, P. D., Dufrene, R. S., McConnell, D. R., Mrozewski, S., Guerin, G., Cook, A., Jones, E., and Roy, R., 2010, Gulf of Mexico Gas Hydrate Joint Industry Project Leg II: Logging-While-Drilling Operations and Challenges, Offshore Technology Conference, Offshore Technology Conference, <https://doi.org/10.4043/20452-ms>.
- Cook, A. E., Anderson, B. I., Malinverno, A., Mrozewski, S., and Goldberg, D. S., 2010, Electrical anisotropy due to gas hydrate-filled fractures: Geophysics, v. 75, no. 6, p. 13, <https://doi.org/10.1190/1.3506530>.
- Cook, A. E., Anderson, B. I., Rasmus, J., Sun, K., Li, Q., Collett, T. S., and Goldberg, D. S., 2012, Electrical anisotropy of gas hydrate-bearing sand reservoirs in the Gulf of Mexico: Marine and Petroleum Geology, v. 34, no. 1, p. 72-84, <https://doi.org/10.1016/j.marpetgeo.2011.09.003>.
- Cook, A. E., Goldberg, D. S., and Malinverno, A., 2014, Natural gas hydrates occupying fractures: A focus on non-vent sites on the Indian continental margin and the northern Gulf of Mexico: Marine and Petroleum Geology, v. 58, p. 278-291, <https://doi.org/10.1016/j.marpetgeo.2014.04.013>.
- Cook, A. E., and Waite, W. F., 2018, Archie's Saturation Exponent for Natural Gas Hydrate in Coarse-Grained Reservoirs, v. 123, no. 3, p. 2069-2089, <https://doi.org/10.1002/2017jb015138>.
- Darnell, K. N., Flemings, P. B., and DiCarlo, D., 2019, Nitrogen-Driven Chromatographic Separation During Gas Injection Into Hydrate-Bearing Sediments: Water Resources Research, <https://doi.org/10.1029/2018wr023414>.
- Diegel, F. A., Karlo, J. F., Schuster, D. C., Shoup, R. C., and Tauvers, P. R., 1995, Cenozoic structural evolution and tectono-stratigraphic framework of the northern Gulf coast continental margin, in Jackson, M. P. A., Roberts, D. G., and Snelson, S., eds., Salt tectonics: a global perspective: AAPG Memoir 65, p. 109-151, <https://doi.org/10.1306/M65604C6>.
- Eaton, B. A., 1969, Fracture gradient prediction and its application in oil field operations: Journal of Petroleum Technology, v. 21, no. 10, p. 1353-1360, <https://doi.org/10.2118/2163-PA>.
- Fang, Y., Flemings, P. B., Daigle, H., Phillips, S. C., Meazell, P. K., and You, K., 2020, Petrophysical properties of the Green Canyon Block 955 hydrate reservoir inferred from reconstituted sediments: Implications for hydrate formation and production: AAPG Bulletin, v. 104, no. 9, p. 1997-2028, <https://doi.org/10.1306/01062019165>.
- Flemings, P. B., Phillips, S. C., Pettigrew, T., and Green, T., 2016, GOM2 Pressure Coring Tool with Ball Valve (PCTB) Land Test Initial Report, https://ig.utexas.edu/wp-content/uploads/2019/06/GOM2_PCTB_Land_Test_Initial_Report.pdf.
- Flemings, P. B., Phillips, S. C., Collett, T. S., Cook, A. E., Boswell, R., and Scientists, U.-G.-E., 2018a, Proceedings of the UT-GOM2-1 Hydrate Pressure Coring Expedition: Austin, TX, University of Texas Institute for Geophysics, <https://doi.org/10.2172/1646019>.
- Flemings, P. B., Phillips, S. C., Collett, T. S., Cook, A. E., Boswell, R., and Scientists, U.-G.-E., 2018b, UT-GOM2-1 Hydrate Pressure Coring Expedition Hole GC 955 H002, in Flemings, P. B., Phillips, S. C., Collett, T. S., Cook, A. E., and Boswell, R., eds., Proceedings of the UT-GOM2-1 Hydrate Pressure Coring Expedition: Austin, TX, University of Texas Institute for Geophysics, <https://doi.org/10.2172/1648313>.
- Flemings, P. B., 2020, Phase 3 Report (Period ending 9/30/2019), Deepwater Methane Hydrate Characterization and Scientific Assessment, DOE Award No.: DE-FE0023919, <https://www.osti.gov/servlets/purl/1615748>.
- Flemings, P. B., Pettigrew, T., Houghton, J., Phillips, S. C., Price, A., Murphy, Z., Fang, Y., and Santra, M., 2020a, GOM2 Pressure Coring Tool with Ball Valve (PCTB) Land Test II Report, https://ig.utexas.edu/wp-content/uploads/2020/08/PCTB_Land_Test_II_Report_wAppendices.pdf.
- Flemings, P. B., Phillips, S. C., Boswell, R., Collett, T. S., Cook, A. E., Dong, T., Frye, M., Guerin, G., Goldberg, D. S., Holland, M., Jang, J., Meazell, K., Morrison, J., O'Connell, J., Pettigrew, T., Petrou, E., Polito, P. J., Portnov, A., Santra, M., Schultheiss, P. J., Seol, Y., Shedd, W., Solomon, E. A., Thomas, C. M., Waite, W. F., and You, K., 2020b, Pressure coring a Gulf of Mexico deep-water turbidite gas hydrate reservoir: Initial results from The University of Texas–Gulf of Mexico 2-1 (UT-GOM2-1) Hydrate Pressure Coring Expedition: AAPG Bulletin, v. 104, no. 9, p. 1847-1876, <https://doi.org/10.1306/05212019052>.
- Flemings, P. B., 2021a, Phase 4 Report (Period ending 9/30/2020), Deepwater Methane Hydrate Characterization and Scientific

- Assessment, DOE Award No.: DE-FE0023919, <https://www.osti.gov/servlets/purl/1768216>.
- Flemings, P. B., 2021b, A Concise Guide to Geopressure: Origin, Prediction, and Applications, Cambridge Press, <https://doi.org/10.1017/9781107326309>.
- Flemings, P. B., Cook, A. E., Collett, T., and Boswell, R., 2022, Gas hydrates in Green Canyon Block 955, deep-water Gulf of Mexico: Part II, Insights and future challenges: AAPG Bulletin, v. 106, no. 5, p. 937-947, <https://doi.org/10.1306/bltnintro030922>.
- Flemings, P. B., Thomas, C., Collett, T. S., Colwell, F., Cook, A. E., Germaine, J., Holland, M., Houghton, J., Johnson, J. E., Malinverno, A., Meazell, K., Pettigrew, T., Phillips, S. C., Portnov, A., Price, A., Santra, M., Schultheiss, P., Solomon, E., and You, K., 2023a, UT-GOM2-2 Prospectus: Science and Sample Distribution Plan V2.3, <https://doi.org/10.5281/zenodo.13694088>.
- Flemings, P. B., Cook, A. E., Houghton, J., Morrison, J., Portnov, A., Pettigrew, T., Phillips, S. C., Polito, P., Santra, M., and Thomas, C., 2023b, UT-GOM2-2 Operations Plan, https://ig.utexas.edu/wp-content/uploads/2023/06/OperationsPlan_Rev2.3.pdf.
- Fofonoff, N., and Millard, R., 1983, Algorithms for Computation of Fundamental Properties of Seawater: UNESCO Tech. Pap. Mar. Sci., v. 44, <https://doi.org/10.25607/OBP-1450>.
- Frye, M., Shedd, W., and Boswell, R., 2012, Gas hydrate resource potential in the Terrebonne Basin, Northern Gulf of Mexico: Marine and Petroleum Geology, v. 34, no. 1, p. 150-168, <https://doi.org/10.1016/j.marpetgeo.2011.08.001>.
- Gebregiorgis, D., Giosan, L., Hathorne, E. C., Anand, P., Nilsson-Kerr, K., Plass, A., Lückge, A., Clemens, S. C., and Frank, M., 2020, What Can We Learn From X-Ray Fluorescence Core Scanning Data? A Paleomonsoon Case Study: Geochemistry, Geophysics, Geosystems, v. 21, no. 2, <https://doi.org/10.1029/2019GC008414>.
- Goldberg, D. S., Kleinberg, R. L., Weinberger, J. L., Malinverno, A., McLellan, P. J., and Collett, T. S., 2010, 16. Evaluation of Natural Gas-Hydrate Systems Using Borehole Logs, Geophysical Characterization of Gas Hydrates, p. 239-261, <https://doi.org/10.1190/1.9781560802197.ch16>.
- Gradstein, F., Ogg, J., Schmitz, M., and Ogg, G., 2012, Geologic Time Scale 2012 -- 2 volume book, <https://www.sciencedirect.com/book/9780444594259/the-geologic-time-scale>.
- Guo, F., Clemens, S., Liu, X., Long, Y., Li, D., Tan, L., Liu, C., Yan, H., and Sun, Y., 2021, Application of XRF Scanning to Different Geological Archives: Earth and Space Science, v. 8, no. 9, <https://doi.org/10.1029/2020EA001589>.
- Hillman, J. I. T., Cook, A. E., Daigle, H., Nole, M., Malinverno, A., Meazell, K., and Flemings, P. B., 2017a, Gas hydrate reservoirs and gas migration mechanisms in the Terrebonne Basin, Gulf of Mexico: Marine and Petroleum Geology, v. 86, p. 1357-1373, <https://doi.org/10.1016/j.marpetgeo.2017.07.029>.
- Hillman, J. I. T., Cook, A. E., Sawyer, D. E., Küçük, H. M., and Goldberg, D. S., 2017b, The character and amplitude of 'discontinuous' bottom-simulating reflections in marine seismic data: Earth and Planetary Science Letters, v. 459, p. 157-169, <https://doi.org/10.1016/j.epsl.2016.10.058>.
- Hutchinson, D. R., Shelander, D., Dai, J., McConnell, D., Shedd, W., Frye, M., Ruppel, C., Boswell, R., Jones, E., Collett, T., Rose, K., Dugan, B., Wood, W., and Latham, T., Site Selection for DOE/JIP Gas Hydrate Drilling in the Northern Gulf of Mexico, in Proceedings 6th International Conference on Gas Hydrates (ICGH 2008), Vancouver, British Columbia, Canada, July 6-10 2008, https://netl.doe.gov/sites/default/files/2018-12/ICGH_5506_1_41330_0.pdf.
- IODP Depth Scale Task Force, 2011, IODP Depth Scale Terminology, <https://www.iodp.org/policies-and-guidelines/142-iodp-depth-scales-terminology-april-2011/file>.
- Isson, T. T., Planavsky, N. J., Coogan, L. A., Stewart, E. M., Ague, J. J., Bolton, E. W., Zhang, S., McKenzie, N. R., and Kump, L. R., 2020, Evolution of the Global Carbon Cycle and Climate Regulation on Earth: Global Biogeochemical Cycles, v. 34, no. 2, p. e2018GB006061, <https://doi.org/10.1029/2018GB006061>.
- Johnson, J. E., Phillips, S. C., Clyde, W. C., Giosan, L., and Torres, M. E., 2021, Isolating Detrital and Diagenetic Signals in Magnetic Susceptibility Records From Methane-Bearing Marine Sediments: Geochemistry, Geophysics, Geosystems, v. 22, no. 9, <https://doi.org/10.1029/2021gc009867>.
- Kayen, R. E., and Lee, H. J., 1991, Pleistocene slope instability of gas hydrate-laden sediment on the Beaufort margin: Marine Geotechnology, v. 10, <https://doi.org/10.1080/10641199109379886>.
- Kennett, J. P., Cannariato, K. G., Hendy, I. L., and Behl, R. J., 2000, Carbon Isotopic Evidence for Methane Hydrate Instability During Quaternary Interstadials: Science, v. 288, no. 5463, p. 128-133, <https://doi.org/10.1126/science.288.5463.128>.
- Kida, M., Jin, Y., Watanabe, M., Konno, Y., Yoneda, J., Egawa, K., Ito, T., Nakatsuka, Y., Suzuki, K., Fujii, T., and Nagao, J., 2015, Chemical and crystallographic characterizations of natural gas hydrates recovered from a production test site in the eastern Nankai Trough: Marine and Petroleum Geology, v. 66, p. 396-403, <https://doi.org/10.1016/j.marpetgeo.2015.02.019>.

- Kramer, K., and Shedd, W., 2017, A 1.4-Billion-Pixel Map of the Gulf of Mexico Seafloor: Eos, <https://doi.org/10.1029/2017EO073557>.
- Kvenvolden, K. A., 2012, Methane hydrates and global climate: Global Biogeochemical Cycles, v. 2, no. 3, p. 221-229, <https://doi.org/10.1029/GB002i003p00221>.
- Lorenson, T. D., and Collett, T. S., 2018, National Gas Hydrate Program Expedition 01 offshore India; gas hydrate systems as revealed by hydrocarbon gas geochemistry: Marine and Petroleum Geology, v. 92, p. 477-492, <https://doi.org/10.1016/j.marpetgeo.2017.11.011>.
- Malinverno, A., and Goldberg, D. S., 2015, Testing short-range migration of microbial methane as a hydrate formation mechanism: Results from Andaman Sea and Kumano Basin drill sites and global implications: Earth and Planetary Science Letters, v. 422, p. 105-114, <https://doi.org/10.1016/j.epsl.2015.04.019>.
- McConnell, D., and Zhang, Z., 2005, Using acoustic inversion to image buried gas hydrate distribution: Fire in the Ice, v. 5, no. 4, p. 3-5, https://netl.doe.gov/sites/default/files/publication/HMNewsFall05_HighRez.pdf.
- McConnell, D. R., and Kendall, B. A., 2002, Images of the Base of Gas Hydrate Stability, Northwest Walker Ridge, Gulf of Mexico, Offshore Technology Conference: Houston, Texas, <https://doi.org/10.4043/14103-ms>.
- Meazell, K., Flemings, P. B., Santra, M., and Johnson, J. E., 2020, Sedimentology and stratigraphy of a deep-water gas hydrate reservoir in the northern Gulf of Mexico: AAPG Bulletin, v. 104, no. 9, p. 1945-1969, <https://doi.org/10.1306/05212019027>.
- Mienert, J., Vanneste, M., Bünz, S., Andreassen, K., Haflidason, H., and Sejrup, H. P., 2005, Ocean warming and gas hydrate stability on the mid-Norwegian margin at the Storegga Slide: Marine and Petroleum Geology, v. 22, no. 1-2, p. 233-244, <https://doi.org/10.1016/j.marpetgeo.2004.10.018>.
- Milkov, A. V., 2004, Global estimates of hydrate-bound gas in marine sediments: how much is really out there?: Earth-Science Reviews, v. 66, no. 3-4, p. 183-197, <https://doi.org/10.1016/j.earscirev.2003.11.002>.
- Moridis, G., Kowalsky, M. B., and Pruess, K., 2012, TOUGH+HYDRATE v1.2 User's Manual: A Code for the Simulation of System Behavior in Hydrate-Bearing Geologic Media, Lawrence Berkeley National Laboratory, <https://escholarship.org/uc/item/3mk82656>.
- Ogg, J. G., Ogg, G. M., and Gradstein, F. M., 2016, A Concise Geologic Time Scale, Elsevier, 240 p, <https://doi.org/10.1016/C2009-0-64442-1>.
- Peketi, A., Joshi, R. K., Patil, D., Rao, P., and Dayal, A., 2012, Tracing the Paleo sulfate-methane transition zones and H₂S seepage events in marine sediments: An application of C-S-Mo systematics: Geochemistry, Geophysics, Geosystems, v. 13, <https://doi.org/10.1029/2012GC004288>.
- Pohlman, J. W., Kaneko, M., Heuer, V. B., Coffin, R. B., and Whitticar, M., 2009, Methane sources and production in the northern Cascadia margin gas hydrate system: Earth and Planetary Science Letters, v. 287, no. 3-4, p. 504-512, <https://doi.org/doi:10.1016/j.epsl.2009.08.037>.
- Portnov, A., Flemings, P. B., You, K., Meazell, K., Hudec, M. R., and Dunlap, D. B., 2023, Low temperature and high pressure dramatically thicken the gas hydrate stability zone in rapidly formed sedimentary basins: Marine and Petroleum Geology, v. 158, p. 106550, <https://doi.org/10.1016/j.marpetgeo.2023.106550>.
- Prather, B. E., Booth, J. R., Steffens, G. S., and Craig, P. A., 1998, Classification, lithologic calibration, and stratigraphic succession of seismic facies of intraslope basins, deep-water Gulf of Mexico: AAPG Bulletin, v. 82, no. 5, p. 701-728, <https://doi.org/10.1306/1D9BC5D9-172D-11D7-8645000102C1865D>.
- Price, A., Flemings, P., Thomas, C., Cardona, A., Murphy, Z., Garcia, A., Savage, A., Houghton, J., and Pettigrew, T., 2021, GOM2 Pressure Coring Tool with Ball Valve (PCTB Land Test III Report, https://ig.utexas.edu/wp-content/uploads/2021/07/PCTB_Land_Test_III_UT_06.17.21-shrunk.pdf.
- Reeburgh, W. S., 2007, Oceanic methane biogeochemistry: Chem. Rev., v. 107, p. 486-513, <https://doi.org/10.1021/cr050362v>.
- Ruppel, C. D., and Kessler, J. D., 2017, The interaction of climate change and methane hydrates: Reviews of Geophysics, v. 55, no. 1, p. 126-168, <https://doi.org/10.1002/2016RG000534>.
- Schuur, E. A. G., Bockheim, J., Canadell, J. G., Euskirchen, E., Field, C. B., Goryachkin, S. V., Hagemann, S., Kuhry, P., Lafleur, P. M., Lee, H., Mazhitova, G., Nelson, F. E., Rinke, A., Romanovsky, V. E., Shiklomanov, N., Tarnocai, C., Venevsky, S., Vogel, J. G., and Zimov, S. A., 2008, Vulnerability of Permafrost Carbon to Climate Change: Implications for the Global Carbon Cycle: BioScience, v. 58, no. 8, p. 701-714, <https://doi.org/10.1641/b580807>.
- Shedd, W., Frye, M., Godfriaux, P., Dufrene, R., McConnell, D., Boswell, R., Collett, T., Mrozewski, S., Guerin, G., Cook, A., Shelander, D., and Dai, J., 2010, Gulf of Mexico Gas Hydrates Joint Industry Project Leg II: Results from the Walker Ridge 313 Site, Offshore Technology Conference, <https://doi.org/10.4043/20806-MS>.

- Shedd, W., Boswell, R., Frye, M., Godfriaux, P., and Kramer, K., 2012, Occurrence and nature of “bottom simulating reflectors” in the northern Gulf of Mexico: *Marine and Petroleum Geology*, v. 34, no. 1, p. 31-40, <https://doi.org/10.1016/j.marpetgeo.2011.08.005>.
- Shepard, F. P., 1954, Nomenclature based on sand-silt-clay ratios: *Journal of Sedimentary Petrology*, v. Vol. 24, p. 151-158, <https://doi.org/10.1306/D4269774-2B26-11D7-8648000102C1865D>.
- Sloan, E. D., and Koh, C. A., 2007, *Clathrate Hydrates of Natural Gases*, Boca Raton, FL, CRC Press, <https://doi.org/10.1201/9781420008494>.
- Suits, N. S., and Arthur, M. A., 2000, Sulfur diagenesis and partitioning in Holocene Peru shelf and upper slope sediments: *Chemical Geology*, v. 163, no. 1, p. 219-234, [https://doi.org/10.1016/S0009-2541\(99\)00114-X](https://doi.org/10.1016/S0009-2541(99)00114-X).
- Tsuji, Y., Ishida, H., Nakamizu, M., Matsumoto, R., and Shimizu, S., 2004, Overview of the MITI Nankai Trough Wells: A Milestone in the Evaluation of Methane Hydrate Resources, v. 54, no. 1, p. 3-10, <https://doi.org/10.1111/j.1751-3928.2004.tb00182.x>.
- Varona, G. M., Flemings, P. B., and Portnov, A., 2023, Hydrate-bearing sands record the transition from ponded deposition to bypass in the deep-water Gulf of Mexico.: *Marine and Petroleum Geology*, v. 151, no. JMPG_106172, <https://doi.org/10.1016/j.marpetgeo.2023.106172>.
- Waterman, A. S., Weber, R. D., Lu, Y., Smith, V. E., George, R. A., Reilly, T. M., Roederer, R. V., Edmunds, J. A., Parker, B. W., Myers, N. R., and Avery, A. J., 2017, *Biostratigraphic Chart - Gulf Basin, USA, Quaternary and Neogene: Paleo-Data, Inc.*, <https://www.paleodata.com/chart/>.
- Wei, L., Malinverno, A., Colwell, F., and Goldberg, D. S., 2024, Reactive transport modeling of organic carbon degradation in marine methane hydrate systems: *Scientific Reports*, v. 14, no. 1, p. 2837, <https://doi.org/10.1038/s41598-024-52957-w>.
- Wen, B., Aydin, A., and Duzgoren-Aydin, N. S., 2002, A comparative study of particle size analyses by sieve-hydrometer and laser diffraction methods: *Geotechnical Testing Journal*, v. 25, no. 4, <https://doi.org/10.1520/GTJ11289J>.
- Yamamoto, K., 2015, Overview and introduction: Pressure core-sampling and analyses in the 2012–2013 MH21 offshore test of gas production from methane hydrates in the eastern Nankai Trough: *Marine and Petroleum Geology*, v. 66, p. 296-309, <https://doi.org/10.1016/j.marpetgeo.2015.02.024>.
- Yin, Z., and Linga, P., 2019, Methane hydrates: A future clean energy resource: *Chinese Journal of Chemical Engineering*, <https://doi.org/10.1016/j.cjche.2019.01.005>.
- Yoneda, J., Jin, Y., Muraoka, M., Oshima, M., Suzuki, K., Walker, M., Otsuki, S., Kumagai, K., Collett, T. S., Boswell, R., and Okinaka, N., 2021, Multiple physical properties of gas hydrate-bearing sediments recovered from Alaska North Slope 2018 Hydrate-01 Stratigraphic Test Well: *Marine and Petroleum Geology*, v. 123, p. 104748, <https://doi.org/10.1016/j.marpetgeo.2020.104748>.
- You, K., Flemings, P. B., Malinverno, A., Collett, T. S., and Darnell, K., 2019, Mechanisms of Methane Hydrate Formation in Geological Systems: *Reviews of Geophysics*, v. 57, no. 4, p. 1146-1196, <https://doi.org/10.1029/2018rg000638>.
- Zhang, K., Moridis, G., and Pruess, K., 2011, TOUGH+CO₂: A multiphase fluid-flow simulator for CO₂ geologic sequestration in saline aquifers: *Computers & Geosciences*, v. 37, no. 6, p. 714-723, <https://doi.org/10.1016/j.cageo.2010.09.011>.
- Zheng, J., Chong, Z. R., Qureshi, M. F., and Linga, P., 2020, Carbon Dioxide Sequestration via Gas Hydrates: A Potential Pathway toward Decarbonization: *Energy & Fuels*, v. 34, no. 9, p. 10529-10546, <https://doi.org/10.1021/acs.energyfuels.0c02309>.